

DISS. ETH NO. 26918

**STRUCTURE-PROPERTY RELATIONSHIP OF
NANOCELLULOSE FIBRILS AND THEIR
SELF-ASSEMBLED MATERIALS**

A thesis submitted to attain the degree of
DOCTOR OF SCIENCES of ETH ZURICH
(Dr. sc. ETH Zurich)

presented by

Mario Christian Arcari

MSc ETH Food Science, ETH Zurich

born on 05.05.1990

citizen of Zurich, Switzerland

accepted on the recommendation of
Prof. Raffaele Mezzenga (examiner)
Dr. Gustav Nyström (co-examiner)
Prof. Christoph Weder (co-examiner)

2020

ACKNOWLEDGEMENTS

I thank Raffaele for giving me the opportunity to do the PhD in the Food and Soft Materials group that I was finally part of for more than six years.

I thank Gustav, who invited me to tackle this SNF project together. I am grateful for his support and help during all this time, also after he left the FSM group.

I thank my coworkers and the members of the FSM group for the nice time we spent together, within but also outside the lab. A special thanks to my office mates Kathleen and Leonie, to Mattia and Yiping who were always open for discussion, to Horst, Massimo, Paride and Michael for all the breaks with the nice coffee from our own machine.

I am very thankful to the students I could work together on their thesis: Elena, Roberto and Lukas, who always challenged me with their questions and ideas.

I am grateful to my friends who stand at my side no matter what happens.

Finally, I thank my family for their patience, for listening and their encouragement in all situations of life.

SUMMARY

Sustainable and environmentally friendly materials gain increasing attention in time of climate change. A promising alternative to traditional petrol-based materials is cellulose, one of the most abundant biopolymers obtained from trees, plants, algae and bacteria. The processing and refinement for improved and new materials using nanocellulose particles is the major focus in cellulose research.

In this thesis, the extraction, production and characterization of cellulose nanofibrils (CNFs) from two different softwood pulps by TEMPO-mediated oxidation is described. Using CNFs as building-blocks, we further studied the structure-property relationship of self-assembled materials such as hydro- and aerogels as well as the mechanism of CNF adsorption at the air-water interface.

Chapter 1 introduces to the current research in the field, describing the mechanisms of nanocellulose extraction and thereof formed structures and materials. This chapter highlights the most important accomplishments and challenges in nanocellulose research, providing the motivation for this thesis.

Chapter 2 presents a systematic alteration of process parameters to produce CNFs from bleached and unbleached softwood pulp by TEMPO-mediated oxidation. Atomic force microscopy (AFM) combined with statistical image analysis provided insights into the nanostructures of individualized CNFs and allowed for a comparison between samples produced with different production parameters. We confirmed and quantified the shortening of fragments due to both increasing mechanical treatment (sonication in our study) and higher surface charge density of the CNFs. Having collected data over a set of differently charged CNFs and various sonication times allowed us to predict the exact impact of the production parameters. Further, we observed morphological differences between samples from bleached and unbleached pulps. We were able to determine the twisting periodicity of the CNFs from the different pulp samples and found a decrease in periodicity with increasing charge density by analyzing high-resolution AFM height images. These findings can help adapting desired nanostructural properties of CNFs to specific applications.

Chapter 3 describes the analysis of the bulk behavior of the previously characterized CNFs. Trying to upscale the production, we found that additionally to the beforehand studied parameters (sonication and charge density) the concentration of the pulp during the mechanical treatment played an important role. Thereby, we realized that the mechanical disintegration by sonication to individualize CNFs was limited by the dynamic overlap concentration C^{**} of

CNFs, which was proportional to the inverse aspect ratio of the fibrils. Rheological analysis revealed that the dynamic overlap concentration also depicts well the transition from viscous to elastic behavior of CNF dispersions. Further, we utilized the rheological analysis of hydrogels to determine the mesh size experimentally, resulting in a value of 81 nm for 0.06 wt% hydrogels and found a good agreement with predictions from scaling arguments (88 nm). The production of aerogels from the hydrogels by supercritical CO₂-drying turned out to be much more complicated as they are super hydroscopic, fragile and sticking to any surface. Thus, the aerogels were very delicate to handle and prevented us from performing mechanical analysis with the available equipment. More effort to improve the applicability of the aerogels is needed and could be realized by functionalization with hydrophobic molecules.

In Chapter 4, we investigated the mechanism behind the stabilization of interfaces by cellulose. Using the CNFs with varying contour length and surface charge densities, we were able to follow their behavior at the air-water interface. In diffusion-limited experiments, CNFs adsorbed at the air-water interface within 24 h, reducing the surface tension due to the formation of highly viscoelastic interfacial layers. We found that lower surface charge densities of the CNFs accelerated the interfacial adsorption, leading to an increase in surface pressure and thus a decrease of the surface tension of around 10 mN/m. Neutron reflectivity experiments revealed a surface coverage of ~ 40% and qualitatively suggested a contact angle smaller than 90°, since CNFs remained mainly in the water phase. We concluded that the surface charges limit the interfacial adsorption and lead to lower surface coverage. Moreover, the low contact angle is most certainly the reason for the poor foaming capacity of CNFs.

Chapter 5 deals with the electrostatic complexation of CNFs and amyloid fibrils from β -lactoglobulin (BLG), oppositely charged polyelectrolytes to create hybrid materials. We studied the interaction of the two polymers at different concentrations as well as the impact of the pH. Further, we presented a proof-of-concept for a core-shell filament with a conductive gold-crystal core and an insulating CNF shell.

In short, this thesis discusses the impact of production parameters on the morphology of TEMPO-CNFs and the formation of self-assembled materials from these CNFs. Thereby, the focus lays on the influence of the properties of the individual CNF as building block to the properties of the thereof formed structures. This understanding provides the foundation for designing materials and self-assembled structures by a bottom-up approach.

ZUSAMMENFASSUNG

Nachhaltige und klimafreundliche Materialien gewinnen immer mehr an Bedeutung. Zellulose ist eines der am häufigsten vorkommenden Biopolymere, das aus Bäumen, Pflanzen, Algen und Bakterien gewonnen wird. Die Verarbeitung und Veredelung zu verbesserten und neuen Materialien zu finden, steht im Mittelpunkt der aktuellen Forschung auf diesem Gebiet.

Diese Doktorarbeit beschreibt die Herstellung und Charakterisierung von Zellulosenanofibrillen (CNFs) aus zwei verschiedenen Nadelholzzellstoffen durch TEMPO-Oxidation. Unter Verwendung der CNFs als Bausteine untersuchten wir die Struktur-Eigenschafts-Beziehung von selbst zusammengesetzten Materialien wie Hydro- und Aerogelen und den Mechanismus der Adsorption an der Luft-Wasser-Grenzfläche.

Kapitel 1 führt in die aktuelle Forschung auf diesem Gebiet ein und beschreibt die Mechanismen der Extraktion von Nanozellulose sowie die daraus gebildeten Strukturen und Materialien. Dieses Kapitel hebt die wichtigsten Errungenschaften und Herausforderungen in des Forschungsgebiet hervor und liefert die Motivation für diese Arbeit.

Im ersten Manuskript (Kapitel 2) studieren wir die systematische Änderung der Prozessparameter zur Herstellung von CNF aus gebleichtem und ungebleichtem Nadelholzzellstoff durch TEMPO-Oxidation. Rasterkraftmikroskop (AFM) in Kombination mit statistischer Bildanalyse ermöglichte Einblicke in die Nanostrukturen einzelner CNFs und einen Vergleich zwischen den Proben, die mit unterschiedlichen Produktionsparametern hergestellt wurden. Wir konnten den Effekt der Verkürzung der Fragmente sowohl durch die zunehmende mechanische Behandlung (Ultraschallbeschallung in unserer Studie) als auch durch die höhere Ladungsdichte an der Oberfläche der CNFs bestätigen und quantifizieren. Der systematisch gesammelte Datensatz ermöglichte uns eine genaue Auswertung der Auswirkungen der Produktionsparameter und lässt damit Vorhersagen machen. Darüber hinaus beobachteten wir Unterschiede zwischen Proben von gebleichtem und ungebleichtem Zellstoff, jedoch wäre eine tiefer gehende Studie erforderlich, um die genauen Ursachen für die Schwankungen zu ermitteln. Bei der Analyse der AFM-Bilder konnten wir die Periodizität des Verdrehung der CNFs aus den verschiedenen Proben bestimmen und fanden eine Abnahme der Periodizität mit zunehmender Ladungsdichte. Diese Ergebnisse helfen, gewünschte nanostrukturelle Eigenschaften der CNFs spezifisch den Anwendungen anzupassen.

Das zweite Manuskript (Kapitel 3) beschreibt die Analyse des Bulkverhaltens der zuvor

charakterisierten CNFs. Bei dem Versuch, die Produktion zu erhöhen, stellten wir fest, dass zusätzlich zu den zuvor untersuchten Parametern (Beschallung und Ladungsdichte) die Konzentration des Zellstoffs eine wichtige Rolle spielte. Dabei stellten wir fest, dass der mechanische Zerfall durch Beschallung zur Herstellung individualisierter CNFs durch die dynamische Überlappungskonzentration C^{**} der CNFs begrenzt war, die proportional zum umgekehrten Formfaktor der Fibrillen (bestimmt bei niedrigen Konzentrationen) war. Rheologische Messungen ergaben, dass die dynamische Überlappungskonzentration auch den Übergang vom viskosen zum elastischen Verhalten von konzentrierten CNF-Dispersionen gut abbildet. Zusätzlich konnten wir die rheologische Analyse von Hydrogelen nutzen, um die Maschenweite experimentell auf 81 nm für Gelen von 0,06 Gew.-% zu bestimmen und fanden eine gute Übereinstimmung mit Vorhersagen aus Skalierungsargumenten (88 nm). Die Bildung von Aerogelen aus den Hydrogelen durch überkritische CO_2 -Trocknung erwies sich als wesentlich komplizierter als ursprünglich angenommen. Die getrockneten CNFs waren enorm hygroskopisch, und die Luftfeuchtigkeit bei normalen Raumbedingungen war hoch genug, um die Aerogele innerhalb weniger Tage schrumpfen zu lassen. Aufgrund ihrer Zerbrechlichkeit und Klebrigkeit an Oberflächen waren die superleichten Aerogelen sehr empfindlich in der Handhabung. Diese ungünstigen Eigenschaften und die extrem niedrige Dichte hinderten uns daran, mit der verfügbaren Ausrüstung mechanische Analysen durchzuführen. Weitere Anstrengungen zur Verbesserung der Anwendbarkeit der Aerogelen sind erforderlich und könnten durch Funktionalisierung mit hydrophoben Molekülen realisiert werden.

Im dritten Manuskript (Kapitel 4) untersuchten wir den Mechanismus hinter der Stabilisierung von Grenzflächen durch Zellulose. Anhand der CNFs mit unterschiedlichen Konturlängen und Oberflächenladungsdichten konnten wir ihr Verhalten an der Luft-Wasser-Grenzfläche untersuchen. In diffusionsbegrenzten Experimenten adsorbierten die CNFs innerhalb von 24 h an der Luft-Wasser-Grenzfläche und reduzierten dabei die Oberflächenspannung durch die Bildung hoch viskoelastischer Grenzflächenschichten. Wir fanden heraus, dass niedrigere Oberflächenladungsdichten der CNFs die Grenzflächenadsorption beschleunigten, was zu einem Anstieg des Oberflächendrucks und damit zu einer Abnahme der Oberflächenspannung um etwa 10 mN/m führte. Neutronenreflexionsexperimente ergaben eine Oberflächenbedeckung von $\sim 40\%$ und legten qualitativ einen Kontaktwinkel kleiner als 90° nahe, da die CNFs hauptsächlich in der Wasserphase verblieben. Wir kamen zu dem Schluss, dass die Oberflächenladungen die Grenzflächenadsorption begrenzen und zu einer geringeren Oberflächenbedeckung führen,

darüber hinaus ist der niedrige Kontaktwinkel der Grund für die geringe Schaumbildungskapazität der CNFs.

Die vierte Arbeit (Kapitel 5) befasst sich mit der Komplexierung von CNFs und BLG-Fibrillen, entgegengesetzt geladener Polyelektrolyten, zur Bildung von Hybridmaterialien. Wir untersuchten die Wechselwirkung der Polymere bei verschiedenen Konzentrationen sowie den Einfluss des pH-Wertes. Ferner präsentierten wir einen Proof-of-Concept für einen druckbaren Koaxialdraht mit einem leitfähigen Gold-Nanokristallkern und einer isolierenden CNF-Hülle.

CONTENTS

Chapter 1: Introduction	9
1.1 Motivation	9
1.2 Cellulose materials	10
1.3 Electrostatic complexation for hybrid materials.....	17
1.4 Methodologies of characterization	19
1.5 Scope	20
Chapter 2: Nanostructural properties and twist periodicity of cellulose nanofibrils with variable charge density.....	21
Chapter 3: Structure property relationships of cellulose nanofibril hydro- and aerogels and their building blocks.....	43
Chapter 4: Designing cellulose nanofibrils for stabilization of fluid interfaces	63
Chapter 5: Conductive and insulated gold hybrid core-shell structures.....	77
Chapter 6: Conclusion of the thesis.....	91
Chapter 7: Outlook	93
Chapter 8: Confinement-induced ordering and self-folding of cellulose nanofibrils	95
Chapter 9: References	111

Introduction

1.1 Motivation

Climate change and resource management are some of the most challenging problems we are facing in the 21st century. Humanity is using more resources than can possibly be produced in a sustainable way, risking destruction of planet earth as a habitat for successor generations. These problems lead to the need of rethinking social and environmental behavior of our society, causing an increasing demand of sustainable and environmentally compatible solutions.

Coal and petrol-based fuel were the foundation of the industrial revolution in the 18th century. However nowadays, the dislocation of tremendous amounts of CO₂ into the biosphere leads to serious consequences to our environment.

There is an emerging request for green solutions to replace petrol-based resources. Not only fuel for transportation, but also materials for packaging and commodity should be substituted in a sustainable way. The need for providing attractive alternatives from petrol-based materials challenges academic as well as industrial researchers. Thereby, the properties of the well-established materials need to be maintained or even improved, so that industry benefits from the adaptation to green and sustainable alternatives. Furthermore, for a broad acceptance of the sustainable innovations, the safety of these materials needs to be guaranteed.

Due to the abundancy, renewability and excellent mechanical properties, cellulose is one of the biopolymers with the highest potential to fulfill these challenges. In recent years, a broad variety of new applications and innovations using cellulose emerged, where self-assembled materials and nanomaterials produced from cellulose arose as a peculiar field with great prospects.

In this doctoral thesis, I used cellulose nanoparticles to study the structure-property relationship of self-assembled nanocellulose materials. The following introduction provides an overview of the production of cellulose nanoparticles as well as the formation of self-assembled structures.

1.2 Cellulose materials

Cellulose is the structure providing compound in the cell walls of trees, plants, bacteria and algae. Due to its flexibility, low weight and high mechanical strength, human society has exploited cellulose as an engineering material for thousands of years and the technological applications have improved throughout the evolution of humanity. Starting as a construction material, over time, the usage has evolved for even more complex applications such as textiles, paper production and recently in the form of delignified wood as novel high-end construction material.^[1-3]

The favorable mechanical properties of wood- and cellulose-based materials are centered on the hierarchical structure within the cell wall as schematically shown in Figure 1A. Repeated units of glucose molecules are covalently bound (β 1-4 glucosidic bond) to form a linear chain of several thousands of molecules. Multiple cellulose chains are connected parallelly via hydrogen bonds to form cellulose fibrils. The intra- and inter-chain hydrogen bonds are responsible for the high axial stiffness. These features are utilized by organisms such as trees and plants to form extremely robust cell wall matrices. Thereby, cellulose fibrils are aligned and interconnected via hemicellulose and lignin to form microfibrils (Figure 1b).^[2]

Depending on the source and treatment, cellulose possesses four different crystalline structures,^[4,5] whereas only cellulose I is the naturally occurring crystalline structure. Two subgroups are distinguishable with $I\alpha$ being the dominating polymorph produced by most algae and bacteria.^[6] In higher plant cell walls and tunica, the $I\beta$ polymorph is the most abundant structure.^[7]

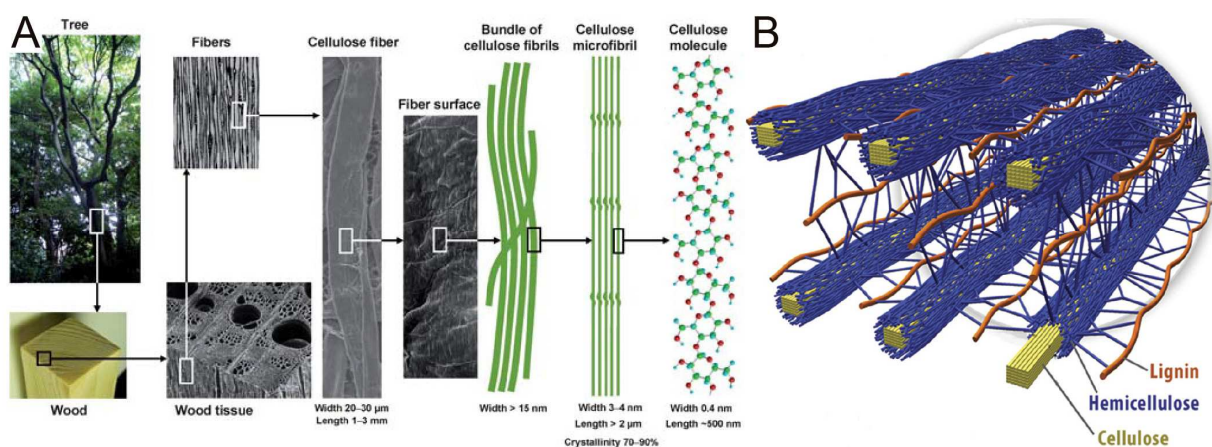


Figure 1: A) Schematic illustration of hierarchical structure of cellulose from wood biomass. Reproduced from ref. ^[8] with permission of The Royal Society of Chemistry. B) Illustration of cellulose nanofibrils surrounded and interconnected by hemicellulose and lignin. Reproduced from ref. ^[9] with permission of The Royal Society of Chemistry Materials.

For its beneficial properties, nanocellulose gained enormous attention in nanotechnological applications.^[10–13] The hierarchical organization of cellulose, hemicellulose and lignin in the plant matrix can be broken down to its individual compounds. This is done in the pulping process, where the cellulose containing plant material is dispersed in aqueous slurries. There are different processes to purify the cellulose and increase its dispersibility in water since native cellulose is hydrophobic. Additionally, steric or electrostatic repulsion of the cellulose particles can improve the stability of thereof formed colloidal dispersions. By controlling the self-assembly of the colloids, a vast variety of materials can be achieved. There are thin films with optical properties such as color adaptation due to humidity,^[14,15] UV reflecting behavior,^[16] or gas-barriers for food storage.^[17] Flame-resistant cellulose materials can be achieved by phosphorylation of foam-like materials.^[18] Generally, cellulose is well suited to produce self-supporting and highly porous materials for a lot of different applications such as wastewater treatment,^[19] oil adsorption,^[20] flow-through catalysis,^[21] thermal insulation,^[22] inks for 3D-printing,^[23–25] or templates for cell growth in biomedical applications.^[26,27]

1.2.1 Extraction methods for cellulose nanoparticles

Nanocellulose may serve as a building block to design functional materials by a bottom up approach. There are different approaches for extracting cellulose nanoparticles yielding in different properties and morphologies. The most common used methods are sulfuric acid degradation^[28] and TEMPO-mediated oxidation^[29] in combination with a mechanical disintegration step (*e.g.* sonication or homogenization) to produce cellulose nanoparticles with a high aspect ratio and distinguished surface modifications. These surface modifications introduce ionic groups that electrostatically stabilize the resulting colloids in aqueous dispersions. Unmodified, the functionality of these side groups are rather limited, however, they can be functionalized to acquire desired properties such as hydrophobicity.^[11,30]

In the process of nanocellulose production, two major groups of resulting particles are distinguishable. Typically, sulfuric acid degradation yields in short and rod-like particles, so called cellulose nanocrystals (CNCs) with dimensions of 100-200 nm length and 5-20 nm diameter,^[31] whereas the TEMPO-mediated oxidation process leads to more fiber-like particles, the cellulose nanofibrils (CNFs). CNFs are generally thinner, 2-5 nm in diameter, and can show lengths of more than 1 μm . Depending on the source and method of isolation, the dimensions can vary.^[31] Representative particles of each group are shown in the AFM height images in Figure 2.

CNCs are known for their ability to form liquid crystallin phases,^[32–35] reinforcing fillers for

composites^[36–38] and their ability to stabilize fluid interfaces to produce emulsions.^[39,40] CNFs are generally longer and thinner particles, resulting in a higher aspect ratio than CNCs, and show kinks along their contour.

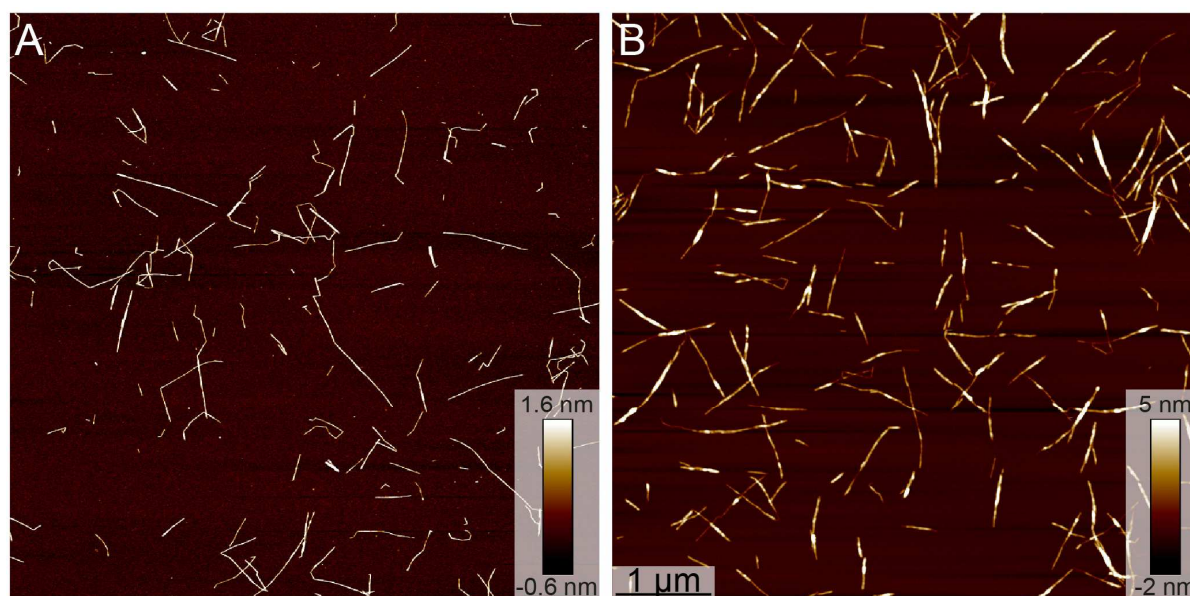


Figure 2. A) CNFs from TEMPO-mediated oxidation with high aspect ratio and kinks. B) CNC from sulfuric acid hydrolysis without kinks and rod-like shape. The scale bar is for both images.

1.2.2 Extraction of cellulose nanofibrils by TEMPO-mediated oxidation

In 2007, Saito and Isogai developed a protocol to produce highly crystalline and individualized CNFs using the 2,2,6,6-tetramethylpiperidine-1-oxyl (TEMPO) radical.^[29] In this process, TEMPO highly selectively^[41] oxidizes the methylene C6 carbons on the CNF surface to a carboxylic group via an aldehyde (Figure 3). After the TEMPO-mediated oxidation of pulp, the slurry is mechanically treated. Due to the negatively charged surfaces of the fibrils, they repel each other and form transparent, stable CNF dispersions after the mechanical treatment. The mild conditions and high selectivity for the C6 carbon of the TEMPO-mediated oxidation allows the preservation of the crystalline core of the CNFs.^[42]

The major production parameters that define the characteristics of the CNFs are the time of mechanical treatment and the added amount of NaClO, thus the energy input and the primary oxidant, respectively. Increasing the amount of NaClO leads to a higher surface charge density and to shorter CNFs with a lower degree of polymerization after sonication.^[43,44] Longer sonication leads to a better disintegration of the fibril matrix to individual particles, but also results in shorter fragments due to fracturing and induction of along the fibril contour.^[45–47] However, a threshold of shortening depending on the cellulose source can be observed, preventing them from becoming completely rod-like particles without kinks and thus not allow-

ing the formation of liquid crystalline phases as observed in CNCs.^[47]

The impact of variations in process parameters has been a focus of research since the development of the protocol in 2007 with the goal to better understand the effect of TEMPO-mediated oxidation of paper pulp.^[8,48–51] This knowledge is the foundation for predictions of CNF properties,^[45,52,53] optimization^[54,55] and upscaling for efficient industrial processes.^[56,57] All studies confirm the trend of shortening due to increasing mechanical treatment and higher surface charge densities. However, a systematic comparison of the different parameters is still lacking. Such a study becomes even more important in perspective of recent findings that variations in the source materials lead to significant differences in the fibril properties of the resulting CNFs.^[58]

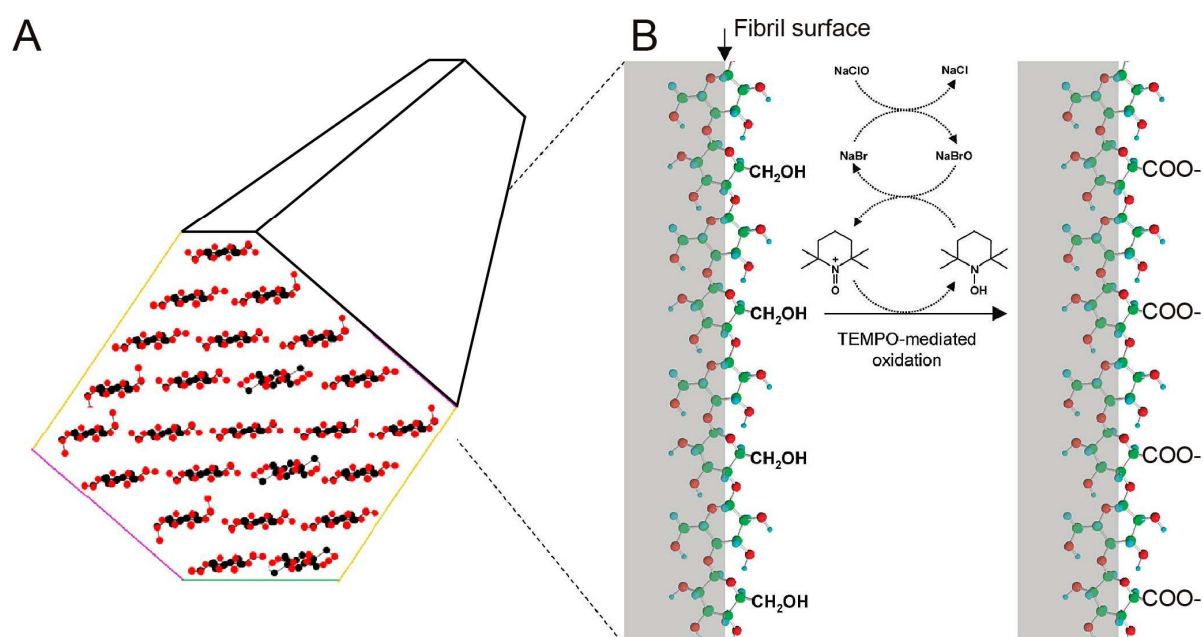


Figure 3: Schematic of a single CNF. A) Cross-section of the crystalline structure. Reproduced from ref. ^[59] by permission of PNAS. B) Surface modification due to TEMPO-mediated oxidation. Adapted with permission from ref. ^[42]. Copyright (2010) American Chemical Society.

1.2.3 Chirality of cellulose

Above a given concentration, CNCs are able to form liquid crystalline phases (Figure 4a).^[32,60] In this regime, the optical properties can be tuned by the properties of the CNC (*e.g.* aspect ratio and surface charges) determined through the isolation process, as well as the ionic strength of the dispersion.^[61–64] The individual CNC particles possess a right-handed twist and are therefore chiral particles.^[46] This chirality can lead to the formation of chiral nematic, also called cholesteric phases, where the particles are aligned parallel in a plane, however, twisted in z-direction (Figure 4b). Thereby, a transfer of chirality from the single, right-handed particles to a left-handed cholesteric phase is observed.^[46] In nature, plants and animals use this

twisted alignment to form highly robust and elastic structures for protection or intense colors (structural colors).^[65,66] Anisotropic particles like CNCs can be used to mimic structures provided by nature resulting in a vast range of applications emerging such as films with favorable tensile stress or changing colors due to humidity.^[15,67,68] The right-handedness of CNFs has only been proven recently, however, the impact of material properties such as surface charge density, fibril diameter and composition of the crystalline core on the quantitative amount of fibril twisting has still to be revealed.

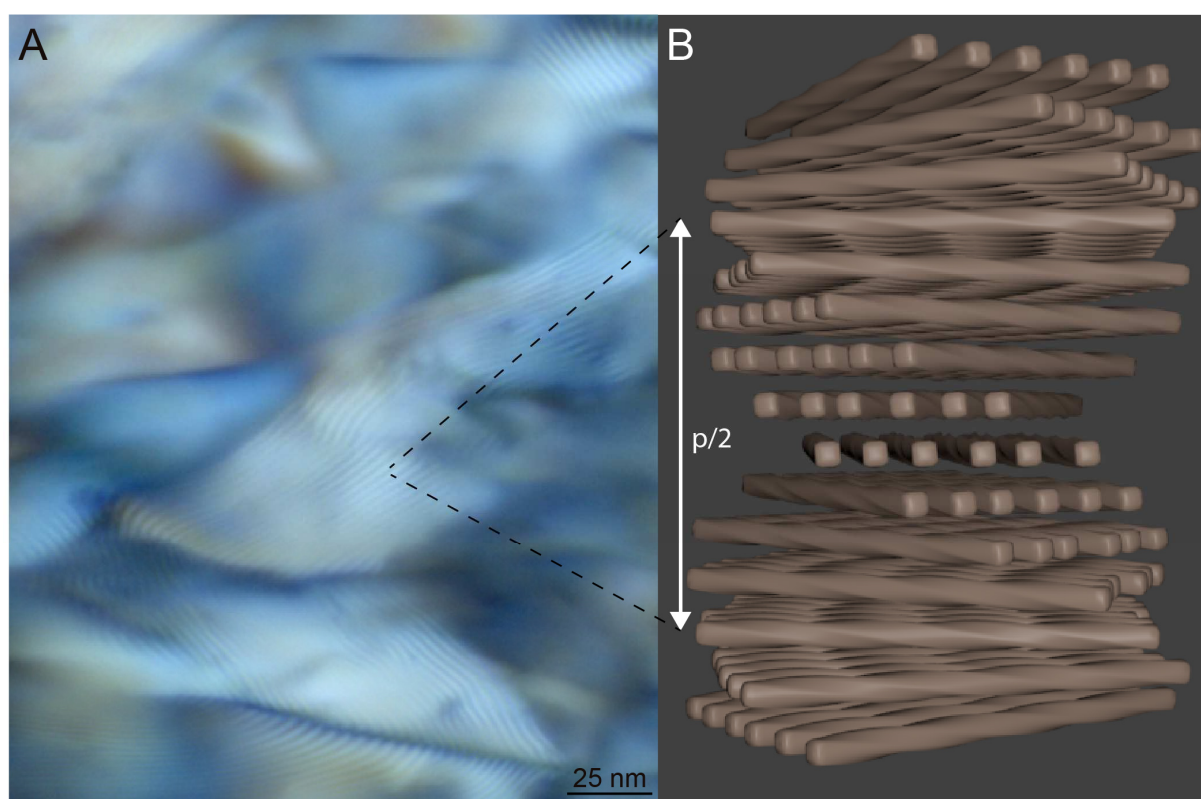


Figure 4: A) Cholesteric liquid crystalline phase from sulphated CNCs. B) Schematic of helical twist of CNCs that lead to the cholesteric phase. The arrow indicates half the pitch (180° rotation of the fibrils) what is the distance between two lines in panel A.

1.2.4 Formation of cellulose materials, structures and their characterization

Hydrogels

Hydrogels are systems where a network formed by colloidal particles or polymers enclosed by a continuous phase of water. For the colloidal network to be formed, certain conditions must be fulfilled to allow the particles to interact. Basically, the concentration of the colloids needs to be above a certain threshold, bringing the particles close enough to each other for them to interact. There are several ways to produce hydrogels, relevant for cellulose are salt and pro-

ton induced gelation or increasing the colloid concentration to cause jamming of the dispersion. To achieve stable gels, the particles have to be crosslinked. Crosslinking can be achieved by covalent bonds using reactive molecules (chemical crosslinking).

A second possibility for a stabilized network is physical crosslinking, where several alternatives are possible. As noted earlier, CNF form stable dispersions due to the negative charges on the fibril surface of the carboxylic groups. The addition of cations (*e.g.* Na⁺ or Ca²⁺) leads to screening of the surface charges and decreases the repulsion between the individual fibrils, allowing them to come closer and form hydrogen bond that further stabilizes the interaction. The same effect can be achieved by lowering the pH since protonation reduces the amount of negative charges. Additionally, it promotes the formation of hydrogen bonds between different fibrils, resulting in even stronger hydrogels than charge screening.^[69] A third way producing physical hydrogel is by concentrating a CNF dispersion, thus decreasing the excluded volume of the fibrils, forcing them to come closer than they would at ideal conditions, a jammed system is formed.

Due to the anisotropic morphology and the simplicity of controlling the gelation, CNFs are a widespread model system for rheological studies. However, the lack of comparability between the CNFs used in different studies makes the understanding of structure-property relationships between the building blocks and the thereof resulting materials nearly impossible.

Aerogels

An aerogel is a super light material, where a porosity of more than 99% and surface areas of 500-600 m²g⁻¹ for CNF aerogels can be achieved.^[70] They are generally produced from hydrogels, where the water phase is replaced with air. However, the replacement of the water proves to be challenging as due to the extremely high capillary forces of water, drying of hydrogels at room conditions leads to a collapse of the network structure, resulting in xerogels with a significant lower porosity (Figure 5a). The impact of water's high capillary force can be avoided by exchanging the water with solvent featuring a lower capillary force.

Freeze drying is another option to create highly porous structures, so called cryogels.^[71-77] In contrast to the supercritical CO₂-drying, where the pore size is determined by the CNF properties, the pores of cryogels are defined by the freezing process. As shown in Figure 5d, cryogels prevail pore walls and appear honey-comb-like.

The capillary forces can be reduced to a minimum by using supercritical CO₂-drying. Since water and liquid CO₂ are immiscible, the water needs to be replaced by a solvent miscible with liquid CO₂, often ethanol or methanol. The exchange of the organic solvent with CO₂ takes place under pressure (~ 5 MPa). As soon as the organic solvent is completely ex-

changed, the pressure is increased, bringing the CO₂ to the supercritical state. This allows the transition from the liquid to the gaseous phase without phase transition and thus avoiding the impact of capillary forces (Figure 5b).^[70,78–80]

Assuming a minimal impact on the network structure due to supercritical CO₂-drying and that the network properties are mainly given by the characteristics of the particles, variations in aerogels from different CNFs should be observable, allowing the analysis of a structure-property relationship.

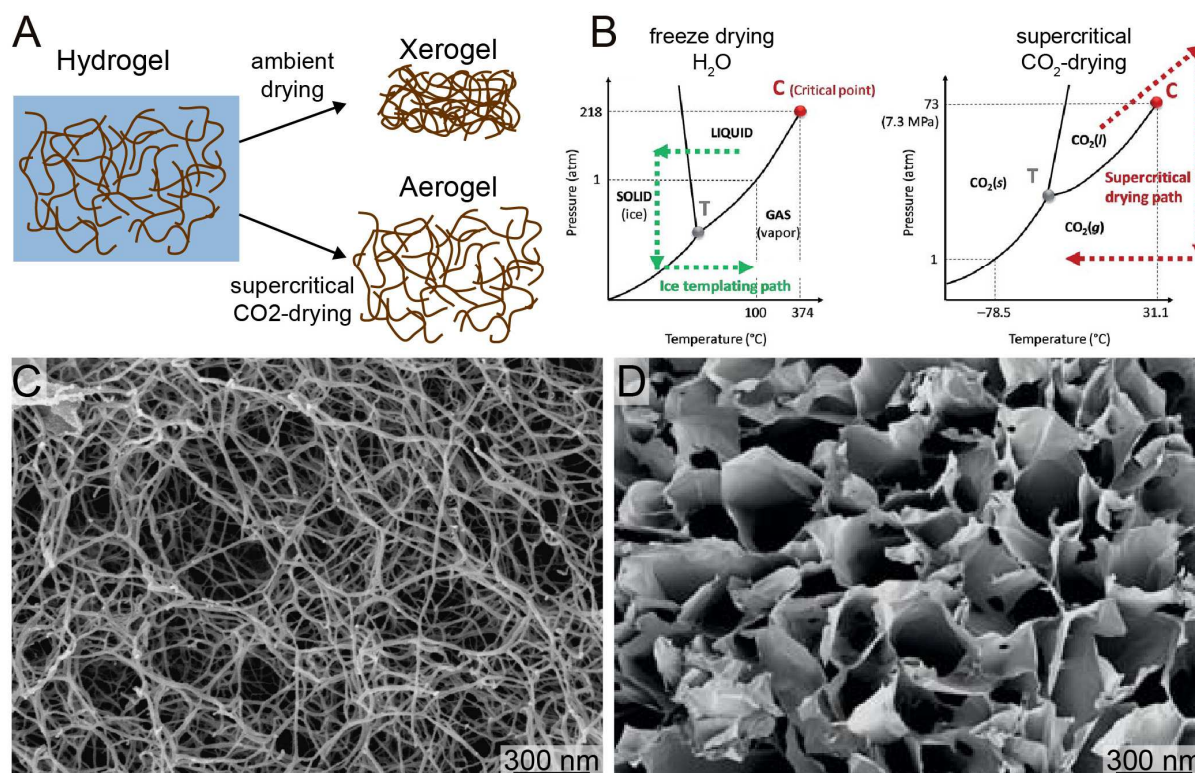


Figure 5: A) Schematic illustration of drying methods and the impact of to the network structure due to drying at ambient conditions and supercritical CO₂-drying to form xerogels and aerogels, respectively. B) Phase diagram of freeze drying and supercritical CO₂-drying. Reproduced from ref. ^[78] by permission of The Royal Society of Chemistry. C) SEM of CNF network structure due to supercritical CO₂-drying and D) due to freeze drying, respectively. Reproduced from ref. ^[77] by permission of The Royal Society of Chemistry.

Interface

The topography of cellulose nanoparticles allows wetting by both, hydrophilic and hydrophobic, phases and thus the particles are favored at the interface, where they lower the interfacial tension resulting in an increase of the total interface area. Therefore, cellulose nanoparticles are well known to form stable oil-water and water-oil emulsions.^[81–84] These particle-stabilized emulsions are called Pickering emulsions. In contrast to the formation of stable wa-

ter-oil interfaces, nanocellulose has very poor capacities to stabilize foams, so that additional surfactants are needed.^[85]

It was thought that cellulose does not adsorb to the air-water interface without further hydrophilization. Only recently, it was shown that CNCs are able to adsorb at the interface, however in much longer timescales than for surfactants.^[40,86] A complete adsorption in diffusion-limited experiments lasted several hours and decreased the interfacial tension similarly to surfactants. Comparable studies of the adsorption behavior of CNFs at the air-water interface and interfacial stabilization are still missing.

1.3 Electrostatic complexation for hybrid materials

Cellulose has outstanding physical properties, although it lacks functionalities without further modifications. The formation of hybrid materials allows the combination of CNFs' favorable properties with functional molecules to create new materials with desired properties.

Beside nanocellulose, many other bio-colloids are stabilized by surface charges. Electrostatic complexation combines oppositely charged particles to produce functional materials without the addition of crosslinkers, salt or protonation. The properties of the formed complexes can be controlled by the conditions related to ionic strength, pH and hydration during the process.^[87] In contrast to hydrophobic and chemical interactions, electrostatic interactions are reversible, making it interesting for self-healing applications. Electrostatic interactions can furthermore take place in an aqueous environment without the use of harsh chemicals. This allows for bio-compatible applications such as wound healing, where the treatment has to be performed in wet conditions.^[88] The layer-by-layer technique is another prominent representative for structures formed by electrostatic interactions.^[89]

The fundamental mechanism behind the electrostatic complexation is the thermodynamically driven interaction of cationic and anionic particles or polymers to form ionic bonds. Generally, the reaction time is extremely fast, allowing efficient processes such as the layer-by-layer technique, however, complicates a homogeneous mixing of oppositely charged polymers in bulk.

A further method to produce a material exploiting electrostatic complexation is interfacial polyelectrolyte complexation (IPC) to produce fibers or filaments.^[90,91] These filaments can be drawn from the gel-like interface that is formed between two oppositely charged polyelectrolyte solutions or dispersions. This gel formed at the interface prevents the free mixing of the solutions/dispersions. Pulling the interfacial gel upwards allows the reformation of the gel at the interface between the droplets and a thus, continuous process.^[92]

1.3.1 Amyloid fibrils from β -lactoglobulin

Amyloid fibrils are associated with neurodegenerative diseases such as Alzheimer and Parkinson. Their structure is formed by stacking of β -sheets of denatured protein fragments, leading to very stable assemblies. The synthesis of these amyloid fibrils can also be performed in vitro for studying the mechanisms and conditions of the self-assembly. The gained knowledge might be translated to the living organism, aiming to understand the fundamental processes in vivo to prevent and cure diseases.

It was recently shown that amyloids are not only associated with diseases, but they also have beneficial use. A well-known model system of amyloids is β -lactoglobulin (BLG), a globular bovine milk protein, a side stream from cheese production. Recent works showed a wide range of applications such as wastewater treatment,^[93] reduction of metal salt to nanoparticles for flow through catalysis,^[94] synthesis of gold nanoparticles,^[95,96] produced materials thereof^[97,98] and liquid crystalline phases from rigid amyloid fibril fragments.^[99,100]

1.3.2 Formation of hybrid material using CNFs and amyloid fibrils

The electrostatic interactions of CNFs and protein forming complexes and gels used in material and food sciences as well as medical applications has been investigated extensively.^[101-107] CNFs have the ability to form very stable and strong films and bulk materials but lack extended functionalities. In contrast, films produced from BLG-fibrils are brittle, however due to the different amino acids, they have a great potential for chemical functionalities as exemplified above. The probably most astonishing property of BLG-fibrils is their ability to reduce Au^+ to nanometer-thin crystals possessing a large surface area.^[95,96] The ability to form these Au-crystals is attributed to the reducing properties of BLG-fibrils and the formation of a nematic phase at high enough fibril concentrations.^[95] These Au-crystals can cover huge areas with a minimal amount of gold and the materials preserve the ability of electrical conductivity.^[96] To further explain from a geometrical perspective, high aspect ratio crystals or plates facilitates the use of less amount of gold compared with spherical nanoparticles to result the same material conductivity.

The combination of CNFs and BLG-fibrils containing Au-crystals promises a composite that preserves the beneficial properties of the two components.^[108] However, only a more fundamental understanding of the interactions can lead to controlled self-assembly pathways in order to reliably produce composite materials. Therefore, the interaction between the two polyelectrolytes should be investigated depending on the concentration and effective surface charge, adjustable by the pH.

The interaction between CNFs and monomeric BLG forming bulk materials has been reported previously.^[106,107] However, a study on the interaction of CNFs with BLG-fibrils is still missing. We have chosen the IPC technique to form composite filaments to study their interaction. Gaining this knowledge enables to fine-tune the composition of the hybrid material in perspective of specific applications.

A possible application is represented by an electrically conductive filament, combining the BLG-fibril stabilized Au-crystal dispersion with CNFs that have insulating properties. To obtain a well-defined core-shell structure, injection in a coagulation bath appears to be more promising than IPC. The technique of the injection could be improved towards coaxial extrusion, which adds the possibility of precisely printing the filament in the desired manner, thus saving resources.

1.4 Methodologies of characterization

I briefly describe the most important methods of characterization used for the presented work.

1.4.1 Atomic force microscopy

Atomic force microscopy (AFM) is a high-resolution microscopy technique for topographic imaging in the nanometer scale. A cantilever with a sharp tip scans the sample that was immobilized on mica, an atomic flat surface. The height information is determined by the deflection of the cantilever due to the topography of the sample and is amplified by a laser reflected on the cantilever, recorded by a detector.

1.4.2 Rheology

The mechanical properties of soft materials and liquids can be determined by a rheometer. Thereby, the resistance to deformation and flow behavior are measured in response of an applied force. Under oscillation, the so induced stress can be fractionized into the storage (G') and loss (G'') moduli of the material, describing the elastic and viscous behavior, respectively. Substances where G'' dominates appear liquid-like and flow. An example is a diluted polymer dispersion, where the polymers are free to move. Increasing concentration or interactions lead to an increase of storage modulus G' . The formation of a network leads to the domination of G' and thus a solid-like response of the material. The behavior of materials at the transition from the viscous to the elastic regime is used to characterize their sol-gel transition.

1.5 Scope

In recent years, there have been a lot of studies illuminating different aspects of CNFs from TEMPO-mediated oxidation. Already small variations in the procedure of the TEMPO-mediated oxidation and the starting material lead to an immense impact on the resulting CNFs. These distinctions make it extremely difficult to distinguish the impact of process parameters from different studies. A systematic study with a wide range of variations in process parameters is still missing and of exceeding importance to understand the mechanism behind the production of TEMPO-CNFs and the consequences of particle characteristics for self-assembled materials.

In the following chapters, I first present a characterization of the single particles. CNFs were produced from bleached and unbleached softwood pulp with four different charge densities for both types of pulp. The impact of the different production parameters (*i.e.* sonication time, charge density and source) on the final CNF properties (*i.e.* contour length, aspect ratio and twist) was evaluated.

In the second manuscript, we investigated the impact of variations in CNF particle properties on the behavior of aqueous dispersions and self-assembled structures such as hydrogels and aerogels.

In the third manuscript, we studied the underlying mechanism of adsorption to the air-water interface of CNFs with different charge densities. These two projects allowed understanding the structure-property relationship between the different hierarchical levels of CNFs and thereof formed materials.

The fourth project exploits the interaction of oppositely charged biopolymers (CNF and BLG-fibrils mixed with Au-crystals) for a prove-of-concept of a conductive and insulated core-shell wire.

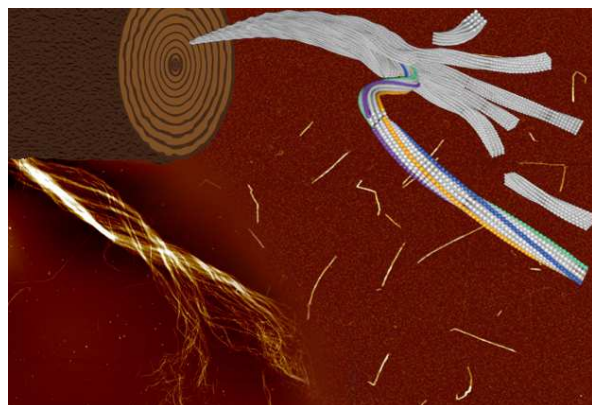
Nanostructural properties and twist periodicity of cellulose nanofibrils with variable charge density

Mario Arcari, Elena Zuccarella, Robert Axelrod, Jozef Adamcik, Antoni Sánchez-Ferrer, Raffaele Mezzenga, and Gustav Nyström

Biomacromolecules 2019, 3, 1288-1296

<https://doi.org/10.1021/acs.biomac.8b01706>

Reprinted with permission from reference ^[109]. Copyright 2019 American Chemical Society.



Nanostructural Properties and Twist Periodicity of Cellulose

Nanofibrils with Variable Charge Density

Mario Arcari¹, Elena Zuccarella¹, Robert Axelrod¹, Jozef Adamcik¹, Antoni Sanchez-Ferrer¹, Raffaele Mezzenga^{1,2} and Gustav Nyström^{1,3*}*

1. ETH Zurich Department of Health Sciences and Technology, Schmelzbergstrasse 9, LFO E23 Zurich 8092, Switzerland.
2. ETH Zurich, Department of Materials, Wolfgang-Pauli-Strasse 10, 8093 Zurich, Switzerland.
3. EMPA, Laboratory for Applied Wood Materials, Überlandstrasse 129, 8600 Dübendorf, Switzerland.

*Email: raffaele.mezzenga@hest.ethz.ch, gustav.nystroem@empa.ch

Cellulose nanofibrils (CNFs) are a renewable and facile to produce nanomaterial that recently gained a lot of attention in soft material research. The nanostructural properties of the fibrils largely determine their self-organizing functionalities, and the ability to tune CNF nanostructure through control of the processing parameters is therefore crucial for developing new applications. In this study, we systematically altered the CNF production parameters (i.e., variation in cellulose source, chemical and mechanical treatment) to observe their impact on the nanostructural properties of the resulting fibrils. Atomic force microscopy (AFM) allowed detailed topological examination of individual CNFs to elucidate fibril properties such as contour length, kink distribution and the right-handed twist periodicity of individual fibrils. Statistical analysis revealed a large dependency of the fibril properties on the cellulose source material. Our results furthermore unambiguously confirm that the linear charge density of the fibrils regulates both contour length and twist periodicity and thus has a very strong impact on the final morphology of CNFs. These results provide a route to tune the detailed nanostructure of CNFs with potential impact on the self-organization of these biological colloids and their optimal use in new nanomaterials.

INTRODUCTION

Due to its exceptional mechanical properties, nanofibrillated cellulose (NFC) is a source for a multitude of applications such as material reinforcement, hydrogels, liquid crystals and aerogels production.^[2,11] The mechanical quality of native cellulose originates from the multiple hydrogen bonds that strongly link the individual cellulose CNFs within cellulose bundles that reinforce plant cell walls. This intricate hydrogen bonded matrix, including also additional biopolymers (*i.e.*, lignin and hemicellulose), provides impressive reinforcement properties in the native state but also complicates the process to individually separate the single fibrils for new applications. One possible route to obtain NFC consists in the use of an enzymatic pre-treatment followed by mechanical homogenization or sonication.^[110–112] However, the fibrils resulting from this process are typically very polydisperse in thickness, organized in bundles of single fibrils and measuring ~5–90 nm in width.

Saito *et al.* presented an elegant way to obtain individualized CNFs from wood pulp using TEMPO-mediated oxidation conditions (T-CNF).^[29] This process allowed the production of well-defined single nanofibrils at high yields, opening up for a variety of applications to evolve, such as transparent films for food packaging with improved oxygen barriers,^[17,113] free-standing hydrogels with only 0.1 wt% cellulose mass fraction^[114] and aerogels with potential as lightweight thermal insulators.^[70] Due to their high surface area, nanocellulose aerogels can further be applied as absorbents for environmental remediation^[20] or as templates for batteries.^[115]

Worldwide, various groups work with the above-mentioned TEMPO protocol, to make different material sources accessible and compare properties of diverse NFC with T-CNF,^[31,42,44,45,50,53] where surface modifications is of special interest. Due to the mild conditions of the TEMPO-mediated oxidation process and the high selectivity to oxidize the methylene C6 carbon on the surface of the CNF, the crystalline fibril core is largely preserved.^[42] Moreover, it has been shown that increasing the charge density of CNF by increasing the amounts of hypochlorite as primary oxidant leads to shorter fibrils.^[43] Varying the exposition to sonication was also found to influence yield, diameter and degree of polymerization (DP) of CNF.^[44,53]

Usov *et al.* suggested that kinks, present along the contour of CNFs, result from the processing conditions, therefore caused by the sonication treatment, and not from alternating amorphous and crystalline domains along the nanofibril.^[45,116] The mechanism of breaking fibrils was also shown in a very recent study, where it was found that fibrils break preferably within rigid segments rather than at positions of kinks as one might assume.^[46] These results

are in agreement with Saito *et al.* who compared fibrils with various sonication times and additionally observed that the length of T-CNF converges toward a minimum of 278 ± 127 nm after more than 60 min of sonication for fibrils with a carboxylate content of 1.5 mmol per gram of oxidized wood cellulose.^[47]

Nanocellulose particles are furthermore known to twist, as experimentally observed on microfibrils^[117] and aggregated cellulose nanocrystals.^[118,119] These results from higher order nanocellulose structures were supported by observations of the twist on single CNFs,^[45] all cases revealing a right-handed twist. This right-handed twisted configuration has been confirmed by theoretical simulations as the lowest energy state for native, uncharged, crystalline CNFs.^[120,121] The amount of twist resulting from the simulations was independent on the length of the fibrils^[122,123] but inversely dependent on the fibril cross-section area,^[122–124] generally demonstrating a twisting of ~ 1.5 to 10 deg/nm for different fibril thicknesses.^[122,123] Even though there is a consensus about the right-handed twisted nature of CNFs, a direct experimental analysis of the twist periodicity of single CNFs is still missing. The exact mechanism behind the twisting also remains debated, specifically the role of the hydrogen bonds^[125] and the influences of crystalline distortions induced by mechanical defects in the form of kinks.^[126] Another unknown, yet highly relevant, parameter is the influence on the twist periodicity of the type and amount of charges introduced by surface modification during nanocellulose production.

Investigating the prior literature, there is a lack of a clear picture of the combined influence of mechanical (sonication) and chemical (pulp chemistry, charge density) treatments on the nanostructure and twist periodicity of T-CNF. Systematically altering production parameters and mapping out the impact of the manufacturing process on the CNF nanostructure in a single study becomes even more important in the context of the recent published work of Schütz *et al.*, where they showed that variations in cellulose sources may lead to tremendously different properties of the resultant cellulose nanocrystals.^[58]

In this paper, we systematically studied the change in fibril properties as a result of variations in sonication time of TEMPO-mediated oxidized CNFs with different charge densities produced from industrially bleached and unbleached softwood pulp. AFM imaging provided a basis to obtain statistics of the CNF contours including information about contour length, kinks, the average segment length, height and fibril twist. Dynamic Light Scattering (DLS) and wide-angle X-ray scattering (WAXS) were used as complementary techniques to benchmark the average contour lengths and the diameter of the crystallites obtained from AFM.

We found that different charge densities (induced by varying the oxidation treatment) and

different sonication times affect the fibril length and periodicity of the twist. These results contribute to our understanding of how the processing conditions can be used to control the CNF nanostructure, thus providing a tunability that is crucial for the use of CNFs in high performance applications.

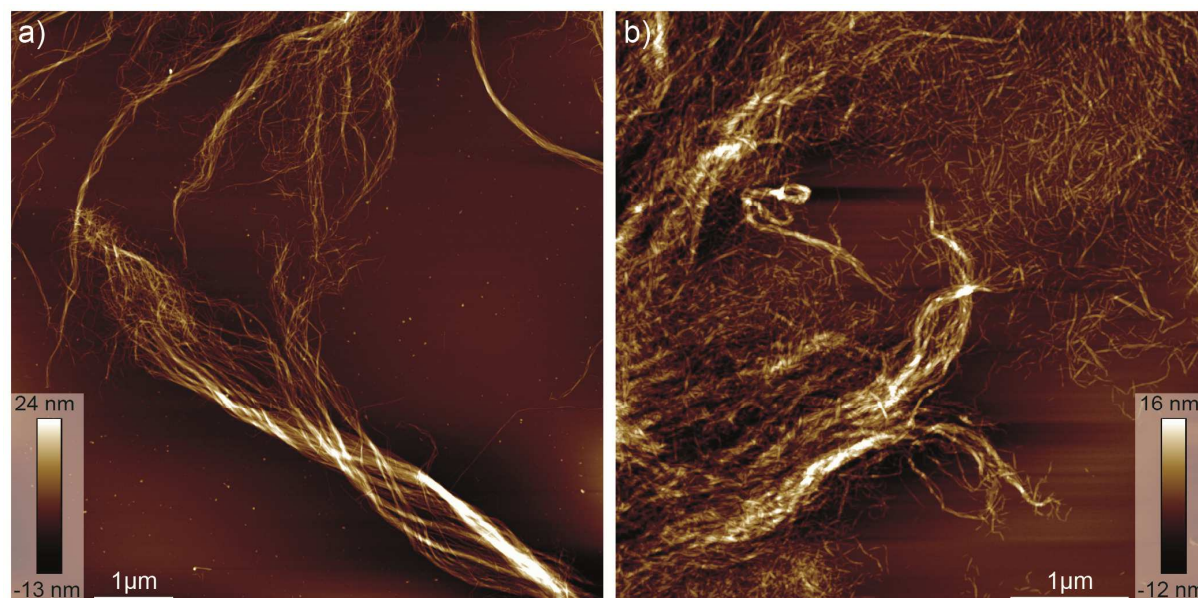


Figure 1. Unbleached and bleached softwood pulp after TEMPO-mediated oxidation. AFM images a) unbleached and b) bleached pulp after TEMPO-mediated oxidation without further treatment.

RESULTS AND DISCUSSION

Effects of varying charge density on fibrillization of TEMPO-mediated oxidized cellulose nanofibrils.

After the TEMPO-mediated oxidation under the same conditions, the industrially bleached and unbleached softwood pulp showed different morphologies. As observed in Figure 1, the unbleached pulp (a) revealed generally long fibers that unravel into fibril bundles and eventually single fibrils, whereas the bleached pulp (b) consisted of a fibril network with less pronounced hierarchical levels. The reason of the difference may be related to the composition of the pulps as discussed in the next paragraph. In both pulp samples, the smallest fibrils revealed a height of around 1.3 nm, whereas fibrils with diameters around 4 - 5 nm were the most represented population (Figure S1).

The surface charges of the T-CNF, present as carboxylic groups, was determined by conductivity titration of dispersed oxidized softwood pulp. Figure 2a indicates a difference in efficiency of the oxidation process between unbleached and beforehand industrially bleached softwood pulp as source material. The charge density of the fibrils from bleached pulp increased from 270 $\mu\text{mol/g}$ CNF (1.5 mmol NaClO) up to 1120 $\mu\text{mol/g}$ CNF (10 mmol NaClO),

whereas the unbleached pulp from 150 $\mu\text{mol/g}$ CNF (1.5 mmol NaClO) up to 940 $\mu\text{mol/g}$ CNF (10 mmol NaClO). The difference between bleached and unbleached pulp is justified by the different composition of the two genitor sources. The unbleached pulp still contains lignin and hemicellulose, which then would be removed in the following industrial bleaching process.^[127] One of the bleaching agents used in this process is NaClO that is also the primary oxidant of the TEMPO-mediated oxidation. Therefore, the presence of lignin makes NaClO less available for the TEMPO-mediated oxidation, decreasing the overall efficiency of the cellulose oxidation process for the unbleached pulp. Additionally, hemicellulose present in the unbleached pulp is also oxidized and, due to the good water dispersability of the oxidized byproduct, it is removed during the rinsing process.

The fibrillization was promoted by ultra-sonication and facilitated due to the repulsion between the single fibrils within the fibril bundles. The repulsion resulted from the negative surface charges of the fibrils at neutral pH. This mechanism can be observed on the AFM images in Figure 2c–f, where large agglomerates can be found for the lowest charge density after 7 min of sonication (c). With increasing charge density (d-f), fewer fibril agglomerates were found, translating, in turn, to an increased single fibril yield at constant sonication time. Statistical analysis of the images reveals a decrease in length-weighted average fibril length from 670 to 340 nm and 880 to 470 nm while increasing the concentration of oxidation agent from 1.5 to 10 mmol/g of cellulose for CNF from bleached and unbleached pulp, respectively (Figure 2b).

Indeed, a breakdown of fibrils into shorter objects with increasing charge density can be expected when the electrostatic energy per unit length (which favors breaking) exceeds the cohesive energy per unit length:

$$\frac{k_B T l_B (N_{charges})^2}{L} > \sigma \pi D_{equivalent} L + \Delta F \cdot L, \quad (1)$$

where k_B is the Boltzmann constant, T is the temperature, l_B is the Bjerrum length, $N_{charges}$ is the total number of charges per length L , σ is the fibril-water interfacial tension, $\pi D_{equivalent}$ is the cross-sectional perimeter of the fibril ($D_{equivalent}$ being the diameter of the cylindrical fibril with an equivalent cross-sectional perimeter) and ΔF is the total cohesive energy per length L holding the single CNF together. The critical linear charge density, at which the electrostatic breakdown is expected, can be extracted from Equation (1) using the definition $\lambda_{critic} = N_{charges}/L$, thus:

$$\lambda_{critic}^2 > \frac{\sigma\pi D_{equivalent} + \Delta F}{k_B T l_B} \quad (2)$$

Due to the high polydispersity of the fibril length and the presence of many short fragments, the difference between samples was more evident using the length weighted average fibril length. This trend is also in agreement with earlier reported data.^[43] However, a plateau in fibril length could be observed for fibrils produced from the unbleached source at charge densities between 150 and 650 $\mu\text{mol/g}$, in general agreement with equation (3) and indicating that a certain threshold of repulsion is needed for an efficient fibrillization by sonication.

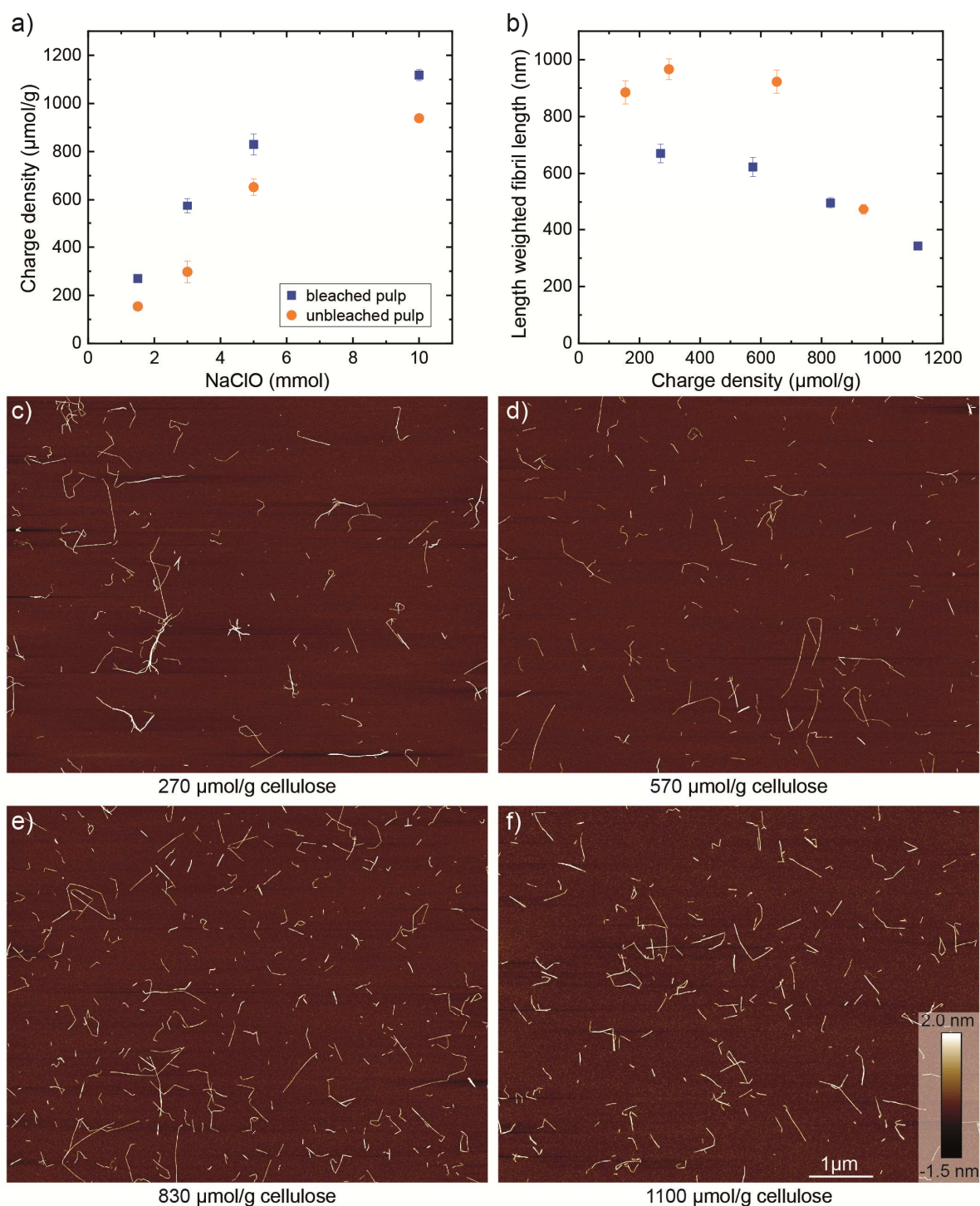


Figure 2. Influence of charge density on the fibril length. a) Charge density of carboxylic acid groups induced by varying amounts of NaClO added per gram of bleached (blue squares) and unbleached (orange circles) softwood pulp. The error bars show the standard deviation ($n = 2$). b) Plot of the length weighted averaged fibril contour length versus charge density for CNFs prepared from bleached (blue squares) and unbleached (orange circles) wood pulps (with error bars expressing the standard error of the mean, $n > 200$). c-f) AFM-images of T-CNF produced from bleached softwood pulp with varying charge density after 7 min of sonication. The scale and height bars in image f) apply to all AFM images.

Impact of sonication time on fibril length.

In agreement with earlier reports, not only the charge density but also the sonication time has a direct impact on the fibril length.^[46,47] A comparison of the ensemble average mean fibril length obtained by DLS (Figure 3a), using equation 1, with the average contour height based on fibril tracking data from AFM images showed good agreement, supporting the use of the fibril based contour tracking method. This method is hereafter used throughout the manuscript. The analysis revealed the expected shortening due to sonication. The weighted length of the longest unbleached fibrils (3 mmol unbleached) possessed the lowest charge density and decreased from 1100 nm after 5 min of sonication to 560 nm after 25 min of sonication (Figure 3b). Samples with higher charge density (e.g., 10 mmol unbleached) that had generally shorter fibril lengths after 5 min of sonication, exhibited less shortening and seemed, after 25 min, to converge to a similar length such as the 3 mmol unbleached CNFs. The fibrils from the bleached source were generally shorter than those from the unbleached. Starting at 720 nm after 5 min of sonication, their length declined to 540 nm after 25 min of sonication. Finally, the highest charged, bleached fibrils did not significantly change in length with additional sonication after the initial 5 min. A screening of sonication times shorter than 5 min revealed an inefficient fibrillization, and huge agglomerates were still observed by the AFM analysis, whereas only few single fibrils were present (Figure S2). Since the CNFs produced with 1.5 mmol NaClO per gram of cellulose have nearly the same length as those with 3 mmol NaClO per gram of cellulose, they are not shown in the plot, but the measured values are listed in Table S1. The existence of a threshold of minimal length with increasing sonication time was observed earlier^[47] and seems to be mainly dependent on the cellulose source.

Nyström *et al.* proposed a mechanism for cutting and hence shortening of fibrils, where fibrils break not only at kink position but along rigid segments too, possibly via an intermediate kink forming step.^[46] These results suggested that the kink zones are regions formed from mechanical defects, thereby being mechanically weaker than the rigid segments. Moreover, that same study showed that acid hydrolysis may be used to shorten fibrils preferentially at positions of kinks. Thus, in order to obtain fibrils with strong mechanical strength and chemical resilience for further applications, it is desirable to minimize the number of kinks, while maintaining a maximum fibril length.

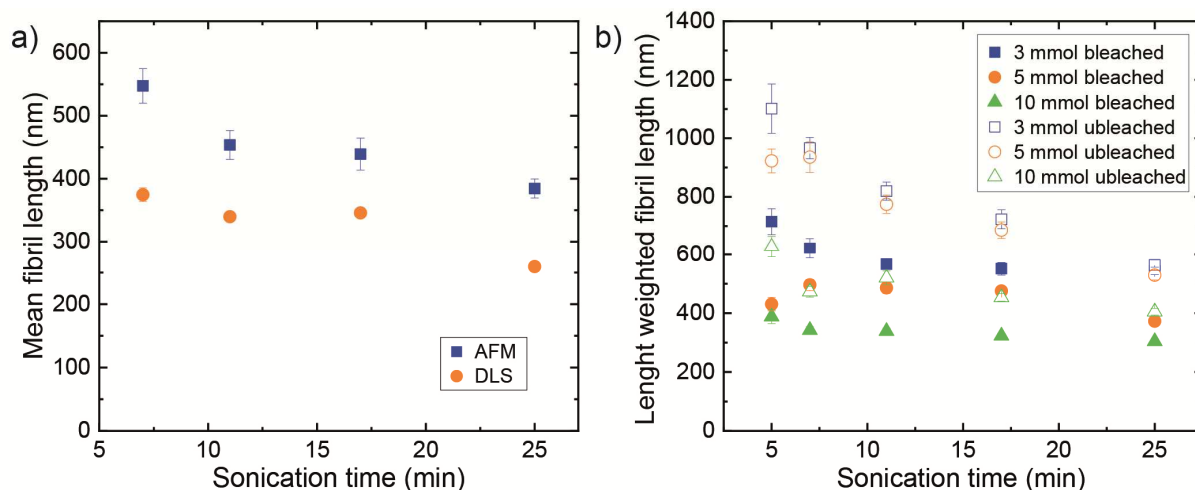


Figure 3. Influence of sonication time on fibril length. a) Comparison of mean fibril length between DLS (orange circle) and AFM (blue square) measurements of CNF dispersions prepared from unbleached wood pulp with a charge density of 300 $\mu\text{mol/g}$ CNF (standard deviation of DLS of 3 measurements and standard error of AFM $n > 200$). b) Length weighted fibril length determined by fibril tracking from AFM images (error bars express the standard error of the mean, $n > 200$) for different sonication times.

The influence of surface charge density on kink density and segment length.

So far, we can conclude that increasing charge density as well as sonication time decrease the fibril length. Do both these treatments also affect the morphology of the single fibrils in a similar way? To find out, we continued the analysis with focus on the number of kinks per fibril and the segment length of the differently charged samples. Figure 4a suggests that, with increasing charge densities, the average number of kinks per fibril is linearly decreasing from 1.9 to 0.6 and from 2.2 to 0.7 kinks per fibril for bleached and unbleached CNF, respectively. The amount of kinks per fibrils seems to be independent on the cellulose source. Therefore, the effect of increasing charge density is comparable with increasing sonication time, both leading to fewer kinks. Analyzing the average segment lengths in Figure 4b indicates an average segment length between 110 and 145 nm and 140 and 220 nm for bleached and unbleached fibrils, respectively.

Connecting the dependence of the fibril length from the charge density with the finding of the maximal segment length, we can conclude that the fibrils from the unbleached source with a charge density of 650 $\mu\text{mol/g}$ CNF result in the optimal properties of high aspect ratio and a low density of kinks.

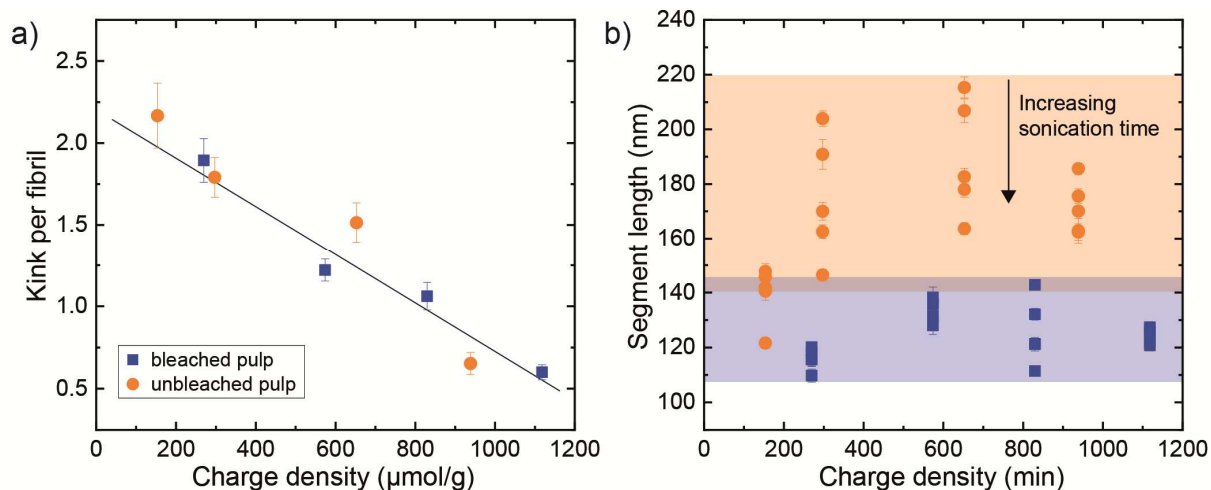


Figure 4. Influence of charge density a) on the average number of kinks per fibril after 7 min of sonication (with the black line as a linear fit) and b) the segment length at different sonication times, where the colored areas indicate the average segment length of the samples from unbleached and bleached pulps. For both graphs, the standard error is calculated based on the data of more than 200 tracked fibrils per point.

Periodicity and twist of CNFs as a function of fibril charge and thickness.

AFM imaging provides an accurate measurement in z-direction. These z-data yield precise topological information of the height variations along the fibril contour, thus allowing us to extract information on the pitch of the fibrils. Figure 5a and 5b show a representative example of a CNF scanned in orthogonal directions, where the right-handedness of the fibril is directly observable in both images. Figure 5c shows the twist periodicity, p , of the fibrils (measured as the average distance between two consecutive height maxima along the fibril contour, as depicted in Figure 5d) as a function of increasing fibril charge density. The periodicity of fibrils from bleached and unbleached sources linearly decreased from 70 to 41 nm and 55 to 40 nm, respectively, with increasing charge density. The autocorrelation function (ACF) implemented in FiberApp^[128] provides an alternative way to determine the periodicity, as shown in Figure 5e. The height profile in Figure 5d shows an average relative height difference between minima and maxima of $\sim 2^{1/2}$, suggesting a squared cross section for the right-handed fibrils as illustrated schematically in Figure 5f and in agreement with previous works^[45,126,129] but significantly different from the observations of microfibrils that have a wider (10 – 50 nm) rectangular cross-section.^[117] Based on the squared cross section and the ensued periodicity, we can assume the length of the pitch as $L = 4p$ and obtain values between 158 and 281 nm.

Turning to the fibril height, a decrease from 1.6 to 1.3 nm and 1.9 to 1.0 nm is observable for the CNF from the bleached and unbleached pulp, respectively (Figure S3 and Table S1). Height differences of less than the size of a glucose molecule (*ca.* 0.5 nm) may seem difficult

to justify but these result from averaging the heights within the sample population. WAXS experiments confirmed precisely the same trend for the bleached fibrils (Figure S3 and S4). Moreover, the chemical fibril treatment led to an increase in roughness of the mica surface, when higher charged fibril dispersions are deposited (Figure S5). The roughness might originate from an increasing amount of free cellulose polymers due to the sonication process with the corresponding peeling-off of cellulose polymer chains from the fibril surface.

It is to be expected that thinner fibrils with a smaller fibril cross-section area have a lower torsional stiffness and therefore require less energy to twist, resulting in a higher twisted configuration, as supported also by theoretical works.^[120,121] When electrostatics are taken into account, the fibril twist undergoes a more complex behavior. For amyloid fibrils, it has been shown that the periodicity is a function of the electrostatic strength and can be accurately described by a model balancing the twist elasticity of the fibril with the electrostatic repulsion from the fibril surface charges.^[130,131] Assuming a similar mechanism for the present CNFs, their twist periodicity should decrease for an increasing amount of electrostatic charge, as a result of an increased electrostatic torsional momentum, which is indeed what we observed, as shown in Figure 5c, for both the bleached and unbleached fibrils. These results confirm unambiguously that the linear charge density of the fibrils regulates contour length and twist periodicity, and thus has a very strong impact on the final morphology of CNFs.

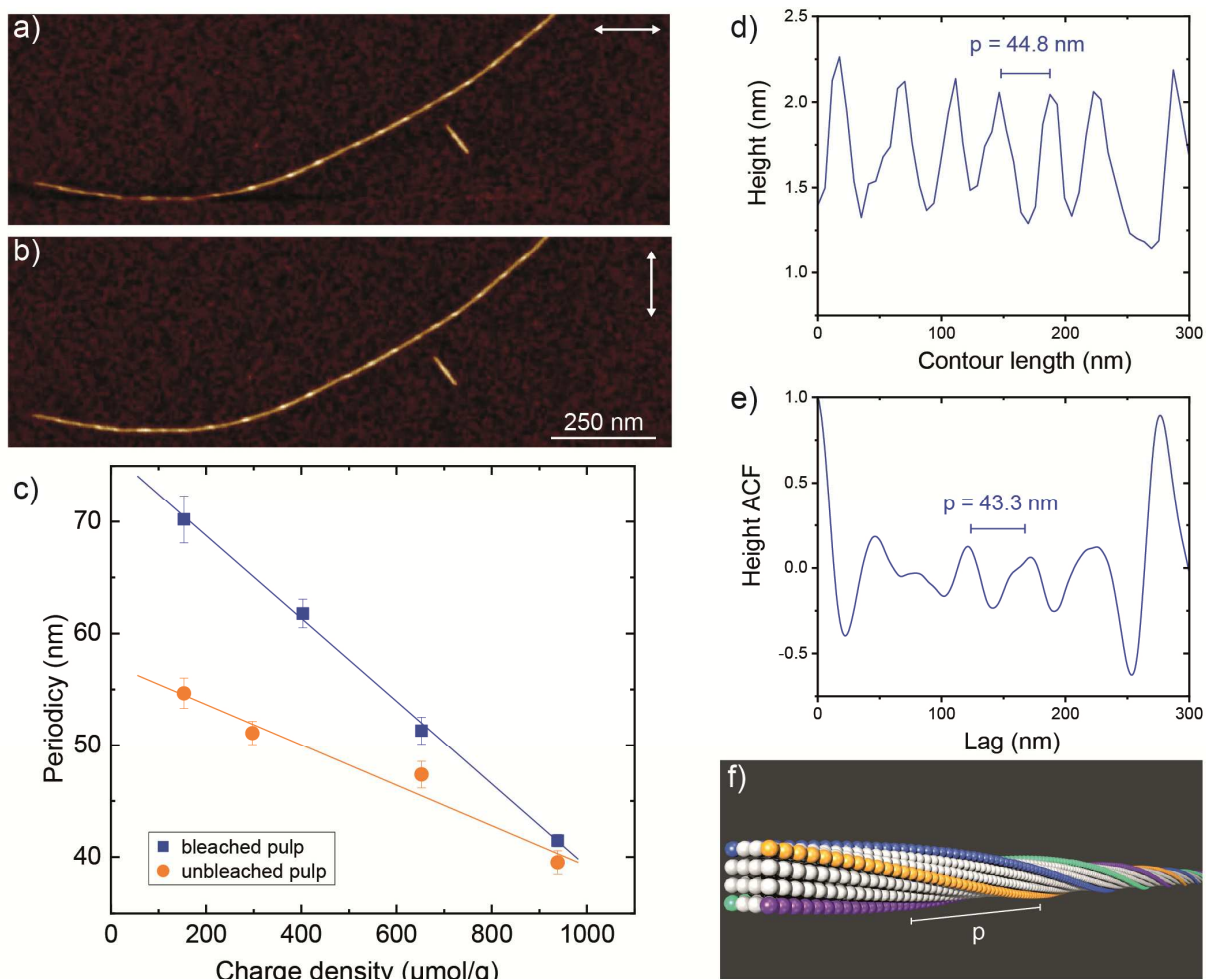


Figure 5. Analysis of the periodicity of the pitch of cellulose fibrils. a) AFM image of a single fibril (unbleached source after 11 min of sonication), where the white line indicates the scanning direction. b) AFM image of the same fibril with 90° turned scanning direction. c) Dependency of periodicity on the charge density of CNFs from bleached (blue square) and unbleached (orange circle) softwood pulp sources, with the respective linear fit. d) Height plot along the contour of a single fibril. e) Plot of the height autocorrelation function (ACF) versus lag of the same fibril contour. f) Schematic of a twisted 4x4-cross section fibril, where the periodicity p is indicated.

CONCLUSIONS

The present study provides insights into the nanostructure of single CNFs resulting from a systematic variation of both chemical and physical parameters, *i.e.*, the industrial treatment of the pulp starting material, the amount of oxidant in the TEMPO-mediated oxidation process and the mechanical treatment (sonication). Using AFM imaging and statistical image analysis, we observed a principal difference in fibrillization between samples from bleached and unbleached softwood pulp, where the unbleached fibrils were generally less charged but longer. However, the length of the individual fibril largely depends on the charge density induced by

the TEMPO-mediated oxidation and the sonication time used to fibrillate the samples. Increasing these two parameters leads to shorter and thinner fibrils. We found an optimum between maximal fibril length and minimal number of kinks at a charge density of around 600 $\mu\text{mol/g}$.

Furthermore, AFM imaging allowed us to resolve the twisting periodicity of individual CNFs. We found a decreasing twist periodicity and decreasing height of the fibrils for increasing charge density. This is in agreement with a model balancing the twist elasticity of the fibrils with the electrostatic repulsion from the fibril charges.^[130,131]

EXPERIMENTAL SECTION

All materials and devices used are listed in the supplementary information.

Synthesis of carboxylated cellulose nanofibrils.

Carboxylated CNF were prepared from bleached and unbleached commercial never-dried sulphite softwood-dissolving pulp (Domsjö, Sweden) by TEMPO-mediated oxidation.^[29] Thereby, the amount of NaClO as oxidation agent was varied between 1.5 up to 10 mmol/g of cellulose in order to obtain pulps with different charge densities. The oxidized cellulose pulp was dispersed in 100 mL Milli-Q water (0.5 g/L), ultra-sonicated (operated at 200 W, 24 kHz, no interval, 20% amplitude, 7 mm probe) for various durations up to 25 min, followed by centrifugation at 4000 RCF for 45 min to remove non-fibrillated cellulose aggregates.

Measurement of charge density.

The charge density was determined by conductivity titration on the oxidized cellulose pulp fibers following the protocol SCAN-CM 65:02. The fibers were dispersed in Milli-Q water to obtain a total volume of 500 mL with a NaCl concentration of 1 mM. The pH was adjusted to 2.5 and stirred for 30 min to protonate all carboxyl groups. The dispersion was thereafter titrated adding NaOH up to pH 10 while the conductivity was recorded. The charge density of the carboxyl groups was then readily obtained from the plateau region of conductivity.

Fibril characterization using atomic force microscopy (AFM).

The freshly cleaved mica was modified with 20 μL of 0.05% (3-aminopropyl)triethoxysilane (APTES) for 60 s to induce positive charges on the surface. A droplet of around 2 mg/L fibril dispersion was deposited on the mica and allowed to adsorb for 30 s before it was rinsed with Milli-Q water and dried with pressurized air. The AFM measurements were conducted in tapping mode under ambient conditions using commercial cantilevers (Bruker) to obtain images

with a resolution of at least 2.9 nm/pixel.

The images were analyzed with FiberApp,^[128] where only single fibrils were considered. In addition, agglomerates and fibrils that showed splitting events were not considered (see SI for further experimental details).

The analysis of the twist periodicity was performed with the height distribution tool implemented in FiberApp, where for each sample 40 straight fibril segments were tracked and the periodicity determined by the average distance between local maxima along to the fibril contour.

Wide-angle X-ray scattering (WAXS).

Small and wide-angle X-ray scattering (SAXS and WAXS) experiments were performed using a Rigaku MicroMax-002⁺ equipped with a microfocused beam (40 W, 45 kV, 0.88 mA) with the $\lambda_{\text{CuK}\alpha} = 0.15418$ nm radiation collimated by three pinhole collimators (0.4, 0.3 and 0.8 mm) in order to obtain direct information on the scattering patterns. The SAXS and WAXS intensities were collected by a two-dimensional Triton-200 gas-filled X-ray detector (20 cm diameter, 200 μm resolution) and a two-dimensional Fujifilm BAS-MS 2025 imaging plate system (15.2×15.2 cm², 50 μm resolution), respectively. An effective scattering vector range of $0.05 \text{ nm}^{-1} < q < 25 \text{ nm}^{-1}$ was obtained, where q is the scattering wave vector defined as $q = 4\pi \sin \theta / \lambda_{\text{CuK}\alpha}$ with a scattering angle of 2θ .

Dynamic light scattering (DLS).

The translational diffusion coefficient was determined by DLS. To minimize particle interactions, the CNF solution was diluted (0.1 g/L) and centrifuged at 12000 RCF for 30 min to remove large agglomerates potentially present in the samples. The fibril length L was calculated assuming that the fibrils behave as rigid rods and using equation 1:^[132,133]

$$D = \frac{kT}{3\pi\eta L} \left(\ln L - \ln d + c_0 + \frac{c_1 d}{L} + \frac{c_2 d^2}{L^2} \right), \quad (3)$$

where D is the translational diffusion coefficient measured by DLS, k the Boltzmann's constant, T the temperature (25 °C), η the viscosity of water, d the fibril diameter determined by AFM and c_0 , c_1 and c_2 are constants (0.312, 0.565 and 0.1, respectively) for cylindrical objects, taken from reference.^[132]

AUTHOR INFORMATION

Corresponding authors

*Email: raffaele.mezzenga@hest.ethz.ch, gustav.nystroem@empa.ch

Author contributions

M.A. and G.N. designed the study. M.A., E.Z., R.A., J.A. and A.S.F. performed the experiments. M.A., E.Z., R.A., J.A., A.S.F., R.M. and G.N. analyzed data. M.A., R.M. and G.N. wrote the paper.

Notes

The authors declare no competing financial interest.

ACKNOWLEDGMENTS

We thank Domsjö, Sweden for providing the softwood pulp and K. Smith for critical reading the manuscript. M. Arcari and G. Nyström acknowledge funding from the Swiss National Science Foundation Ambizione Grant No. PZ00P2_168023/1.

Supplementary Information

Supplementary text

Fibril characterization using AFM

To make sure that we were able to compare the AFM images with as little bias as possible, we only tracked single fibrils without splitting events or thick segments where two or more fibrils overlay. The concentration for the different fibril dispersions used to adsorb the fibrils onto mica was adjusted to guarantee the least possible overlapping. The adsorption on the mica depends on the charge density as well as the sonication time and could be seen as a qualitative measurement for the effectiveness of the fibrillization.

Depending on the sonication time, the number of larger particles (agglomerates and fibrils that split) not taken into account were around 50% for 5 min of sonication. This value declined to around 25% for 17 min of sonication. However, the variation between the data of a completely tracked image (100% of the fibrils) and the data we presented in the paper is lower than 3%.

Supplementary figures

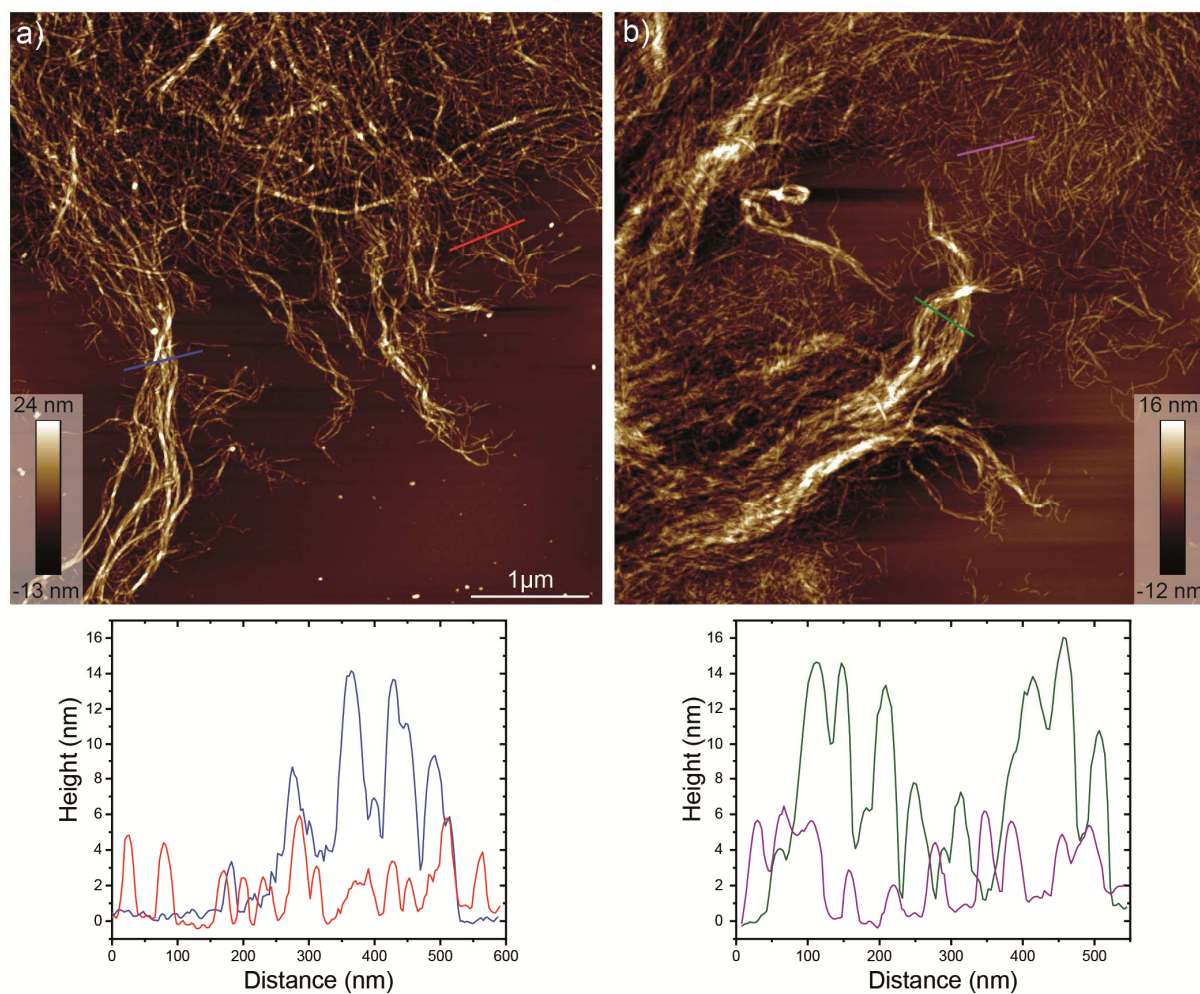


Figure S1. AFM images of TEMPO-mediated oxidized a) unbleached and b) bleached paper pulp without sonication treatment and the corresponding height profiles along the colored lines at the bottom of each image.

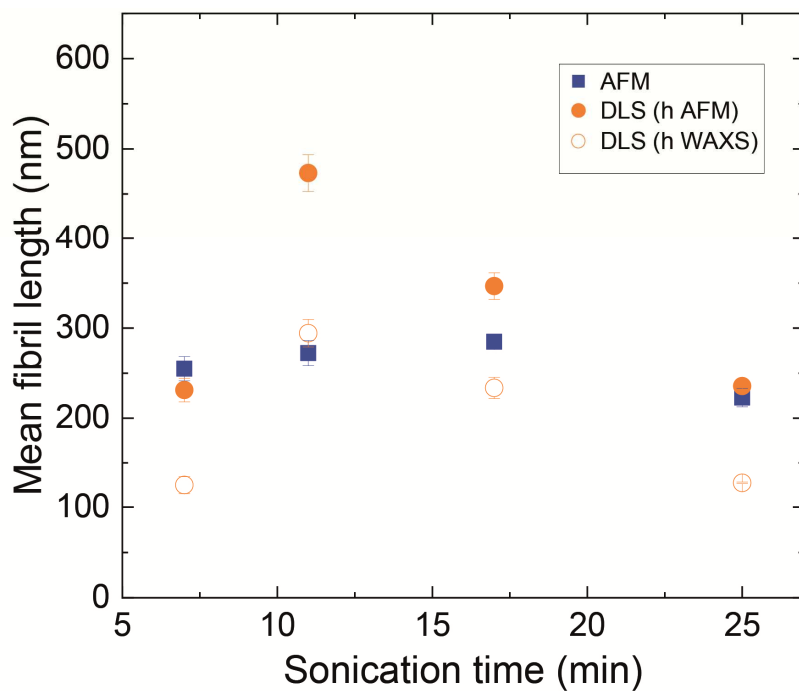


Figure S2. Comparison of mean fibril length between DLS (orange circle) and AFM (blue square) measurements of CNF dispersions prepared from bleached wood pulp with a charge density of 830 $\mu\text{mol/g}$ CNF (standard deviation of DLS of 3 measurements and standard error of AFM $n > 200$). For DLS the height h is taken from either AFM ($h \approx 2$ nm, full circle) and WAXS ($h \approx 4$ nm, empty circle), respectively.

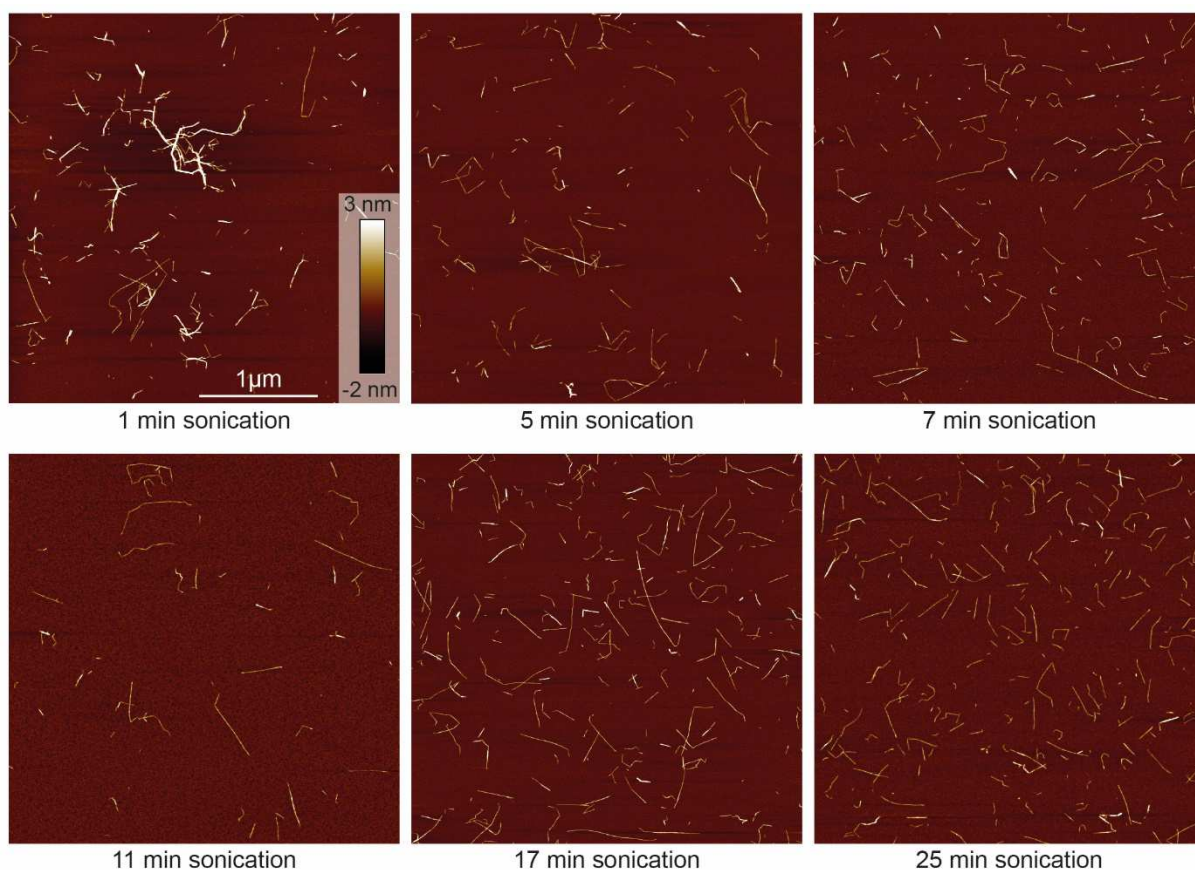


Figure S3. Representative AFM images showing the influence of increasing sonication time on the fibrillation of CNFs from bleached paper pulp with a charge density of $830 \mu\text{mol/g}$.

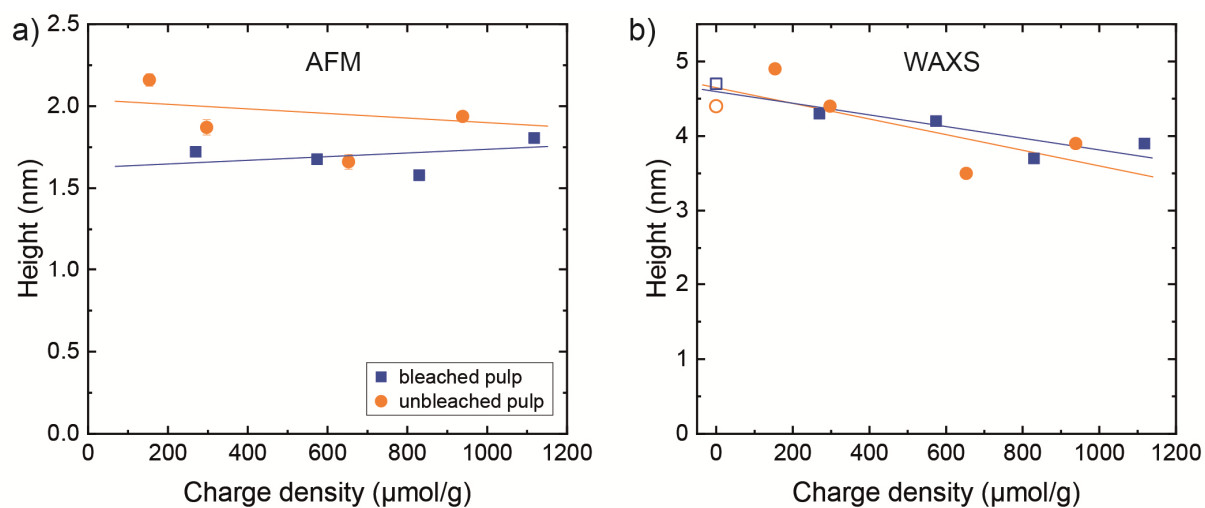


Figure S4. Average fibril height determined by a) AFM and b) WAXS as function of charge density. As zero charge density, WAXS measurements were done with unoxidized and unsonicated pulp (empty points), whereas the other points were done with lyophilized samples from sonicated fibril dispersions.

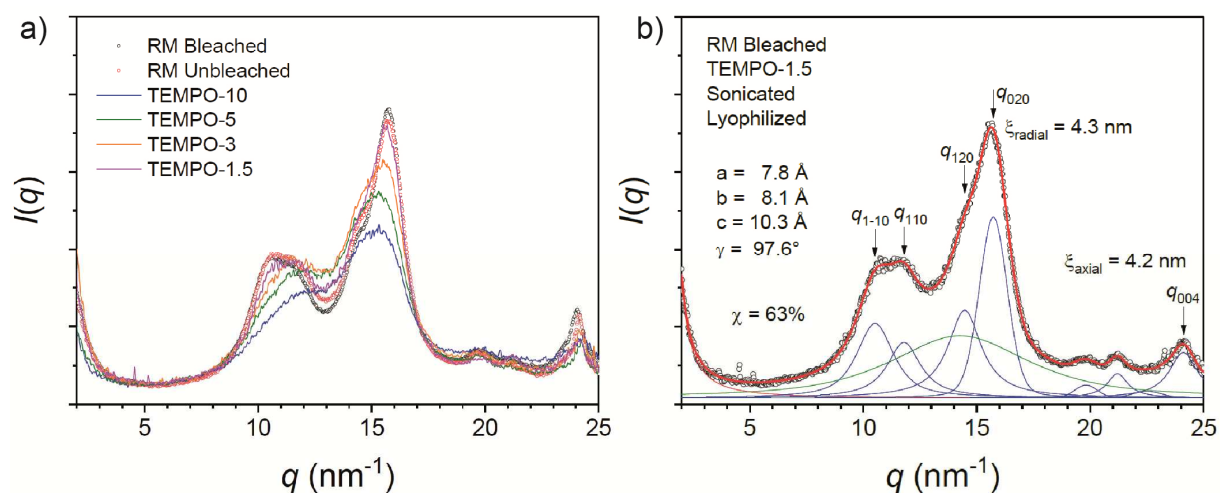


Figure S5. a) WAXS intensity profile of lyophilized bleached and unbleached industrial pulp and four bleached TEMPO-mediated oxidized samples (sonicated and lyophilized). b) Convolution of the WAXS profile of bleached CNF after sonication and lyophilization.

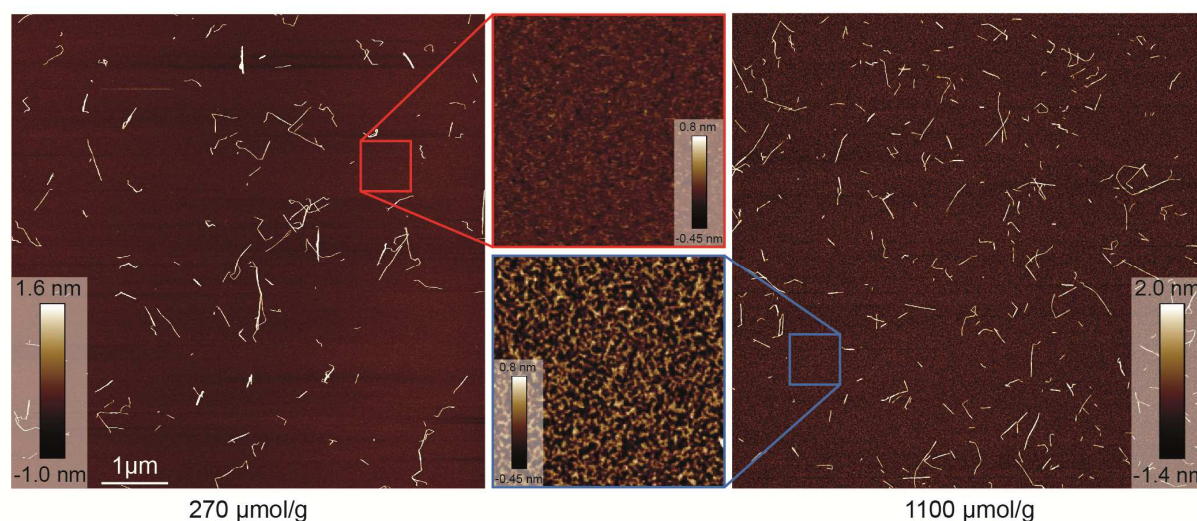


Figure S6. AFM images showing the difference in roughness of the APTES-modified mica surface while adsorbing CNF dispersions with low and high charge density. The roughness is coming from negatively charged single cellulose polymer chains.

Table S1. Parameters obtained from AFM image analysis and DLS for all different CNF samples.

Sample name*	Mean length (nm)	stdE	Length weighted length (nm)	stdE	Mean length (nm, DLS)	Inverse kink density	Average segment length (nm)	Number of kinks per fibril	Average height (nm)	stdE	Charge density ($\mu\text{mol/g}$)
1.5bl 05min	281	27	680	43		180	110	1.56	1.9	0.02	270
1.5bl 07min	332	23	671	33		177	116	1.87	1.7	0.02	270
1.5bl 11min	342	20	592	27		181	118	1.89	1.7	0.01	270
1.5bl 17min	313	27	560	36		183	116	1.71	1.6	0.02	270
1.5bl 25min	323	18	528	23		191	120	1.69	1.6	0.02	270
3bl 05min	352	31	715	44		228	138	1.54	1.9	0.02	570
3bl 07min	265	22	623	34	548	247	128	1.07	1.5	0.02	570
3bl 11min	292	11	567	15	422	239	132	1.22	1.7	0.01	570
3bl 17min	300	16	551	21	325	248	136	1.21	1.6	0.01	570
3bl 25min	327	10	544	13	329	234	136	1.40	1.5	0.01	570
5bl 05min	212	16	431	23		282	121	0.75	1.5	0.03	830
5bl 07min	255	14	496	19	231	231	121	1.10	1.7	0.01	830
5bl 11min	272	14	486	19	473	257	132	1.06	1.6	0.01	830
5bl 17min	285	7	476	9	347	286	143	1.00	1.7	0.01	830
5bl 25min	223	10	373	13	236	223	111	1.00	1.5	0.01	830
10bl 05min	234	18	388	23		254	122	0.92	1.7	0.03	1100
10bl 07min	205	9	342	12	343	321	125	0.64	1.9	0.01	1100
10bl 11min	204	8	339	10	403	340	127	0.60	1.8	0.01	1100
10bl 17min	185	6	323	8	338	349	121	0.53	1.6	0.01	1100
10bl 25min	199	6	304	8	189	343	126	0.58	1.7	0.01	1100
1.5ubl 05min	518	47	1098	69		193	141	2.69	2.0	0.02	150
1.5ubl 07min	493	30	885	40		207	146	2.38	1.9	0.01	150
1.5ubl 11min	468	32	774	41		216	148	2.17	2.1	0.02	150
1.5ubl 17min	447	30	746	39		208	142	2.15	2.2	0.02	150
1.5ubl 25min	390	22	624	28		177	122	2.21	1.9	0.02	150
3ubl 05min	553	60	1101	84		292	191	1.90	1.4	0.02	230
3ubl 07min	547	27	966	36	375	325	204	1.68	1.8	0.01	230
3ubl 11min	454	23	819	31	340	253	163	1.79	1.8	0.01	230
3ubl 17min	439	25	723	33	346	277	170	1.58	1.5	0.02	230
3ubl 25min	385	15	564	18	259	236	146	1.63	1.5	0.01	230
5ubl 04min	552	50	1285	77		396	231	1.39	1.7	0.02	650
5ubl 05min	482	29	922	41		389	215	1.24	1.5	0.02	650
5ubl 07min	493	38	935	52	338	356	207	1.38	1.5	0.02	650
5ubl 11min	459	24	774	31	383	303	183	1.51	1.4	0.01	650
5ubl 17min	400	22	686	28	332	321	178	1.25	1.3	0.01	650
5ubl 25min	335	13	529	16	215	320	164	1.05	1.7	0.01	650
10ubl 05min	329	26	628	36		323	163	1.02	1.7	0.02	940
10ubl 07min	294	14	473	18	456	436	176	0.67	1.4	0.01	940
10ubl 11min	268	17	520	24	459	411	162	0.65	1.2	0.01	940
10ubl 17min	288	10	453	13	412	523	186	0.55	1.4	0.01	940
10ubl 25min	264	9	405	11	253	477	170	0.55	1.5	0.01	940

*The sample name is compound from: amount of NaClO [mmol/g cellulose]; bleached (bl) or unbleached (ubl); sonication time. 3 bl 11min = 3 mmol NaClO per g cellulose, bleached pulp, 11 min sonication.

Supplementary material and methods

Materials and chemicals

If not stated otherwise, the chemicals were obtained by Sigma Aldrich and used without further purification. Bleached and unbleached never-dried sulphite softwood-dissolving pulp was obtained by Domsjö, Sweden. The degree of polymerization (DP) of both pulps was around 770, determined by Domsjö.

Instrument list

Ultra-sonicator:	Hielscher UP200S
DLS:	Zetasizer Nano ZS, Malvern Instruments Ltd. U.K.
Centrifuge:	Centrifuge 5810 R, Eppendorf Prism Microcentrifuge, Labnet Sigma 3K3OH, Sigma
Charge density:	Conductivity meter EL30/EL3, Mettler Toledo
AFM:	MultiMode VIII Scanning Probe Microscope, Bruker, USA
WAXS:	Rigaku MicroMax-002 ⁺ , Rigaku Innovative Technologies, Auburn Hills, Michigan, USA

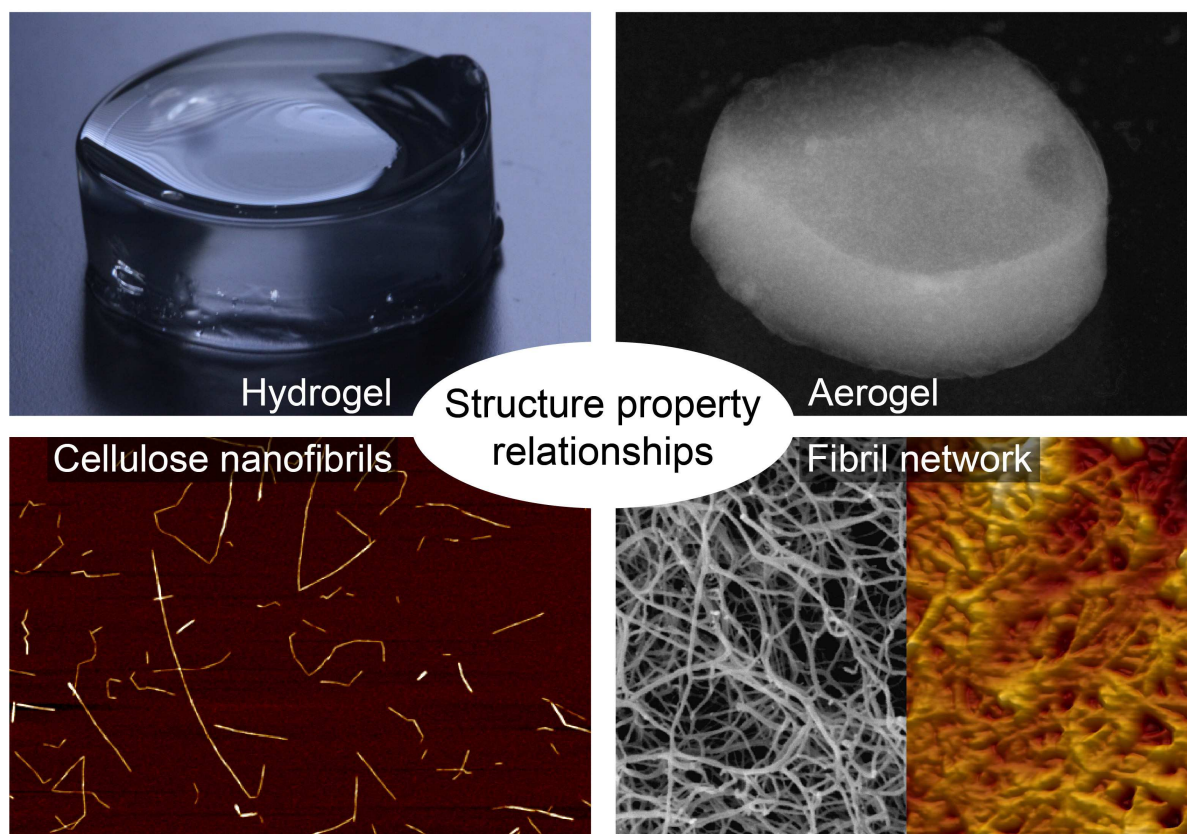
Structure property relationships of cellulose nanofibril hydro- and aerogels and their building blocks

Mario Arcari, Robert Axelrod, Jozef Adamcik, Stephan Handschin, Antoni Sánchez-Ferrer, Raffaele Mezzenga, and Gustav Nyström

Nanoscale 2020, 14-19

<https://doi.org/10.1039/D0NR01362E>

Reprinted from reference ^[134] with permission from The Royal Society of Chemistry.



Structure property relationships of cellulose nanofibril hydro- and aerogels and their building blocks

Mario Arcari¹, Robert Axelrod¹, Jozef Adamcik¹, Stephan Handschin¹, Antoni Sánchez-Ferrer¹, Raffaele Mezzenga^{1,2}, and Gustav Nyström^{1,3*}*

1. ETH Zurich Department of Health Science and Technology, Schmelzbergstrasse 9, LFO E23 Zurich 8092, Switzerland.
2. ETH Zurich, Department of Materials, Wolfgang-Pauli-Strasse 10, 8093 Zurich, Switzerland.
3. EMPA, Laboratory for Cellulose & Wood Materials, Überlandstrasse 129, 8600 Dübendorf, Switzerland.

*Correspondence to: raffaele.mezzenga@hest.ethz.ch, gustav.nystroem@empa.ch

As abundant and renewable material with excellent mechanical and functional properties, cellulose nanomaterials are utilized in advanced structural, optical and electronic applications. However, in order to further improve and develop new cellulose nanomaterials, a better understanding of the interplay between the self-assembled materials and their building blocks is crucial.

This paper describes the structure property relationships between cellulose nanofibrils (CNF) and their resulting self-assembled structures in the form of hydrogels and aerogels. Rheological experiments revealed that the transition from viscous to elastic state with the corresponding evolution of the properties of the CNF dispersion depends on the aspect ratio and can be described in terms of the dynamic overlap concentration. The elastic shear modulus was dependent on the aspect ratio at very low CNF concentrations, reaching a plateau, where only the concentration of CNFs was relevant. This transition point in shear modulus was exploited to determine the mesh size of the fibril network, which was found to be in excellent agreement with predictions from scaling arguments. These findings highlight the possibility to tune the self-assembled materials response directly from the bottom-up by the CNF particle structure and thus, suggest new assembly routes starting directly from the CNF design.

Introduction

Super lightweight aerogels from renewable resources are of general scientific and industrial interest for a wide range of applications including thermal insulation, filtration and gas sorption.^[135] Due to the abundance of cellulose originating from plant materials and the increasing availability as a result of the improvements and upscaling of the production of cellulose nanomaterials, this natural polymer has a large potential. This potential has already been recognized and led to a vast amount of research in the field of cellulose materials, providing numerous new applications and accessing more sustainable production methods.^[2,49] In order to further develop these materials and optimize functionality, it is however critical to better understand the mechanism of self-assembly of the anisotropic nanoparticles into materials with different hierarchical levels.^[11]

The formation of porous cellulose materials can be achieved in different ways, where the most studied use freeze drying and supercritical CO₂ drying of aqueous cellulose nanoparticle dispersions to obtain cryo- and aerogels, respectively.^[70,71,73,78,79,136] Pores of cryogels are templated by the formation of ice crystals and can, depending on the control of the freezing process, show lamellar-like or cellular organization. Instead, for aerogels, the network structure is built by a physical or chemical crosslinking step to form hydrogels before solvent exchange and supercritical CO₂ drying. In this case, concentration and particle properties such as aspect ratio and surface charge density are of significance for the network formation. Aqueous nanocellulose dispersions are typically stabilized by electrostatic repulsion coming from deprotonated acidic groups, such as carboxylates or sulfates, on the fibril surface at neutral pH. Protonation or screening of the surface charges due to addition of ions destabilizes the colloidal dispersions and a physical network can be formed.^[69,79,133,137–140] Rheology provides a facile option to compare the properties of dispersions as well as hydrogels, and, in combination with the knowledge of the nanoparticle characteristics, allows insight into structure property relationships at the different length scales.^[114,140–142]

The recent focus of nanocellulose aerogel research has been primarily on pioneering applications, whereas the fundamental understanding of the hydrogel- and aerogel-formation mechanisms was less emphasized. Recently gained knowledge indicates, however, that the source material out of which the nanoparticles are produced influences the properties of the resulting materials more than initially assumed.^[58] Taking this understanding into account, a systematic investigation of the correlation between the properties of single fibrils and the formation and properties of self-assembled higher order systems is highly relevant and still missing.

Saito and Isogai developed a protocol to produce aqueous CNF dispersions using TEMPO-

mediated oxidation that, at optimal conditions, yields transparent dispersions with individualized CNFs.^[29] Though successful at the lab scale, upscaling this process to make it accessible for industry will likely require compromises in material properties in favor of economic feasibility.^[56]

In this study, we investigated the formation of physical networks in nanocellulose hydrogels and the resulting aerogels after supercritical CO₂ drying, while systematically altering CNF properties such as length and charge density. Additionally, we compare the influence of cellulose pulp concentration on the fibrillization and its impact on the CNF dispersion and the resulting hydrogel and aerogel structures. We study the rheological behavior of CNF dispersions as well as the physical network formation due to protonation and charge screening. Finally, the nanostructure of the aerogels is analyzed by scanning electron microscopy (SEM) and atomic force microscopy (AFM).

We found that fibril properties are affected by the initial cellulose pulp concentration during sonication, which further impacts the optical properties of the resultant hydro- and aerogels. Furthermore, the dynamic overlap concentration not only describes optimal fibrillization conditions, but also the transition from viscous to elastic behavior of CNF dispersions. Investigating the gelation at different concentrations and analyzing it using polymer physical considerations revealed a distinct dependency of the elastic shear modulus G' on the aspect ratio of CNFs at low concentrations (0.06 wt%) and lower aspect ratios. The transition point of the aspect ratio, at fixed fibrils concentration, where the elastic shear modulus becomes independent on the aspect ratio can further be used to approximate the mesh size of the CNF networks.

Result and Discussion

Influence of initial pulp concentration on fibrillization.

The major influences on mechanical disintegration of single CNFs are the energy input during the fibrillization and the repulsion between the individual CNFs due to their surface charge density.^[43,44,109] However, as can be observed in **Figure 1**, the cellulose concentration during the mechanical disintegration also plays an important role. The fibrillization of the pulp into individualized objects worked well for cellulose concentrations below 0.1 wt% (Figure 1a,b), whereas with increasing concentration the fibrillization seemed to be less efficient and bundles and aggregates remained in the dispersion (Figure 1c). From these images, we can assume that the critical concentration C^* for the fibrillization is somewhere between 0.1 and 0.6 wt%. This effect is not only observable on the nanoscale. Dispersions with a cellulose concen-

tration higher than C^* appeared turbid to the naked eye after 11 min of sonication (Figure 1e). Optical light microscopy observations revealed still intact cellulose fibers and large fragments, of which the majority could be removed by extensive centrifugation at 12000 rcf for 90 min (Figure S1). These findings go in line with turbidity measurements previously used for nanocellulose width estimations.^[143] Experimentally, C^* can be determined through screening various CNF concentrations, which, however, is labor-intensive and a theoretical approach towards determining the critical concentration is desirable.

At low concentrations, dispersed and distinct fibrils do not, or only weakly, interact. In polymer physics, this effect is described by the dilute or the semi-dilute regime, respectively. It is thought that the static properties of these two regimes are similar, whereas the dynamic properties of the semi-dilute regime is affected by interactions between particles.^[144] The transitions between the different regimes can be approximated by the excluded volume using the aspect ratio a . In the static state, the transition from the semi-dilute to the concentrated regime follows a^{-2} .^[144] However, in the dynamic system, the transitions from dilute to semi-dilute ϕ_{sd} and further to concentrated regimes are shifted and the boundaries are described by the following equation:^[145]

$$a^{-2} \ll \phi_{sd} \ll a^{-1} \quad (1)$$

The upper boundary sets, the onset of liquid crystalline interactions as predicted by Onsager based on excluded volume overlap. As the mechanical disintegration is a rather dynamic process, we consider overlap of excluded volume, and thus, we take the upper boundary as an approximate dynamic overlap concentration of the CNFs. Using **Equation 1**, one can calculate the dynamic overlap concentration C^{**} in wt% as

$$C^{**} = a^{-1} \rho = \frac{d}{L_w} \rho, \quad (2)$$

where d is the fibril diameter, L_w the length weighted fibril length and $\rho = 1.5 \text{ g cm}^{-3}$ the density of cellulose. In the case of the sample presented in Figure 1, the calculated $C^{**} = 0.34 \text{ wt\%}$ lies in the range of concentration assumed earlier from the images.

For the present study, six samples of CNFs with varying aspect ratio and surface charge density were investigated. Three samples originated from a bleached softwood paper pulp and three from an unbleached softwood paper pulp, respectively. **Table 1** provides an overview of the fibril properties, where L_w is the average length-weighted length, L the average fibril length, a the aspect ratio, CD the charge density, d_{eff} the effective diameter and C^{**} the dynamic overlap concentration.

Table 1. Particle dimension, surface charge density (CD), effective diameter, inverse kink density, and dynamic overlap concentration.

	3 bl	5 bl	10 bl	3 ubl	5 ubl	10 ubl
L_w (nm) ^a	567	486	339	819	774	520
L (nm)	292	272	204	454	459	268
a (L_w/d) ^b	323	277	193	467	441	296
CD ($\mu\text{mol/g}$) ^c	574	830	1118	297	653	938
d_{eff} (nm)	19.7	21.0	23.9	15.3	19.8	23.2
Inverse kink density (nm) ^d	239	257	340	253	303	411
C^{**} (wt%)	0.46	0.54	0.78	0.32	0.34	0.51

^a Length weighted length, ^b the average height of all samples is taken (1.76 nm), ^c conductometric titration of the TEMPO-pulp, ^d described in ref. [46]. *Note:* bl = bleached, ubl = unbleached, the number accounts the amount of NaClO per gram cellulose during the TEMPO-mediated oxidation. Data collected from ref. [109].

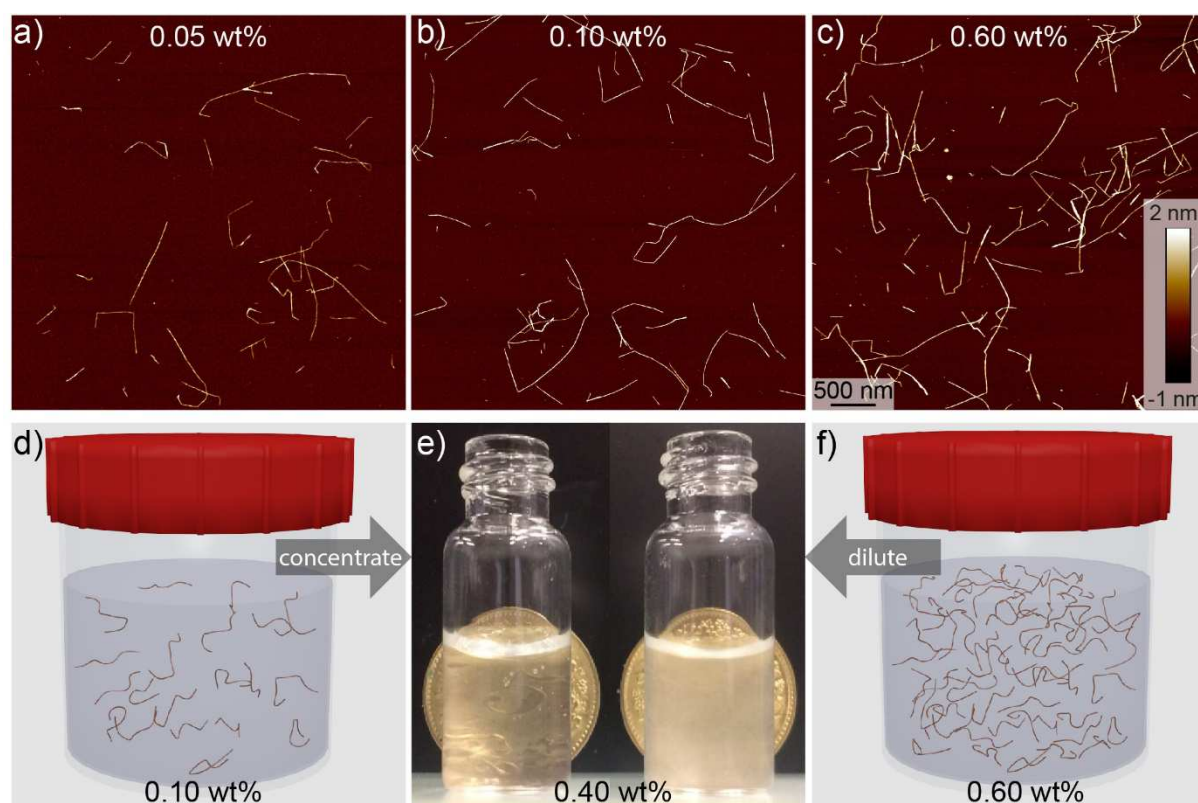


Figure 1. Influence of initial pulp concentration on fibrillization. a-c) AFM images T-CNFs (5 mmol NaClO/g cellulose from unbleached pulp) with varying starting concentration after 11 min of sonication. Schematic of fibrillated CNF dispersions d) below and f) above the dynamic overlap concentration and e) photographs of the transparent and turbid dispersions after sonication and adjustment of the concentration to a final 0.40 wt%.

Effect of aspect ratio on CNF dispersion properties.

Rheological experiments provide insights into the behavior of the CNF dispersions under shear conditions. The aspect ratio and the surface charge density that define the effective diameter d_{eff} (Table 1) determine the excluded volume of the CNFs, a parameter that is important when the system becomes ordered due to shear alignment or increasing concentration.^[142,146] **Figure 2** shows only weak effects of alignment due to increasing shear for 0.06 wt% CNFs, however, distinct shear thinning is found at 0.40 wt%, whereas increasing aspect ratio leads to more viscous dispersions. The aspect ratio of CNFs is dependent on the charge density,^[43,109] this means the charge density determines how efficient the fibrils are mechanically individualized and then further break into shorter fibrils. Nevertheless, with the available data, it was difficult to distinguish these two properties (aspect ratio and charge density) separately. In Figure 2, one observes a non-linear increase in viscosity with the aspect ratio, which could be a result of the charge density. Furthermore, there were only small differences in viscosity between the transparent (individual CNF) and the turbid (branched CNF) dispersions (see Figure S2).

Dynamic frequency sweep experiments at 0.40 wt% without the addition of ions showed a transition from viscous behavior for low aspect ratio fibrils to elastic properties while increasing the aspect ratio (**Figure 3a**). For concentrated transparent dispersions with individualized CNF, this transition occurred at an aspect ratio $a \approx 300$. Interestingly, the transition can be described using the dynamic overlap concentration C^{**} determined by **Equation 2** (Figure 3b).

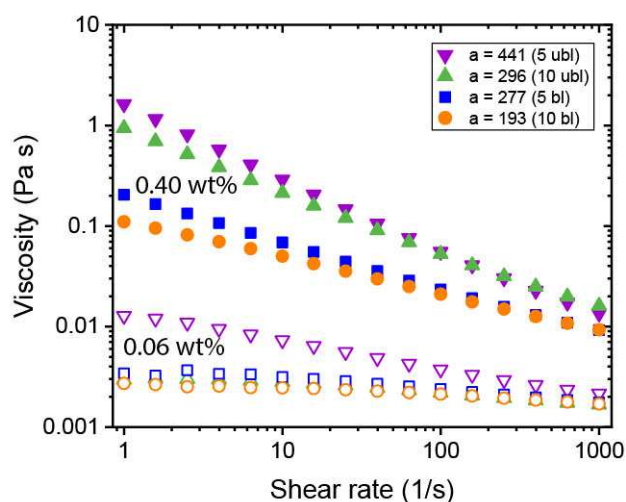


Figure 2. Rheological behavior of CNF dispersions with different fibril aspect ratio a . Measurements were done using a double gap geometry with CNF dispersions of 0.40 wt% (full) and 0.06 wt% (empty).

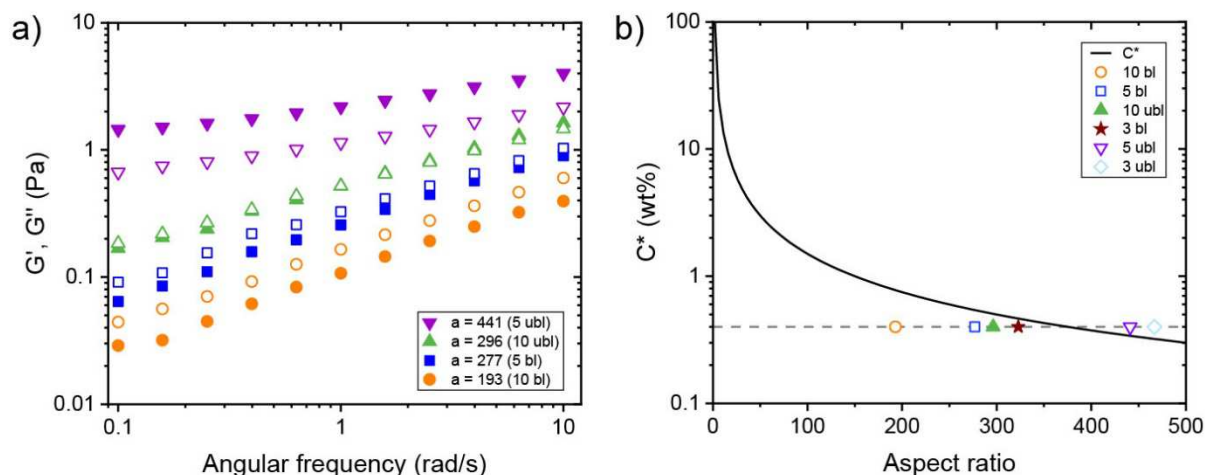


Figure 3. Viscoelastic properties of CNF dispersions around the dynamic overlap concentration (C^{}).** a) Storage shear modulus G' (full symbols) and loss shear modulus G'' (empty symbols) as a function of the shear frequency ω at constant strain ($\gamma = 0.5\%$) and temperature ($20\text{ }^\circ\text{C}$) for CNF dispersions ($0.40\text{ wt}\%$) with different aspect ratio a . b) Relationship of C^{**} vs aspect ratio of the examined CNF dispersions, where the full triangle and star represent the samples with $G' \sim G''$, the empty circle and square $G' < G''$ and the empty triangle and diamond $G' > G''$. The dashed line highlights the experimental concentration at $0.40\text{ wt}\%$.

Rheological properties of hydrogels.

The destabilization of CNF dispersions and thereby formation of physical networks induced by protonation or charge screening using NaCl is extensively discussed in literature.^[69] Due to the ability of CNFs with protonated surface charges to still form hydrogen bonds, these networks are much stronger than those induced by charge screening (see **Figure 4** and Figure S3 for plots of the G' and G'' values across the measured angular frequency ω range). The increase in elasticity with increasing concentration is also well described.^[141] Thereby, the elastic properties of the physical gels are generally dependent on the concentration and should be independent of the aspect ratio of its building blocks.^[147] However, approaching the minimal CNF concentration that still led to gel formation, the aspect ratio came into play. In Figure 4a, we observe the evolution of a plateau for higher aspect ratio fibrils at low concentrations (0.06 and $0.07\text{ wt}\%$) as expected based on the fixed concentration. However, below the threshold of an aspect ratio of 320 , the elasticity decreased. In this regime, the fibrils are too short to entangle and efficiently form a network. Thus, we suggest that the transition from the regime, where the elasticity is dependent on the aspect ratio towards the plateau (independent of aspect ratio) can be used to approximate the mesh size ξ of the network. For the fibrils to form an effective steric network, more than a single contact with one other fibril is needed. Thus, the entanglement length L_m of the fibrils at a certain concentration must be longer than the

mesh size and can be assumed as the fibril contour length L at transition point (kink in G') in Figure 4a. For stiff fibrils ($L_p \gg L$), the mesh size ξ can be described by the following relation.^[148]

$$\xi = \sqrt{\frac{2L_m^3}{3L_p}} \quad (3)$$

Taking the contour length ($L \approx L_m$) of the sample at the kink in G' in figure 4a ($L = 292$ nm) and a persistence length of $2.5 \mu\text{m}$ ^[45] yields a mesh size of 81 nm. Comparing this result from experimentally determined values with scaling arguments for rod-like particles, $\xi \sim d\phi^{-\frac{1}{2}}$, where ϕ is the volume fraction of cellulose at 0.06 wt% (0.0004), a mesh size of 88 nm is found in excellent agreement with the experimentally obtained value.

For physical networks induced by NaCl (Figure 4b), the data becomes much more scattered than those obtained from the systems controlled by HCl (Figure 4a). The screening of the surface charges might be influenced by impurities in the CNF dispersions, such as residual ions and polymers present due to the production of CNFs. Distinguishing between samples from the bleached and unbleached source at 0.40 wt%, the elastic shear modulus G' seems to be independent of the aspect ratios as observed by protonation. However, there seems to be a difference between CNFs from the bleached and unbleached source, respectively. As already observed in the case of network formation by protonation at low CNF concentration, below a certain threshold (interpreted as the mesh size), the fibril length influences the elasticity of the network. In the case of salt induced gelation, we cannot observe the formation of a plateau in the tested range, which indicates a looser network with a mesh size probably larger than that achieved by the networks formed by protonation. Significant differences in the rheological behavior between transparent and turbid dispersions could not be observed (Figure S4).

In the case of protonation, comparing the elastic shear modulus G' with the aspect ratio and the charge density (Figure S5), we do not observe a difference in behavior coming from the sample source. However, the experiment with charge screening using NaCl encourages to have a closer look to find a difference in behavior of the two starting materials.

As discussed earlier, the contour length L needs to be longer than the mesh size ξ for a stiff fibrillar network in order to provide enough crosslink points. ξ is mainly dependent on the concentration. In the case of low concentrations, where $L < \xi$, other factors must determine the elastic properties of networks, such as entanglement and the interparticle interactions. In our rheological experiments, we were not able to decouple the contour length from the charge density. Therefore, we focused on the entanglement. In polymers, the

ability to entangle is given by the chain flexibility, as well as the chain length. It was shown that very short fragments of semiflexible polymers behave like rod-like, stiff particles,^[149] so the contour length surely plays an important role. Additionally, the recent advances towards a fibril model with a crystalline core and an amorphous shell would favor a more stiff than flexible fibril conformation.^[99,150,151] Kinks are defects along the fibril contour and, although it still remains to be studied whether the kinks are fixed in position or freely moving, they might be considered as sites that increase entanglement, since they decrease the excluded volume and so the tendency of rod-like object to align. The inverse kink density takes both parameters, contour length and amount of kinks per fibril into account.^[46] An increasing inverse kink density results from fewer kinks within a given fibril contour and thus, a more rod-like CNF appearance. **Figure 5** shows that for low concentrations a lower inverse kink density (higher density of kinks) results in stiffer gels, which is interpreted to result from the higher degree of entanglement in these networks. Moreover, Figure 5 indicates a dependency of G' on the CNF source, where the linear fits of the samples from the unbleached (dotted line) and bleached (dashed line) have a different slope. We can conclude that CNFs from the two sources have different capabilities for entanglement, where the CNFs produced from the unbleached pulp result in stronger gels at lower concentrations than the CNFs from the bleached source.

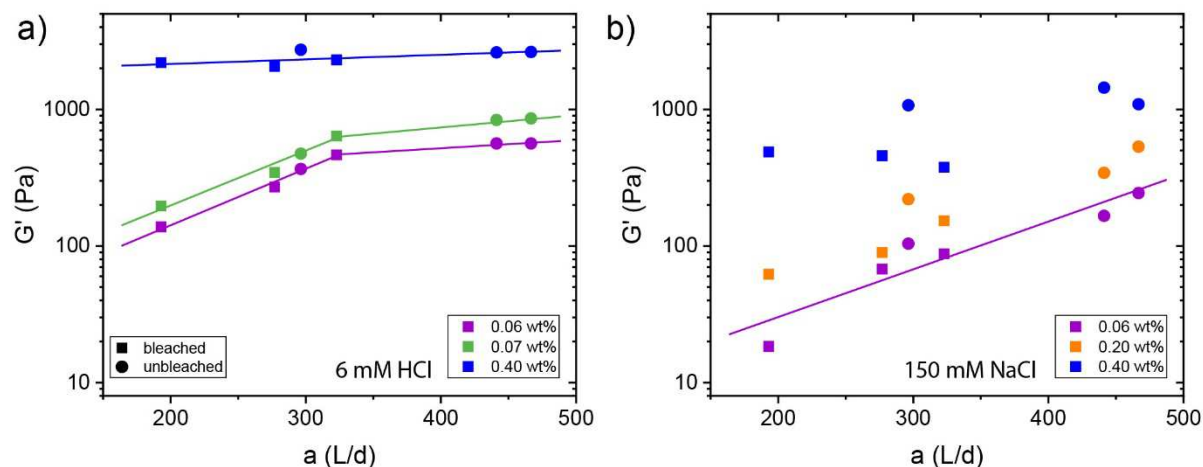


Figure 4. Dependence of the elastic shear modulus G' on aspect ratio of the physical gels at $\omega = 1$ rad/s, $\gamma = 0.5\%$ and 20°C for different concentrations after adding a) 6 mM HCl and b) 150 mM NaCl. The colors indicate different concentrations and the squares and circles represent CNFs from bleached and unbleached pulps, respectively.

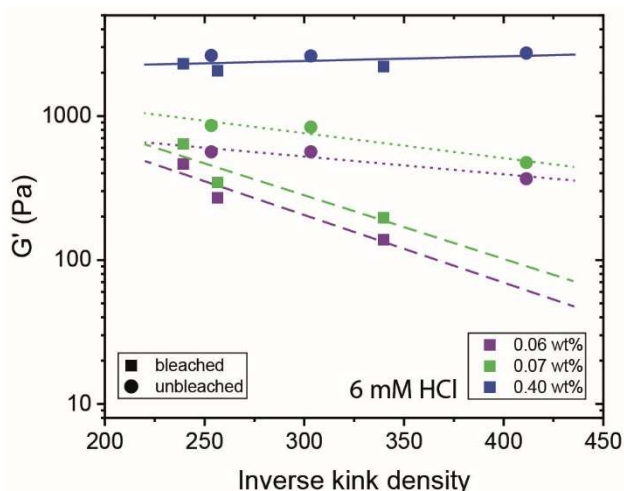


Figure 5. Dependence of the elastic shear modulus (G') of gels on the inverse kink density of CNF at $\omega = 1$ rad/s, $\gamma = 0.5\%$ and 20 °C for different concentrations after adding 6 mM HCl. The colors indicate different concentrations and the dashed and dotted lines (linear fit) represent CNFs from bleached and unbleached pulps, respectively and the continuous line is the linear fit for both samples.

From hydrogel to aerogel.

For macroscopic gelation, where gravity sets a threshold for self-supporting hydrogels, the inversion test allows investigating the ability of self-sustaining structures.^[69] In analogy to our rheological experiments, Figure S6 suggests a dependency of the gelation on the aspect ratio, where the threshold for gelation was observed around $a \approx 280$ for the addition of NaCl. Furthermore, the addition of either HCl or NaCl did not influence the translucency of the hydrogels, in contrast to previous observations.^[152]

Aerogels were produced by supercritical CO_2 -drying of hydrogels after solvent exchange to pure ethanol. A well-described problem in this process is shrinkage. Aerogels produced from low concentration CNF dispersions (~ 0.05 wt%) shrunk around 50%, whereas we found only 30% shrinking for aerogels formed from higher concentrations (0.40 wt%). The shrinkage could be slightly reduced by increasing the time for solvent exchange and adding additional solvent exchange steps. Within a few days, storage at room conditions led to further shrinkage of the aerogels, possibly due to capillary forces within the hygroscopic CNF network. Additionally, the aerogels showed poor resistance against skin contact, probably due to moisture uptake from the skin, which for the present formulations makes CNF aerogels unsuitable as a construction material. These unfavorable material properties made it impossible to conduct experiments to study mechanical properties of the aerogels.

The optical properties of the aerogels obtained after supercritical CO_2 -drying are inherited from the precedent hydrogels (**Figure 6**). The aerogels produced from the transparent CNF

dispersions stayed highly transparent and homogeneous in their macroscopic appearance, whereas the aerogels from turbid CNF dispersions strongly scatter light and show a less homogeneous network structure as observable by eye.

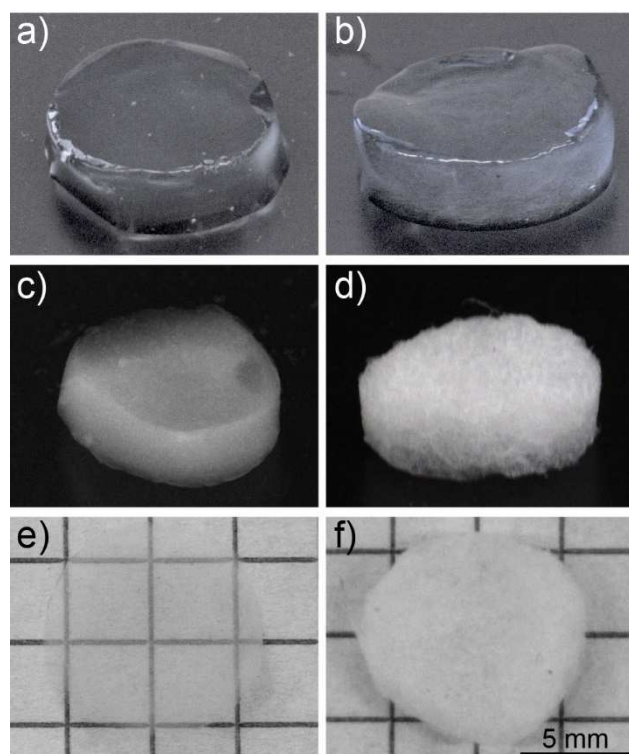


Figure 6. Macro-scale appearance of hydrogels and aerogels. Left row: a) hydrogel and c), e) aerogels produced from concentrated transparent CNF dispersion (0.40 wt%). Right row: b) hydrogel and d), f) aerogels produced from diluted turbid CNF dispersion (0.40 wt%).

To better understand the network formation of the aerogels, we performed SEM and AFM on aerogels from transparent and turbid dispersions to study their respective morphology on the nanoscale. Both methods did not allow seeing significant variations between aerogels produced from different aspect ratio fibrils. However, there were differences between aerogels produced from transparent and turbid dispersions.

SEM revealed networks with mainly single fibrils that form the backbones of the network for the transparent aerogels (**Figure 7a**). In contrast, the backbones of the network in turbid aerogels showed more aggregated fibrils with dangling ends that might originate from only partly individualized aggregates after sonication (Figure 7b). Moreover, the AFM images in Figure 7c-f reveal network backbones that are much broader than the network structure of the transparent aerogels. Additionally, the AFM images suggest a less dense network of the turbid aerogels compared to the transparent aerogels.

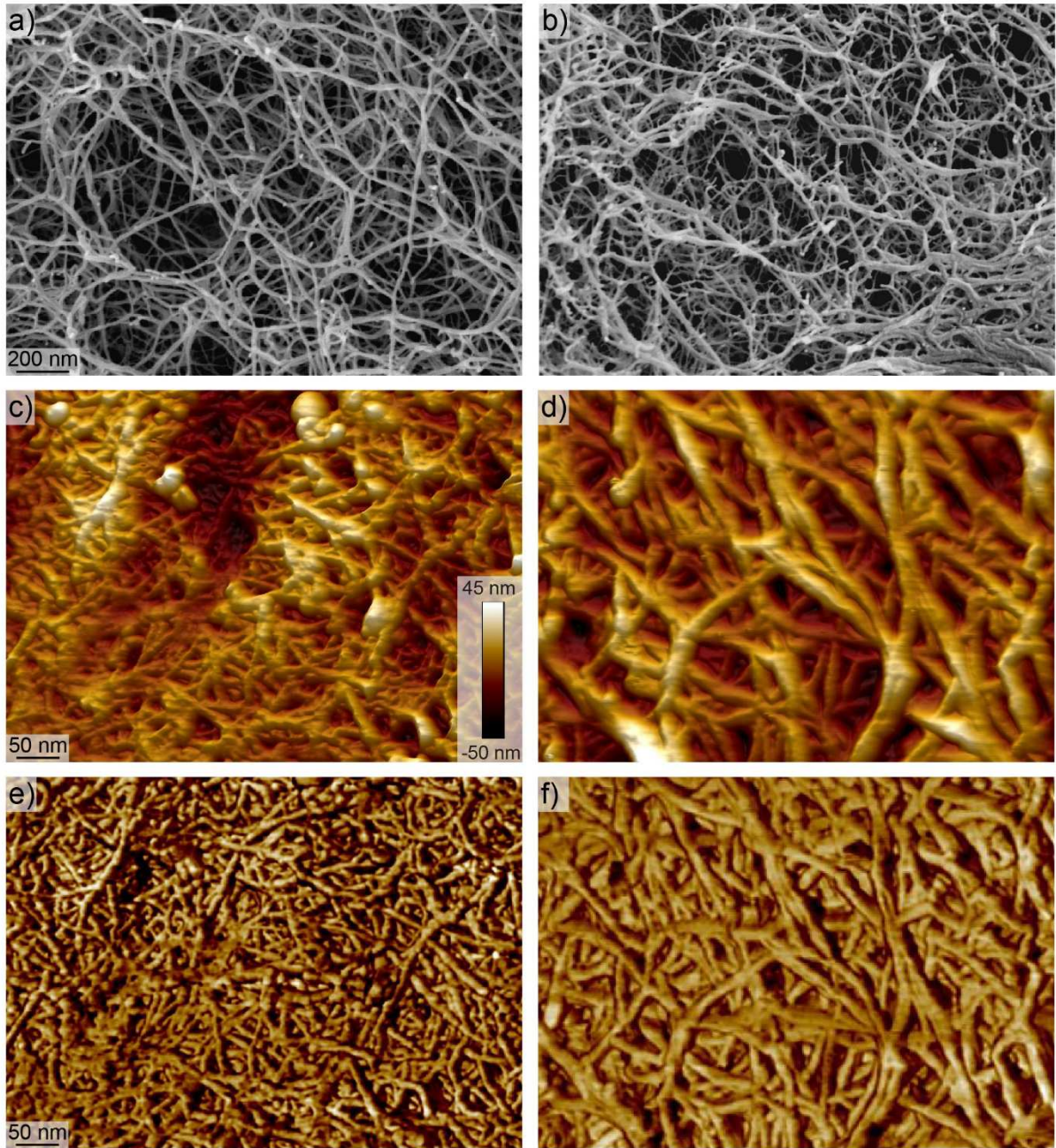


Figure 7. Comparison of aerogel morphologies by SEM and AFM. SEM image of the aerogel produced from a) the transparent and b) the turbid dispersion at 0.40 wt%. c,d) 3D AFM height image and e,f) AFM image of aerogels produced from transparent and turbid dispersions, respectively.

Conclusion

We have shown that the cellulose concentration has a major impact on the fibrillization of CNFs and that mechanical disintegration by sonication is limited by the dynamic overlap concentration C^{**} of the CNF dispersion. The desired single CNF dispersions with a small amount of only partially fibrillated cellulose can be obtained in both the dilute, and the semi-dilute regime. In the perspective of an efficient upscaling of the highly individualized CNF

production, our findings suggest possibilities for improvements of the current process, while maintaining transparency of the final gels and aerogels. The dynamic overlap concentration describes well the transition from viscous to elastic rheological behavior of the CNF dispersions depending on the aspect ratio.

However, at very low concentrations, we observed deviations, where G' was dependent on the fibril length instead. We were able to exploit this deviation to experimentally determine the mesh size to be 81 nm at a concentration of 0.06 wt%. This mesh size is in fine agreement with the 88 nm predicted from scaling arguments. Our results suggest a different ability of CNFs to form stable network depending on the cellulose source, where the fibrils from the unbleached source have a better capability to entangle and hence, build stronger networks.

Supercritical CO_2 -drying of the hydrogels was accompanied by shrinkage at room conditions due to the hygroscopic properties of CNFs, which indicates a need for further functionalization in order to stabilize the fibrillar networks to improve the applicability of the materials. The optical properties are mainly determined by the fibrillization, where the properties are inherited by the preceding hydrogels. Differences between aerogels produced by CNF dispersions originating from bleached or unbleached source, as well as from variations in contour length, could not be observed by SEM and AFM.

Experimental Section

Synthesis of carboxylated cellulose nanofibrils.

The exact protocol for the carboxylated CNF was published in an earlier work about the fibril characterization.^[109] In short, CNFs were prepared from bleached and unbleached never-dried sulfite softwood-dissolving pulp with a degree of polymerization of around 770 (Domsjö, Sweden) by TEMPO-mediated oxidation.^[29] For both sources, carboxylated pulps with three different charge densities were prepared using different amount of NaClO (1.5 – 10 mmol/g cellulose) as primary oxidant. The oxidized cellulose pulp was dispersed in 100 mL Milli-Q water (0.5 g/L), ultra-sonicated (Hielscher UP200S, operated at 200 W, no interval, 20% amplitude, 7 mm probe, cooled with ice water) for 11 min, followed by centrifugation at 4000 rpm for 20 min to remove non-fibrillated cellulose aggregates. The charge density was determined by conductivity titration.

Preparation of hydrogels and aerogels.

Hydrogels were produced by directly mixing 150 μL of 1 M NaCl into 850 μL of the cellulose dispersion (0.072 wt%) in a mold ($d = 1.6$ cm). The mold was sealed with parafilm and left to

gel overnight. Alternatively, 940 μL of the dispersion (0.065 wt%) was mixed with 60 μL 0.1 M HCl.

An alternative way for hydrogel formation was by diffusion. A mold filled with 1 mL of the fibril dispersion (0.061 wt%) was dipped into a NaCl (150 mM) or an HCl (6 mM) solution. A dialysis membrane (Spectrum Laboratories Standard RC Tubing, 6–8 kD cut-off) and a Teflon membrane (Sigma-Aldrich, 1.0 μm x 47 mm), which prevented the gel from sticking to the cellulose-based dialysis membrane, were used to cover the mold and to allow the diffusion of the ions and protons into the dispersion.

Hydrogels were transferred into a customized metal mesh cage and placed in 100 mL of 50% EtOH at 5 $^{\circ}\text{C}$ for 24 h for solvent exchange. The second and third exchanges took place in 97% EtOH (100 mL), and in 99% EtOH (50 mL), respectively, followed by supercritical CO_2 -drying (Tousimis, Autosamdri 931).

Rheological analysis of dispersions and gels.

Fibril dispersions were analyzed with a Physica MCR 5501 rheometer (Anton Paar) equipped with a double gap geometry ($d = 2.67$ cm). A solvent trap prevented evaporation. The temperature was held constant at 20 $^{\circ}\text{C}$. The viscosity was measured with shear rates ($\dot{\gamma}$) from 1000 to 1 s^{-1} .

The gelation was characterized after addition of NaCl (150 mM) or HCl (6 mM) using a cone-plate geometry ($d = 2.5$ cm, angle 2.006 $^{\circ}$) at 20 $^{\circ}\text{C}$. Subsequently, the dispersion was oscillated in a time sweep experiment, keeping strain (γ) and angular frequency (ω) constant at 0.5% and 1 rad/s, respectively, until the dynamic modulus reached a constant value. A frequency sweep from 100 to 0.1 rad s^{-1} at constant strain ($\gamma = 0.5\%$), followed by a strain sweep from 0.1% to 100% at constant angular frequency ($\omega = 1$ rad s^{-1}) was performed.

Scanning electron microscopy.

Small pieces of the aerogels were mounted on SEM aluminum stubs with conductive carbon paste. After drying, the samples were cut with a razor blade and sputter-coated with 4 nm of platinum/palladium (CCU-10, Safematic). SE-inlens images were recorded at a working distance of 4–5 mm with a scanning electron microscope (Merlin FE-SEM, Zeiss), operated at an accelerating voltage of 1.5 kV.

Atomic force microscopy.

To image the single CNFs, freshly cleaved mica was modified with 20 μL of 0.05% (3-aminopropyl)triethoxysilane (APTES) for 60 s to obtain a positively charged mica surface. A droplet of around 2 mg/L CNF dispersion was deposited on the mica and allowed adsorbing

for 30 s before rinsing with Milli-Q water and drying with pressurized air. The AFM measurements (MultiMode VIII Scanning Probe Microscope, Bruker) were conducted in tapping mode under ambient conditions using commercial cantilevers (Bruker). The aerogels were deposited directly on the mica and scanned under ambient conditions.

Supporting Information

Supporting Information is available from the Wiley Online Library or from the author.

ACKNOWLEDGEMENTS

We thank Domsjö, Sweden for providing the paper pulp. M.A. and G.N. acknowledge funding from the Swiss National Science Foundation Ambizione Grant No. PZ00P2_168023/1. The authors acknowledge support of ScopeM/Swiss Federal Institute of Technology ETHZ.

Supplementary figures

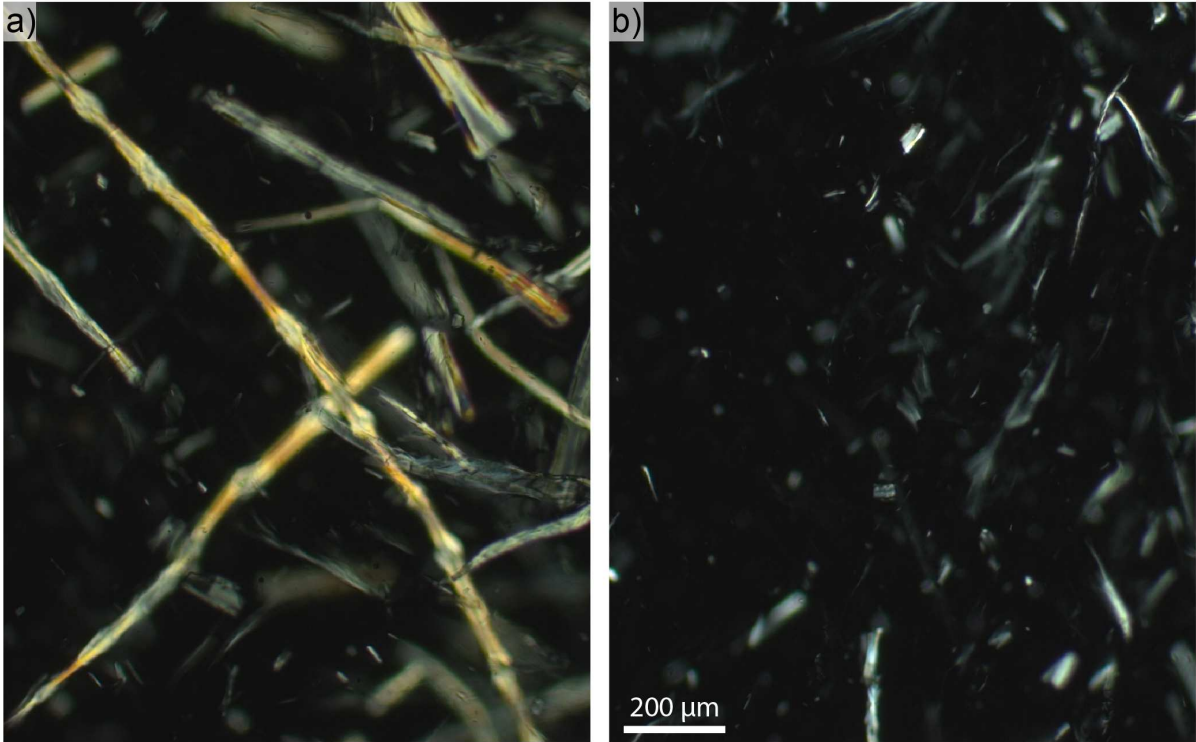


Figure S1. Polarized light micrographs of CNF dispersion (0.5 wt%) from unbleached pulp after 11 min sonication. a) 20 min centrifugation at 4000 rcf and b) after additional 90 min centrifugation at 12000 rcf.

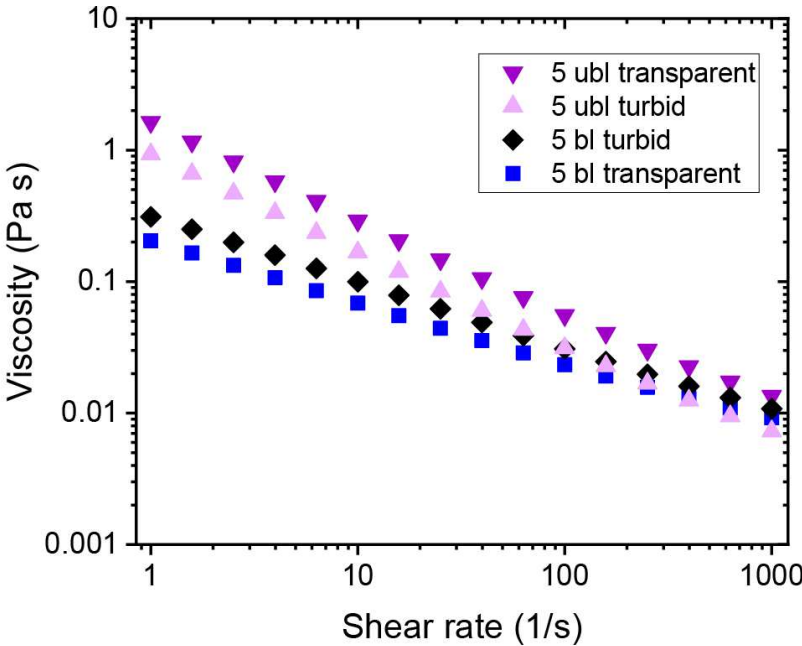


Figure S2. Rheological behavior of transparent and turbid CNF dispersions (0.40 wt%) using a double gap geometry.

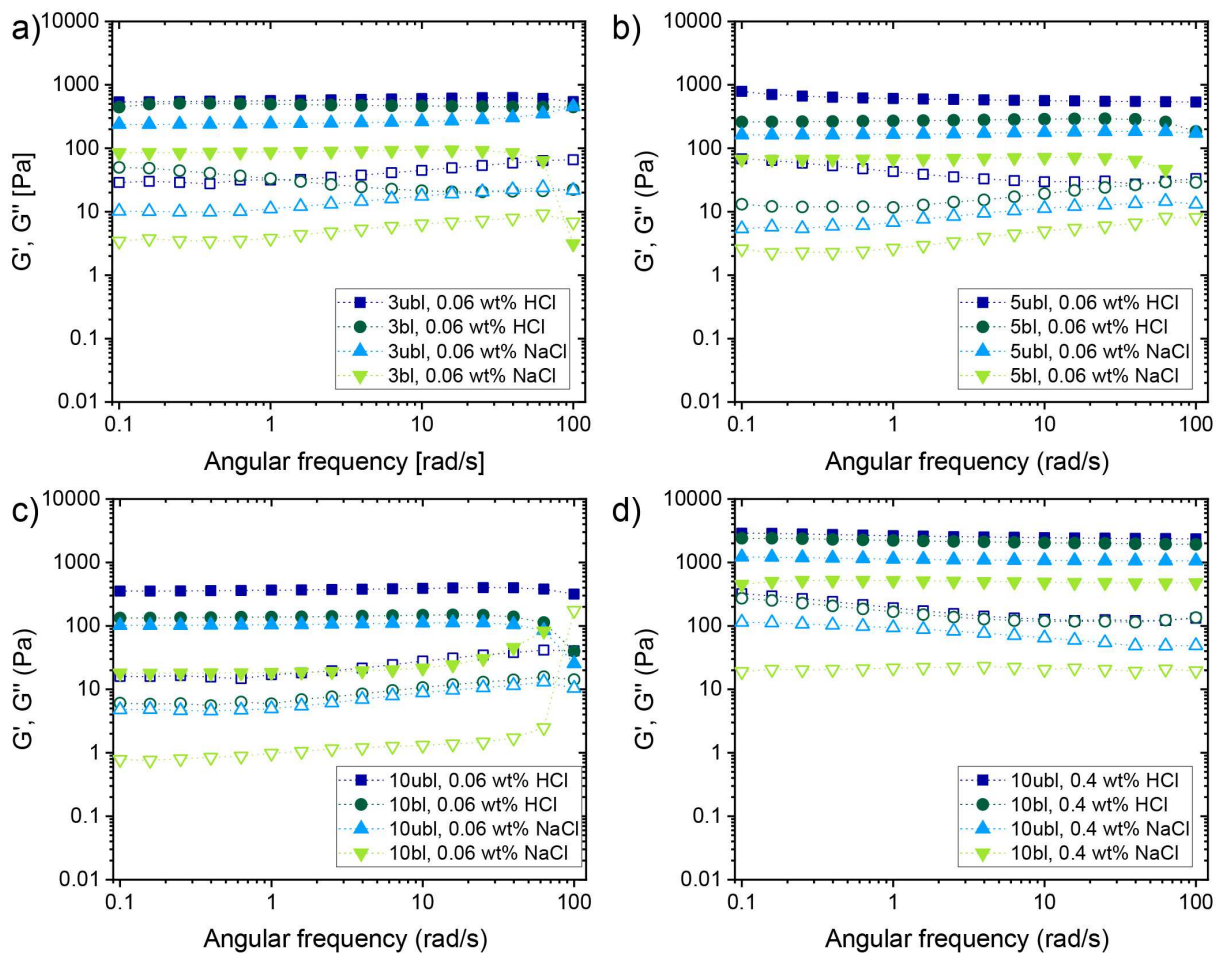


Figure S3. Elastic and viscous shear moduli across the measured angular frequency ω range of a) 3 mmol, b) 5 mmol and c) 10 mmol at 0.06 wt% CNF, and d) 10 mmol at 0.4 wt%.

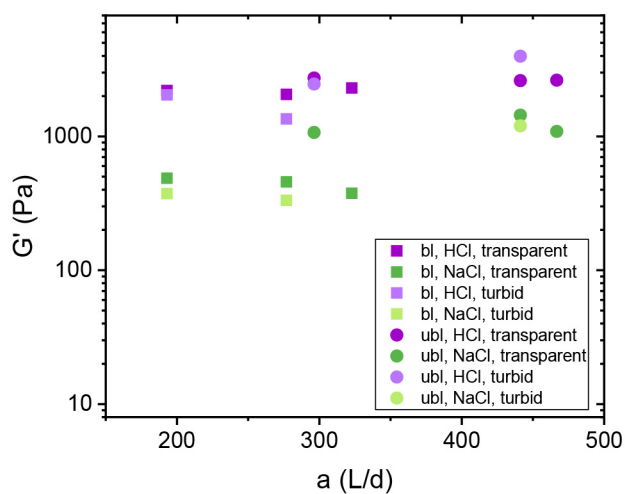


Figure S4. Comparison of elastic shear modulus G' depending on aspect ratio of transparent and turbid CNF dispersions.

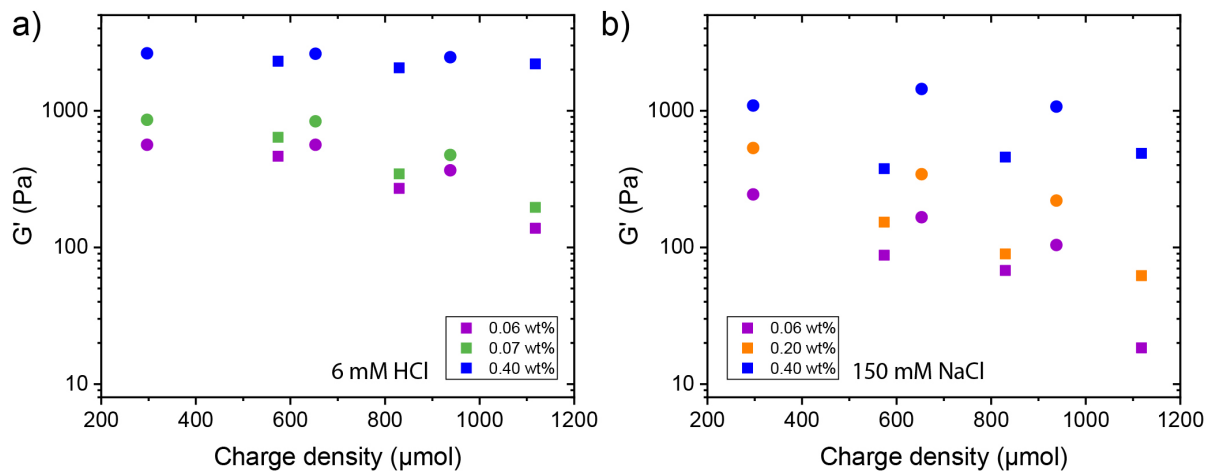


Figure S5. Dependency of the elastic shear modulus (G') on charge density of the gels at $\omega = 1$ rad/s, $\gamma = 0.5\%$ and 20°C for different concentrations after adding a) 6 mM HCl and b) 150 mM NaCl. The squares represent CNFs from bleached pulps, the circles unbleached, respectively.

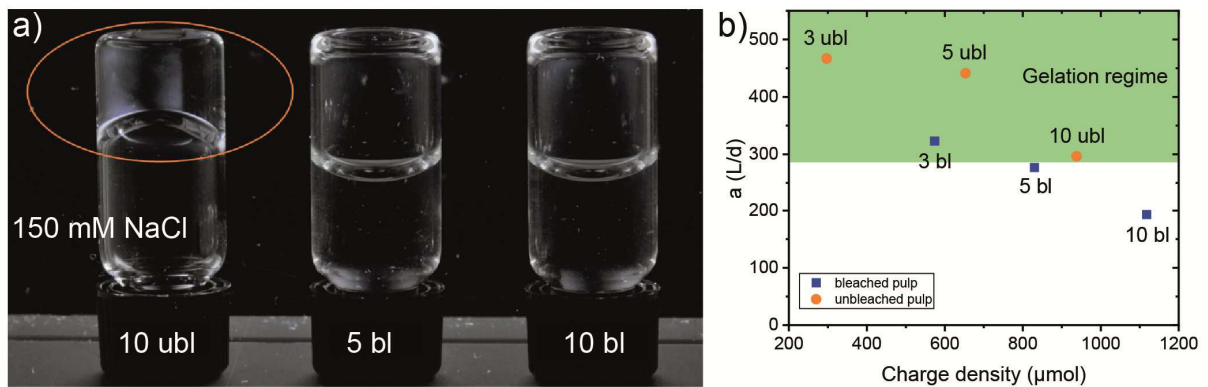


Figure S6. a) Inversion test and b) gelation dependency on aspect ratio as function of charge density of CNFs from bleached and unbleached pulp at 0.06 wt% due to addition of 150 mM NaCl.

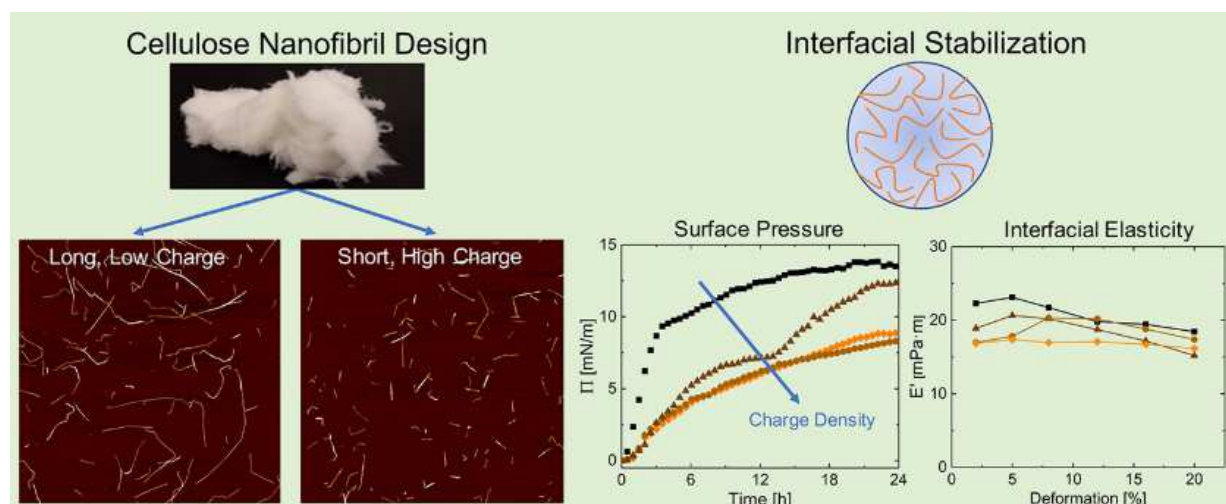
Designing cellulose nanofibrils for stabilization of fluid interfaces

Pascal Bertsch, Mario Arcari, Thomas Geue, Raffaele Mezzenga, Gustav Nyström, and Peter Fischer

Biomacromolecules 2019, 20, 4574–4580

<https://doi.org/10.1021/acs.biomac.9b01384>

Reprinted with permission from reference ^[153]. Copyright 2019 American Chemical Society.



Designing Cellulose Nanofibrils for Stabilization of Fluid

Interfaces

Pascal Bertsch,^{†,||} Mario Arcari,^{†,||} Thomas Geue,[‡] Raffaele Mezzenga,[†] Gustav Nyström,^{*,†,§} and Peter Fischer^{*,†}

[†]Institute of Food Nutrition and Health, ETH Zurich, 8092 Zurich, Switzerland.

[‡]Laboratory of Neutron Scattering and Imaging, Paul Scherrer Institut, 5232 Villigen PSI, Switzerland.

[§]Laboratory for Cellulose & Wood Materials, EMPA, 8600 Dübendorf, Switzerland.

ABSTRACT

Particles of biological origin are of increasing interest for the Pickering stabilization of biocompatible and environmentally friendly foams and emulsions. Cellulose nanofibrils (CNFs) are readily employed in that respect; however, the underlying mechanisms of interfacial stabilization remain widely unknown. For instance, it has not been resolved why CNFs are unable to stabilize foams while efficiently stabilizing emulsions. Here, we produce CNFs with varying contour lengths and charge densities to investigate their behavior at the air–water phase boundary. CNFs adsorbing at the air–water interface reduce surface tension and form interfacial layers with high viscoelasticity, which are attributed to the thermodynamic and kinetic stability of CNF-stabilized colloids, respectively. CNF adsorption is accelerated and higher surface pressures are attained at lower charge densities, indicating that CNF surface charges limit both adsorption and surface coverage. CNFs form monolayers with $\sim 40\%$ coverage and are primarily wetted by the aqueous phase indicating a contact angle $< 90^\circ$, as demonstrated by neutron reflectometry. The low contact angle at the air–water interface is energetically unfavorable for adsorbed CNFs, which is proposed as a potential explanation why CNFs show poor foaming capacity.

INTRODUCTION

Nanocelluloses, cellulose nanofibrils (CNFs) and nanocrystals (CNCs), are renewable nanoparticles that have attracted attention for the stabilization of foams and emulsions.^[39,82] Short, rigid CNCs and longer, partially flexible CNFs can be produced by hydrolysis, oxidation, or through enzymatic treatment from a wide range of cellulosic materials, yielding charged anisotropic nanoparticles.^[10,29] CNCs and CNFs allow the formation of stable Pickering emul-

sions due to high steric and electrostatic repulsion.^[81,154] Their irreversible adsorption facilitates the formation of high internal phase emulsions with an oil content up to 90%.^[83] Ambiguously, nanocelluloses show poor foaming capacity and require hydrophobic surface modifications or adsorption of a cationic surfactant to stabilize foams.^[85,155,156] The stabilization of fluid air–water (A/W) or oil–water (O/W) interfaces using solid particles is known as Pickering stabilization. It comprises the adsorption of particles that are partially wettable by both subphases and prevent their energetic unfavorable contact.^[157] Nanoparticle adsorption is limited by (i) particle diffusion to the interface and (ii) a kinetic adsorption barrier.^[158,159] Current efforts aim at expanding these principles beyond spherical model particles, to account also for charged anisotropic particles such as nanocelluloses. Surface charges result in a higher kinetic adsorption barrier due to electrostatic repulsion within particles in the bulk and adsorbed particles.^[159] Even in absence of other particles, ionic species accumulated at the liquid interface or image charges may impede adsorption.^[160] Surface charges further induce repulsive capillary forces within adsorbed nanoparticles, which limit their surface coverage.^[161] It was previously demonstrated that CNC adsorption lasts several hours in diffusion-limited experiments, but adsorption and surface coverage may be promoted by salt-induced charge screening.^[40,86] It is also known from emulsions that nanocelluloses do not adsorb beyond a critical charge density, and adsorption must then be triggered by salt addition.^[162,163] Adsorbed nanocellulose layers may stabilize fluid interfaces by a decrease in interface tension,^[40,86] electrostatic and steric repulsion,^[154,156] and formation of viscoelastic interfacial layers.^[156,164] We recently reported on the decrease in interface tension, interfacial layer strength, and structure of CNC layers at the A/W and O/W interfaces.^[40,86,164] Such reports are still missing for CNFs, strongly impeding current understanding of CNF interfacial stabilization. TEMPO-mediated oxidation is widely employed for CNF production as it allows the extraction of single CNFs with high crystallinity and selective oxidation of the C6 carbon.^[29,42] Furthermore, the properties of obtained CNFs can be tuned by the physical and chemical process parameters. Ultrasonication induces defects along the fibril contour (so-called kinks) where the fibrils can break, resulting in fibril shortening.^[46,47,53] Increasing the concentration of the oxidation agent yields shorter fibrils with higher charge density, whereas the latter further induces a decrease in twist periodicity.^[29,109] Here, we produce CNFs with varying charge densities and contour lengths to investigate their adsorption kinetics, dilatational rheology, and interfacial layer structure at the A/W interface.

MATERIALS AND METHODS

CNF Preparation and Characterization. Carboxylated CNFs were produced following the TEMPO-mediated oxidation protocol by Saito et al.^[29] In short, CNFs were prepared from bleached and unbleached never-dried sulfite softwood-dissolving pulp (Domsjö, Sweden). From each source, four pulp samples were TEMPOoxidized at pH 10 with different amounts of NaClO (1.5–10 mmol/g cellulose) as the primary oxidant to obtain different charge densities. The carboxylated cellulose pulp was dispersed in 100 mL of Milli-Q water (0.1 wt %), ultrasonicated (Hielscher UP200S, operated at 40 W, no interval, 7 mm probe, cooled with ice water) for 25 min, and centrifuged at 4000 rcf for 20 min to remove nonfibrillated cellulose aggregates. The impact of the ultrasonication is reduced over time, and fibril length converges to a minimum after 25 min.^[47] The concentration was determined by measuring the dry weight and adjusted to 0.1 wt % by dilution or solvent evaporation. The charge density of the carboxylated pulp was determined by conductivity titration following the SCAN-CM 65:02 protocol,^[109] and CNF dimensions were analyzed from atomic force microscopy images using FiberApp.^[128]

Atomic Force Microscopy (AFM) of Single CNFs.

Freshly cleaved mica was modified with 20 μL of 0.05 vol % (3-aminopropyl)triethoxysilane (APTES) for 60 s to obtain a positively charged mica surface. A droplet with a concentration of 2 mg/L CNF was deposited on the mica for 30 s before rinsing with Milli-Q water and drying with pressurized air. The AFM measurements (MultiMode VIII scanning probe microscope, Bruker) were conducted in tapping mode under ambient conditions using commercial cantilevers (Bruker) to obtain images with a resolution of 2.0 nm/pixel.

CNF Adsorption Experiments.

CNF adsorption was determined by the Wilhelmy plate technique. A Wilhelmy balance (KSV Nima) was equipped with a paper plate (21 mm in perimeter) and immersed in 65 mL of CNF dispersion in a homemade Teflon trough ($15 \times 7.8 \times 0.5 \text{ cm}^3$). CNF adsorption was recorded by the surface pressure Π , which corresponds to the decrease in surface tension γ relative to $t = 0$, $\Pi = \gamma_0 - \gamma$. A 2 cm Teflon barrier was mounted on each side, resulting in a surface area A_0 of 86 cm^2 . The barriers were fully closed prior to each measurement to detect potential contaminations. The room temperature was controlled to 22 °C.

Interfacial Dilatational Rheology.

After 25 h of CNF adsorption, interfacial dilatational experiments were performed with the Wilhelmy plate setup introduced above by sinusoidal oscillations of the two Teflon barriers

parallel to the plate. Stepwise increasing area oscillations were performed at 10 mHz oscillation frequency. The interfacial dilatational storage E' and loss E'' moduli were calculated from [109] normalized oscillation cycles. E' and E'' are defined by

$$E' = \Delta\Pi \frac{A_0}{\Delta A} \cos \delta \quad (1)$$

$$E'' = \Delta\Pi \frac{A_0}{\Delta A} \sin \delta \quad (2)$$

where δ is the phase lag of the induced area deformation $A_0/\Delta A$ and resulting changes in surface pressure $\Delta\Pi$.

Neutron Reflectometry.

Interfacial neutron reflectivity experiments were performed at SINQ, the Swiss Spallation Neutron Source at Paul Scherrer Institute (Villigen PSI, Switzerland) with the AMOR time-of-flight reflectometer.^[165] The same Langmuir trough and paper plates as introduced above were used. CNFs were produced in D_2O (99.9 atom % D, ARMAR Chemicals), as elaborated above. Experiments were performed with 65 mL of 0.1 wt % CNF at 25 °C once a stable surface pressure (~25 h) was attained. Reflectivity at pure D_2O was measured as reference. Neutron reflection was recorded at three angles of incidence θ (0.5, 1.3, and 2.8°) and varying neutron wavelengths λ (3.5 to 12 Å), thereby covering a q range of 0.01–0.187 Å⁻¹ within 10.5 h at full neutron flux. The first angle of incidence ($\theta = 0.5^\circ$) was repeated at the end of the experiment to verify that the layers did not undergo significant changes. The measured neutron reflectivity was fitted by the Parratt algorithm^[166] to assess the interfacial structure of the CNF layers. The fits had a $\chi^2 < 2.6 \times 10^{-2}$.

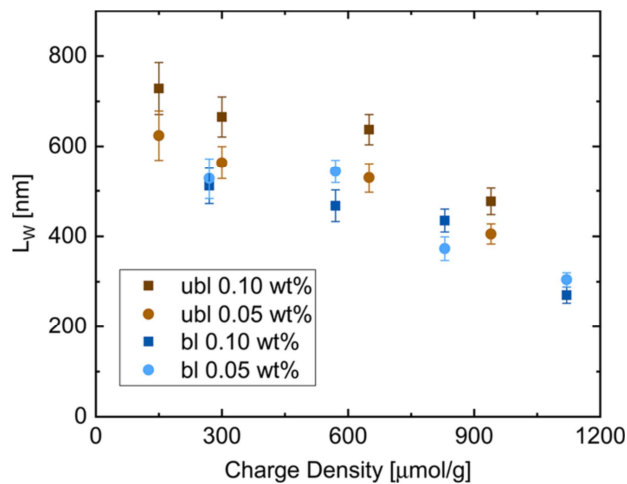


Figure 1. Dependence of length weighted fibril length L_w on charge density of CNFs obtained from unbleached (ubl) and bleached (bl) soft wood pulp after 25 min sonication at 0.1 wt % (present study) and 0.05 wt % (from Arcari et al.^[109]), determined from AFM images using FiberApp.^[128]

RESULTS AND DISCUSSION

Preparation of CNFs with Varying Lengths and Charge Densities.

A set of CNFs with varying contour lengths and surface charge densities were produced to investigate their effect on CNF adsorption behavior. Two different wood pulps were used as starting materials, one before and the other after industrial bleaching. The fibril length and surface charge density were altered by the amount of primary oxidation agent, in this case NaClO, that is used for the TEMPO-mediated oxidation of the cellulose pulp.^[29,109] The ultrasonication treatment was constant at 25 min. In total, we produced eight different CNFs, four from each bleached and unbleached pulp, with surface charge densities from 150 to 1120 $\mu\text{mol/g}$ cellulose. The mean length weighted contour length L_w of the CNFs is shown in Figure 1. Shorter CNFs were obtained at increasing charge density as the increased electrostatic repulsion facilitates the individualization of the fibrils at constant mechanical treatment.^[43] The amount of kinks where the fibrils can break decreases linearly with charge density and does not depend on the cellulose source.^[109] It was previously reported that the carboxylation efficiency is lower for the unbleached pulp,^[109] yielding longer CNFs with lower charge density at the same NaClO concentration. A higher initial cellulose pulp concentration was used (0.1 wt %) in contrast to our previous study (0.05 wt %),^[109] which resulted in slightly longer CNFs obtained from unbleached pulp. Figure 2 shows AFM height images of the CNFs produced from unbleached (left) and bleached (right) pulp at the lowest (top) and highest (bottom) charge densities, visualizing that shorter CNFs are obtained from bleached soft wood pulp and at higher charge density. The detailed information on CNF dimensions and charge densities is compiled in Table 1.

Table 1. Characterization of CNFs Produced from Unbleached and Bleached Soft Wood Pulp with Varying Amounts of Oxidation Agent NaClO Showing Charge Density (CD, from Arcari et al.^[109]), Average Contour Length (L_a), Length Weighted Contour Length (L_w), and Diameter (D)^a

parameter	unbleached pulp				bleached pulp			
	1.5	3	5	10	1.5	3	5	10
NaClO (mmol/g)	1.5	3	5	10	1.5	3	5	10
CD ($\mu\text{mol/g}$)	150 \pm 10	300 \pm 40	650 \pm 30	910 \pm 10	270 \pm 10	570 \pm 30	830 \pm 40	1120 \pm 20
L_a (nm)	430 (40)	410 (30)	410 (30)	290 (20)	310 (30)	290 (30)	270 (20)	160 (10)
L_w (nm)	730 (60)	670 (40)	640 (30)	480 (30)	510 (40)	470 (30)	430 (30)	270 (20)
D (nm)	2.18 (0.07)	1.98 (0.04)	1.56 (0.03)	1.77 (0.04)	2.36 (0.10)	2.11 (0.07)	1.93 (0.04)	1.78 (0.05)

^a CNF dimensions were obtained from AFM height images. The values in brackets correspond to the 95% confidence interval.

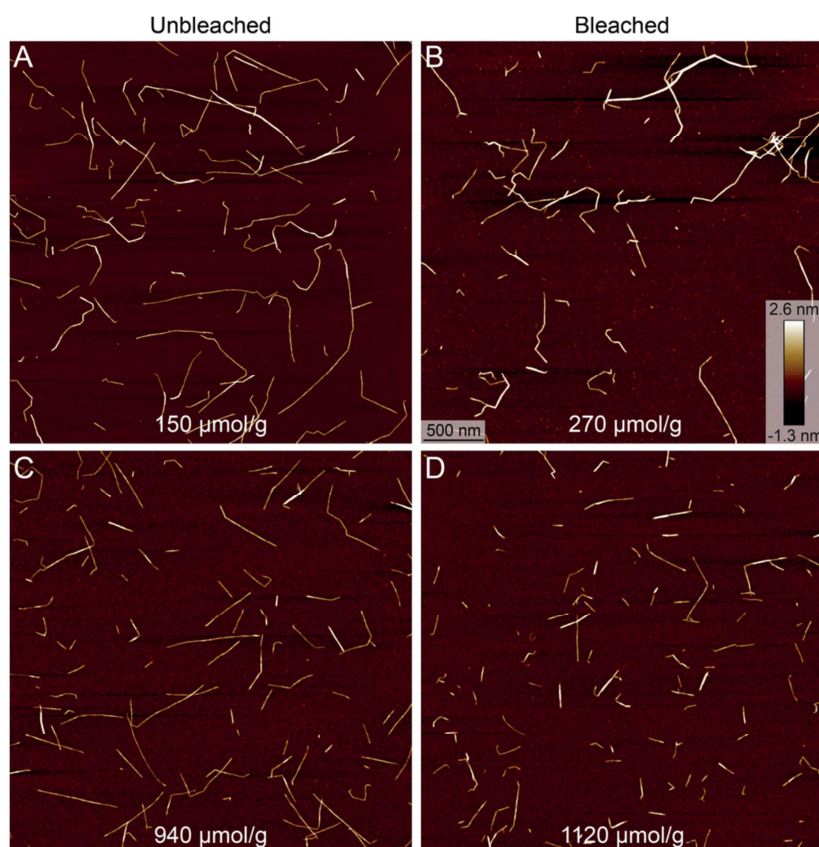


Figure 2. AFM height images of individualized CNFs from unbleached and bleached soft wood pulp with different charge densities after 25 min sonication.

CNF Adsorption and Interfacial Rheology at the A/W Interface.

The adsorption of 0.1 wt % CNFs extracted from unbleached and bleached soft wood pulp at the A/W interface is depicted in Figure 3 A,B, respectively. CNF adsorption is characterized by an initial lag phase without measurable changes in surface pressure Π followed by adsorption within ~ 24 h. The lag phase was reduced and higher Π was attained for CNFs with decreasing charge density. The faster adsorption can be attributed to a lower electrostatic repulsion of adsorbed particles and particles in the bulk, which decreases the kinetic adsorption barrier.^[159] The higher Π denotes a higher surface coverage, which may again derive from the lower kinetic adsorption barrier or lower electrostatic repulsion within adsorbed CNFs. Accelerated adsorption and higher Π were also observed for CNCs upon salt-induced charge screening.^[40,86] This is in good agreement with findings in emulsions, where emulsification is enhanced at lower charge density or upon charge screening but ceases above a critical charge density.^[162,163] Hence, a sufficiently low surface charge or additional charge screening is crucial to exploit CNF interfacial stabilization.

As shown in Figures 1 and 2, longer CNFs are obtained at lower charge densities. It could be argued that the surface coverage of longer CNFs is increasingly limited by their excluded area

A_{ex} , which scales $A_{\text{ex}} \approx L^2$.^[151] However, the present results do not show an effect of fibril length, and the observed behavior can mostly be explained by the varying CNF charge densities. This is interesting considering that the A_{ex} of a 600 nm long fibril is $\sim 210 \text{ nm}^2$ while its Debye length is only $\sim 13 \text{ nm}$.^[46,151] It is possible that attractive capillary forces that arise due to the quadrupolar interface distortions of anisotropic particles dominate over the excluded area.^[167] CNFs extracted from unbleached pulp adsorbed faster and attained higher Π compared to those from bleached pulp. This may derive from remains of lignin in the unbleached pulp, which can also adsorb at fluid interfaces and is more hydrophobic than cellulose.^[82,127] It was reported before that nanocrystals obtained from holocellulose that still contains lignin and hemicellulose adsorb faster than CNCs from purified pulp.^[168]

Figure 3 C,D shows the interfacial dilatational moduli E' and E'' of adsorbed CNF layers from unbleached and bleached pulp, respectively. Measurements were performed after 25 h adsorption on quasi-static CNF layers. All CNFs formed viscoelastic interfacial layers with dominating elastic contributions ($E' > E''$). The layers showed a primarily linear response with E' and E'' being independent of deformation amplitude. Interestingly, CNFs formed viscoelastic interfacial layers independent of charge density, with a slight trend to higher E' at lower charge density. This is in strong contrast to adsorbed CNCs that form viscous interfacial layers, and elasticity must be induced by charge screening.^[164] The increased fibril length and occurrence of kinks may favor fibril entanglement and formation of a viscoelastic interfacial network. Alternatively, it could derive from a higher CNF surface coverage compared to CNCs, as discussed below. Our findings are in good agreement with previous reports on the viscoelasticity of surfactant-induced nanocellulose adsorption layers.^[156] A complex modulus of $\sim 25 \text{ mPa}\cdot\text{m}$ was reported for CNFs in contrast to $5 \text{ mPa}\cdot\text{m}$ for CNCs. The detailed response of CNF layers at the highest deformation tested ($\Delta A/A_0 = 20\%$) is further visualized by the induced changes in Π as a function of surface area in Lissajous plots,^[169] as shown in Figure 4. The Lissajous plots had a constant slope when the interfacial area was higher than A_0 (negative $\Delta A/A_0$), denoting a linear pressure–area response. The slope decreased at decreasing interfacial area (positive $\Delta A/A_0$), indicating nonlinear strain softening in compression, followed by strain hardening in expansion. No significant differences were observed for high and low CNF charge densities. Hence, CNFs form viscoelastic interfacial layers with a broad linear viscoelastic regime and upcoming nonlinear behavior at high deformations. Their interfacial behavior is mostly independent of CNF charge density, in contrast to shorter CNCs that only form viscoelastic layers upon charge screening^[164] or hydrophobic surface modifications.^[170,171]

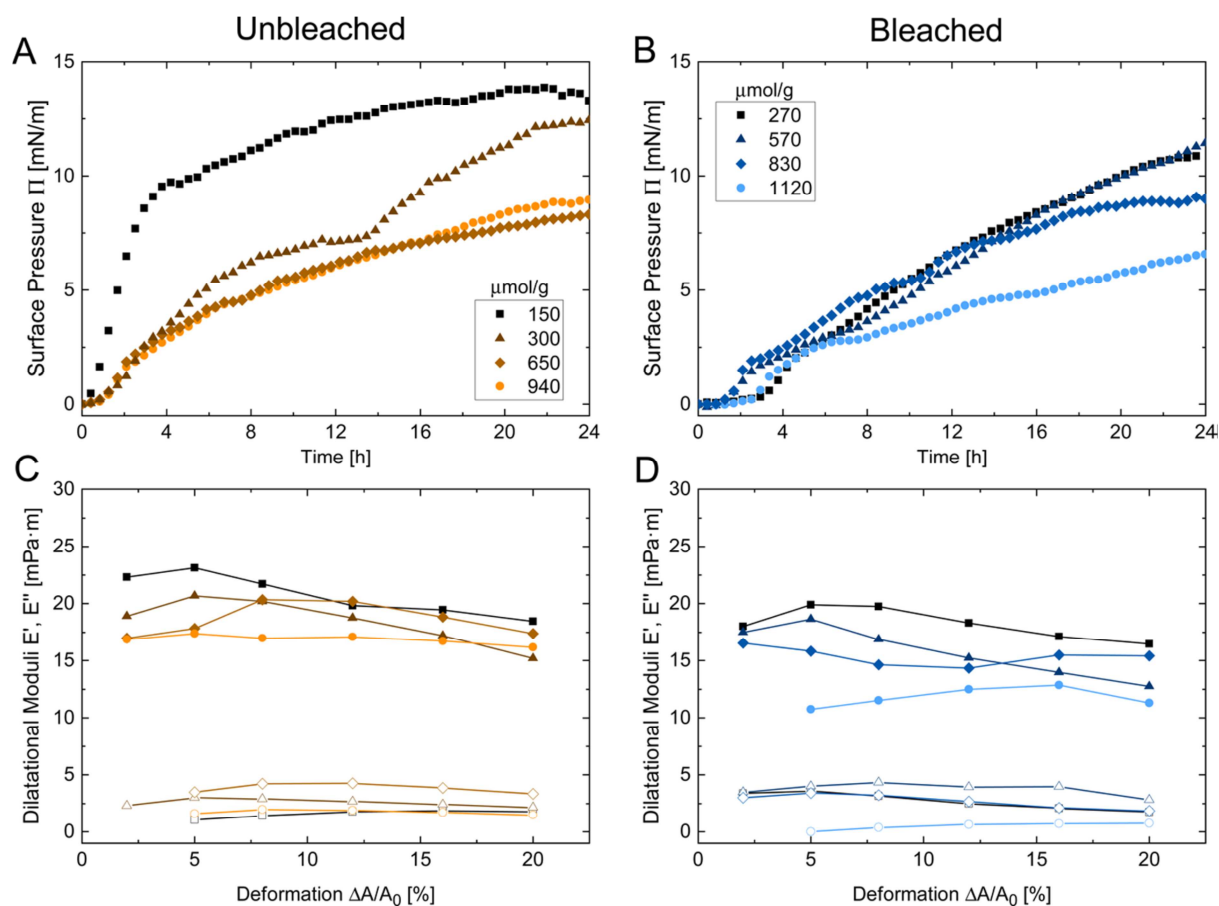


Figure 3. Adsorption kinetics of 0.1 wt % CNFs with varying charge densities extracted from (A) unbleached and (B) bleached soft wood pulp. (C,D) Interfacial dilatational amplitude sweeps of the adsorbed CNF layers showing the storage E' (full) and loss E'' (empty) moduli as a function of area deformation at an oscillation frequency of 10 mHz (determined by the Wilhelmy plate technique at 22 °C).

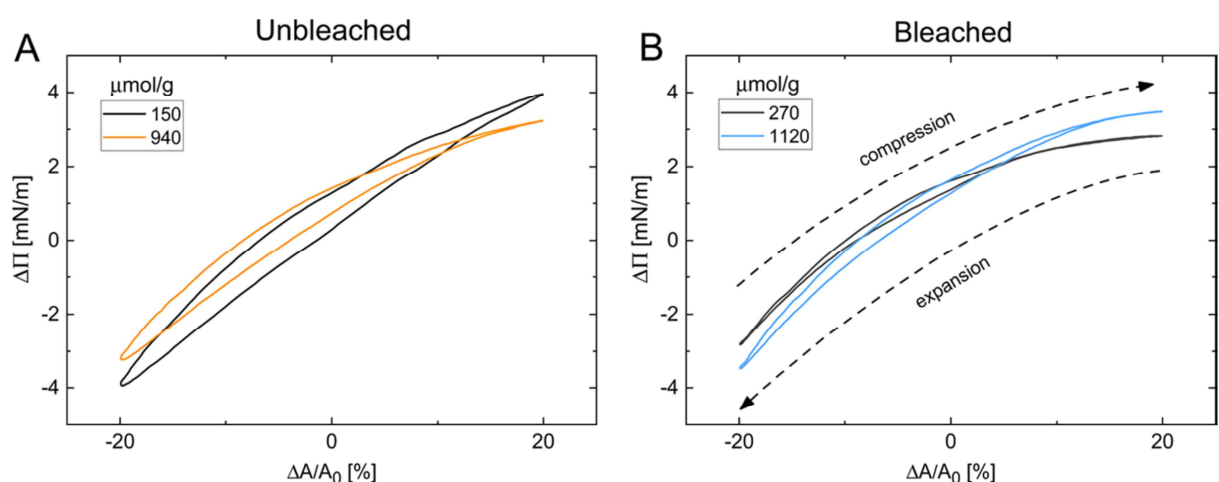


Figure 4. Pressure-area response (Lissajous plots) of adsorbed CNF layers at 20% compression expansion cycles for (A) unbleached and (B) bleached pulp for the highest and lowest charge densities investigated.

Thus, CNFs stabilize fluid interfaces by a decrease in interface tension and formation of comparably strong interfacial layers. A reduction in interface tension γ increases the thermodynamic stability of foams and emulsions, as the Gibbs free energy ΔG of multiphase systems is directly related to its surface area A by $\Delta G = \gamma\Delta A$. The interfacial elasticity on the other hand provides kinetic stability. In fact, the high interfacial moduli of adsorbed CNF layers may be the reason for the exceptional steric stability generally observed in CNF stabilized foams and emulsions.^[85,154] A high interfacial elasticity is associated with a decrease in both coalescence^[172] and Ostwald ripening.^[173] The electrostatic repulsion induced by adsorbed CNFs further promotes kinetic stability. Considering electrostatic repulsion, there seems to be a trade-off; highly charged CNFs provide higher electrostatic repulsion; however, they form less dense interfacial layers associated with a lower surface pressure and viscoelasticity. Another stabilization route not taken into account by our experiments is the thickening of the bulk phase by CNFs and the formation of an interconnected network that entraps air bubbles or oil droplets.^[85,174] Despite the reduction in surface tension and interfacial elasticity at the A/W interface, CNFs generally show poor foaming capacity on their own. They need to be modified or employed in combination with a surfactant to form stable foams,^[85,155,156] in strong contrast to emulsions where no such problems occur. A possible explanation is an unfavorable contact angle of CNFs at the A/W interface, as addressed in detail in the following section.

Interfacial Layer Structure of Adsorbed CNFs.

The structure of adsorbed CNF layers at the A/W interface was investigated by neutron reflectometry. Figure 5A depicts the neutron reflectivity intensity of three CNFs from bleached and unbleached pulp with particularly high and low charge densities relative to pure D₂O. Due to small differences within the tested CNFs, the reflectivity data is given as line and further visualized as reflectivity relative to the reference in Figure 5B. To obtain information on the structure of CNF layers, the reflectivity data was fitted using the Parratt algorithm (Figure S1). The interfacial layers were best described by a model accounting for a monolayer of CNFs and the underlying aqueous sub-phase. The formation of monolayers is widely accepted for nanocelluloses based on findings from small angle neutron scattering^[175] and previous reflectivity experiments.^[40,176] The layer thickness and roughness obtained from the fits are compiled in Table 2. All three CNFs formed adsorption layers with a thickness of ~ 8 Å, close to the lower spatial resolution limit of the employed setup, and variations within different CNFs were within the resolution limit. As shown in Table 1, the height of individual CNFs is 18–22 Å. As the neutron reflectivity is averaged over a certain interfacial area, the layer thickness below the height of individual CNFs suggests that CNFs do not cover the entire interface. The monolayers were best de-

scribed with a scattering length density (sld) of $4.3 \cdot 10^{-6} \text{ \AA}^{-2}$, an intermediary of pure cellulose of $1.6 \cdot 10^{-6} \text{ \AA}^{-2}$, and pure D_2O of $5.9 \cdot 10^{-6} \text{ \AA}^{-2}$, further supporting that the interface is not fully covered with CNFs. Comparison of the layer thickness (8 \AA) and average CNF height (18–22 \AA) allows an approximation of the CNF surface coverage to $\sim 40\%$. The employed monolayer–subphase model further facilitated to probe the localization of CNFs along the z axis, that is, the protrusion into either subphase, as visualized by the sld profile in the z-direction in Figure 5C. The surface roughness of CNF layers toward the air phase did not exceed the roughness induced by capillary waves at the A/W interface ($\sim 4 \text{ \AA}$).^[177] Hence, the CNFs did not significantly protrude into the air phase and remain mostly in the aqueous phase. This provides qualitative information that CNFs adsorb at a contact angle $< 90^\circ$. van den Berg et al.^[178] presented a model that allows the quantitative determination of contact angles from neutron reflectivity data, which however requires variation of several parameters and could not be employed for the present data. Nevertheless, a contact angle $< 90^\circ$ at the A/W interface is in agreement with previous reports.^[40,86]

Determining the orientation and distribution of CNFs in the interfacial x-y-plane was not possible as the scattering signal was insufficient to resolve off-specular data. However, the thin layers and limited expansion in the z direction suggest that CNFs are oriented flat in the x-y-plane. Orientation in the interfacial plane is energetically favorable for anisotropic particles^[179] and was also found for CNCs.^[40,176] We assume that the CNFs do not aggregate and remain as evenly distributed individual particles due to electrostatic repulsion, as previously reported for CNCs even at high ionic strength.^[40,164] A comparable surface coverage of 60% was reported for CNFs in O/W emulsions (850 nm length, 12 nm height, and 0.012 e/nm^2 charge density).^[154] Thus, there seems to be a reasonable agreement of CNF coverage at planar A/W interfaces and curved O/W droplets. The higher coverage in O/W emulsions can probably be attributed to shear forces during emulsification. Another explanation was provided by Lewandowski et al.,^[180] who demonstrated that anisotropic particles preferentially orient side-by-side at curved interfaces, which could facilitate the packing of anisotropic nanoparticles. We recently reported a surface coverage of 20% for CNCs using the same neutron reflectivity setup.^[40] The higher surface coverage found for CNFs compared to CNCs at planar A/W interfaces may explain the higher viscoelasticity observed for CNFs (Figure 3,CD). A higher surface coverage for longer CNFs compared to CNCs is again in conflict with excluded area argumentations, as discussed above. Based on the surface pressure and interfacial coverage, the adsorption energy ΔE of a single CNF adsorbing at the A/W interface can be approximated by an area displacement approach^[181]

$$\Delta E = -\frac{\Pi A}{\eta} \quad (3)$$

Assuming the surface coverage $\eta = 40\%$, an average CNF area A of 1200 nm^2 (Table 1), and a surface pressure Π of 10 mN/m (Figure 3), this results in $\Delta E \approx -7 \cdot 10^3 \text{ kBT}$. This value is in very good agreement with the ΔE reported for CNCs^[40] as the higher coverage and larger area of CNFs repeal each other. The limited protrusion of CNFs into the air phase indicates that CNFs are preferentially wetted by the aqueous phase and adsorb at a contact angle $< 90^\circ$. Although a deviation from 90° is energetically unfavorable for Pickering particles, similar findings were also reported for CNCs at the A/W interface^[40] and in O/W emulsions.^[175] It was recently demonstrated that the contact angle shifted closer to 90° at O/W compared to A/W interfaces due to enhanced particle wetting.^[86] We assume the unfavorable contact angle at the A/W interface is the reason why nanocelluloses are not able to stabilize foams on their own, whereas no such problems are known from emulsions. It was previously observed that CNCs with a similar ΔE are not stably adsorbed at A/W interfaces and desorb upon compression.^[40] Adsorbed nanocelluloses are destabilized by line tension induced by their shape anisotropy^[182] and electrostatic repulsion.^[161] This argumentation is in line with reports on CNF stabilized foams, which employ surface modifications or adsorption of surfactants, rendering CNFs more hydrophobic and thereby achieving an energetically more favorable contact angle.

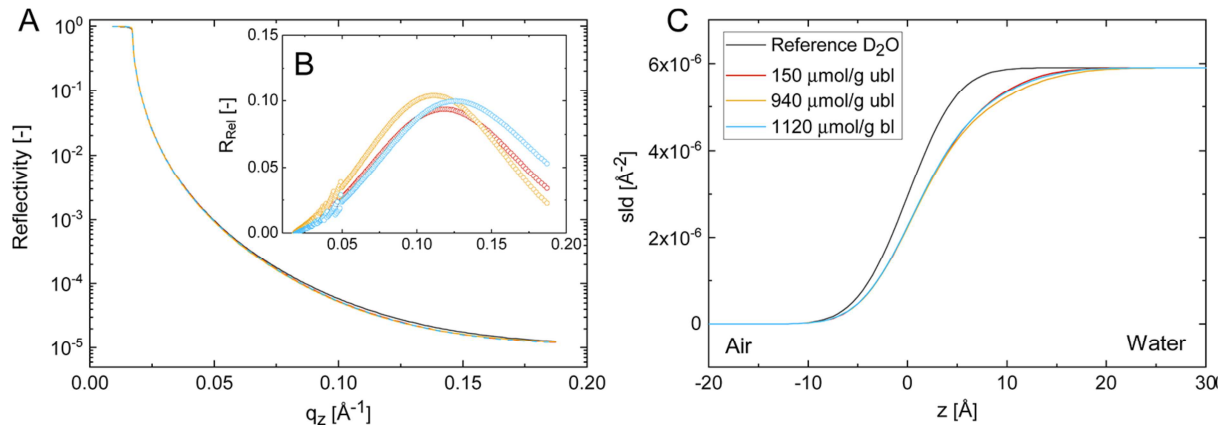


Figure 5. (A) Neutron reflectivity of pure D₂O and interfacial layers of CNFs with varying charge densities from unbleached (ubl) and bleached (bl) pulp at the air/D₂O interface. (B) CNF layer reflectivity relative to pure D₂O. (C) Fitted scattering length densities as a function of layer depth z .

Table 2. Thickness h and Roughness σ of CNF Interfacial Layers at the Air/D2O Interface Obtained from Neutron Reflectivity Data Fitted with the Parratt Algorithm Using a Monolayer–Subphase Model ($\chi^2 < 2.6 \times 10^{-2}$).

interfacial layer	150 mol ubl		940 mol ubl		1120 mol bl	
	h (Å)	σ (Å)	h (Å)	σ (Å)	h (Å)	σ (Å)
CNF layer	7.7	4.0	8.2	4.0	7.8	4.0
subphase		4.8		5.8		5.2

CONCLUSIONS

We investigated the mechanisms behind the interfacial stabilization by cellulose nanofibrils (CNFs) with varying charge densities and contour lengths. In particular, we aimed at the prevailing ambiguity that CNFs efficiently stabilize emulsions, while they need to be modified or combined with a surfactant to stabilize foams. CNFs were found to adsorb at the air–water interface within 24 h in diffusion-limited experiments, associated with a decrease in surface tension by ~ 10 mN/m. CNF adsorption and surface tension reduction were enhanced at decreasing charge density. Thus, CNFs behave as nonamphiphilic nanoparticles, with surface charges limiting both their adsorption and surface coverage. Area compression–expansion cycles revealed that CNFs form interfacial layers with high viscoelasticity independent of their charge density. The decrease in surface tension and high interfacial elasticity were attributed to thermodynamic and kinetic stability, respectively, of CNF stabilized colloids. Neutron reflectivity revealed that CNFs form loose monolayers at the air–water interface with an approximate surface coverage of 40%. The combined information on surface pressure and coverage allowed an approximation of CNF adsorption energy to $\sim -7 \cdot 10^3$ k_BT. CNFs were preferentially wetted by the aqueous phase, resulting in an unfavorable contact angle $< 90^\circ$. We argue that the low contact angle is the reason for the poor foaming capacity of CNFs without additional modification or presence of a surfactant.

AUTHOR INFORMATION

Corresponding Authors

*E-mail: Gustav.Nystroem@empa.ch (G.N.).

*E-mail: peter.fischer@hest.ethz.ch. Phone: +41 44 632 85 36 (P.F.).

Author Contributions

|| Pascal Bertsch and Mario Arcari contributed equally to this manuscript.

Notes

The authors declare no competing financial interest.

ACKNOWLEDGMENTS

Neutron reflectivity experiments were performed at the Swiss Spallation Neutron Source SINQ, Paul Scherrer Institute, Villigen PSI, Switzerland. This project was funded by the Swiss National Science Foundation, Project No. 200021-175994 and Ambizione Grant No. PZ00P2_168023/1.

Chapter 5

Conductive and insulated gold hybrid core-shell structures

Mario Arcari, Lukas E. Roder, Stephan Handschin, Jozef Adamcik, Raffaele Mezzenga and Gustav Nyström

Manuscript in preparation

Conductive and insulated gold hybrid core-shell structures

Mario Arcari¹, Lukas E. Roder¹, Stephan Handschin¹, Jozef Adamcik¹, Raffaele Mezzenga^{1,2*},
and Gustav Nyström^{1,3*}

1. ETH Zurich, Department of Health Sciences and Technology, Schmelzbergstrasse 9, 8092 Zurich, Switzerland.

2. ETH Zurich, Department of Materials, Wolfgang-Pauli-Strasse 10, 8093 Zurich, Switzerland.

3. EMPA, Laboratory for Cellulose & Wood Materials, Überlandstrasse 129, 8600 Dübendorf, Switzerland.

*Correspondence to: raffaele.mezzenga@hest.ethz.ch, gustav.nystroem@empa.ch

ABSTRACT

Sustainable nanomaterials have a great potential to provide solutions for new materials and technologies without compromising potential resource limitations. In this paper, we used anionic cellulose nanofibrils (CNFs) and cationic amyloid fibrils to study the mechanism of interfacial complexation of the two polyelectrolytic polymers to form composite materials. Knowledge from the phase behavior of the two components as a function of concentration and pH was used to develop a composite complex filaments as well as a proof-of-concept for printable core-shell structures composed of a conductive amyloid stabilized gold-crystal core and an insulating outer shell out of CNFs. Optimizing for the conductivity of the core, we found a conductivity threshold at > 70 wt% of gold, which is 20 wt% lower than so far reported. Targeted printing of these wires would allow for printing of multi-layer electrical circuits or even direct printing on casings without the need of additional insulation to save space for miniature applications.

INTRODUCTION

Biosynthesized fibers and filaments from sources such as wool^[183] and silk^[184] have been used since the beginning of human civilization and are still popular to this day. Increasing demand during the industrial revolution led, however, to the development of synthetic polymerized filaments, *e.g.* nylon. The monomers of nylon-6 are crosslinked by amine bonds and melting the thermoplastic polymer allows its processing into filaments.

In addition to biosynthesis and melt processing, electrostatic complexation is a complemen-

tary method to form materials from polymers. Other than hydrophobic and chemical interactions, electrostatic interactions are reversible, making them interesting for self-healing applications. Electrostatic interactions can also take place in aqueous surroundings devoid the use of harsh chemicals. This allows for bio-compatible applications such as wound healing, where treatment needs to be performed in wet conditions.^[88] The layer-by-layer technique is another prominent representative for electrostatic interactions.^[89]

Interfacial polyelectrolyte complexation (IPC) uses the same mechanism but instead of the layering, filaments can be drawn from the interface.^[90,91] The two oppositely charged polyelectrolyte solutions or dispersions form gel complexes at the interaction layer. Pulling this gel upwards leads the reformation of the gel structure at the interface between the droplets and enables a continuous drawing of filaments.^[92] The pulling speed, the ionic strength and the pH are the process parameters that determine the properties of the filaments such as thickness and degree of alignment of the polymers within the filaments.

Two attractive biological fibrillar building blocks, combining physical and functional properties, are amyloid fibrils and cellulose nanofibrils (CNF). Previous research has shown that wet spun IPC filaments from amyloids can achieve tensile strengths of up to 326 MPa,^[185] whereas IPC filaments from CNF has been successfully combined with cationic polymers into strong cohesive assemblies.^[186–188]

The production of materials using oppositely charged particles or polymers is conceptually interesting as it allows the formation of composite materials without the need of further cross-linking, thus reducing process complexity. Optimizing material applicability, however, requires to carefully control the miscibility of the components as well as the timescales over which they form complexation leading to the formation of an entangled gel network. Therefore, shearing of the system should be avoided since it may lead to breaking of the formed gel into fragments, which impedes the formation of a monolithic network.^[108]

Due to their reducing properties, BLG-fibrils are able to reduce Au⁺ ions to gold nanoparticles or, when the BLG-fibril concentration is high enough to form nematic phases, to crystalline Au platelets.^[94,95] These gold platelets are a few nanometers thin and several micrometers in length. This allows the coverage of large areas with a minimal amount of gold.^[96] These gold materials have the ability of electrical conductivity shaped as films as well as in bulk.^[96,97] However, films produced from BLG-fibrils are generally very brittle. The combination of BLG-fibril dispersion containing Au-crystals with CNFs therefore offers a promising improvement of the mechanical properties.

Generally, large polyelectrolytes or charged colloids have previously been combined with a

smaller oppositely charged molecule that served as a crosslinker. The combination of two oppositely charged fibrils has, to the best of our knowledge, not yet been studied. In this paper we present the complexation of negatively charged CNFs with positively charged amyloid fibrils to first understand the mechanism of the complexation and in a second step use this knowledge to develop a proof-of-concept for preparing composite filaments as well as a self-assembled core-shell structure with a conductive gold crystal core and an insulating CNF shell.

EXPERIMENTAL SECTION

Production of TEMPO-CNF and BLG fibrils

TEMPO-CNFs were received from the Laboratory for Cellulose & Wood Materials, EMPA. The production was performed using TEMPO-mediated oxidation according to the protocol from Saito et al.^[29] Instead of sonication, the cellulose pulp was processed using high-pressure homogenization until a transparent dispersion of around 0.7 wt% was obtained. The dispersion was thereafter concentrated under constant airflow up to 2.2 wt%.

Amyloid fibrils were prepared following the protocol from Vigolo et al.^[189] In short, the fibrillization of purified BLG took place at 90°C, pH 2 during 5 h under continuous mixing at 100 rpm in an oil bath.^[100] After the fibrillization process, the BLG-fibril dispersion was quenched in ice water. To remove agglomerates, the dispersion was thereafter centrifuged for 20 min at 4000 rcf. Additional purification for removing unreacted monomers and peptides was performed by dialysis against pH 2.5 MQ water using a 6-8 kDa regenerated cellulose membrane. After the dialysis, the pH was adjusted to 2 by the addition of HCl. Concentration to 5.6% was done using evaporation under continuous airflow.

Synthesis of gold crystals dispersion

Gold crystals (Au-crystals) were synthesized in a nematic dispersion of BLG-fibrils following a protocol earlier developed in our group.^[95] In short, to prepare 500 mL gold crystal dispersion, 16.6 mL of 0.1 M HAuCl₄ were added to 483 mL BLG dispersion (6.6 mg/mL, pH 2) and heated at 60°C overnight. The gold nanocrystal dispersion was then centrifuged at 4300 rcf during 30 min. The supernatant was carefully removed, and the pellets were re-dispersed with additional 1.5 mL pH 2 milli-Q water forming a concentrated BLG stabilized Au-crystal dispersion.

Polyelectrolyte interface tearing for IPC

Droplets of 300 µL of each oppositely charged fibril dispersions with various concentrations

were put next to each other on a hydrophobic surface (plastic petri dish). The two droplets were pushed together using a tweezer and the interface was continuously pulled in a steady slow motion, resulting in the formation of a gel filament.

Core Shell extrusion

Two approaches for the extrusion to form core-shell structures were followed. To produce the Au-crystal ink, Au-crystals (0.7 or 1.5 wt%) were mixed in a dispersion of 2 wt% BLG fibril. The first core-shell extrusion strategy relied on the injection of the Au-crystal ink directly into a dispersion of CNF. The so formed gel could thereafter be collected from CNF dispersion and further be proceeded. In the second approach a coaxial needle was used to directly extrude a composite filament with the Au-crystal ink as core and the CNF dispersion as the outer shell. These filaments were subsequently dried at ambient conditions and collapsed to film-like structures.

Drying methods

Formed hybrid filaments were either dried in petri dishes at room temperature for 24 h or 1 h in an oven at 60°C, resulting in flat, film-like structures. To study the extruded filaments with minimal structural change, the structures were super critical CO₂ dried. Therefore, the water in the gel was exchanged with ethanol by placing it in a 30 mL 50 % EtOH bath. After 24 h a solvent exchange was done to 30 mL 97 % EtOH and the last one again after 24 h with 15 mL 99 % EtOH, followed by supercritical CO₂-drying (Tousimis, autosamdri 931).

Atomic force microscopy (AFM)

To prepare samples for AFM, a droplet of 20 µl of dispersion (amyloid fibrils, cellulose fibrils, gold platelets) was deposited onto freshly cleaved mica, incubated for 30 seconds, and dried with pressurized air. AFM measurements were performed on a MultiMode VIII Scanning Probe Microscope (Bruker, USA) in tapping mode using commercial cantilevers (Bruker, USA) under ambient conditions. The AFM was covered with an acoustic hood to minimize vibrational noise.

Transmission electron microscopy (TEM)

Liquid dispersions were prepared for TEM measurements by placing 5 µl of sample on glow discharged (Emitech K100X, GB) carbon coated grids (Quantifoil, D) and allowed to remain in contact with the grid for 60 sec. After this time interval excess fluid was blotted with a filter paper and the wet sample was stained with a drop of 2 % uranyl acetate for 1s followed by blotting and a second immersion step in uranyl acetate for 15 s. Excess moisture was thereaf-

ter drained with filter paper and the imaging of the air-dried grids was done in a TEM Morgagni 268 (Thermo Fisher Scientific, USA) operated at 100 kV. For gel-like samples the carbon-side of the grid was placed on a fresh surface and the sample was allowed to adsorb for 15-30 s. The further steps were the same as for dispersions.

Scanning electron microscopy (SEM)

Small pieces of super critical CO₂ dried wires were mounted on SEM aluminum pin stubs with double-sided adhesive conductive carbon tape. The edges of the samples were carefully cut in a flat angle with a razor blade and for selected samples also longitudinal cuts were done before sputter-coating with 4 nm of platinum/palladium (CCU-10, Safematic, CH). Secondary electron (SE)-in lens and Everhart-Thornley (ET) SE-images were recorded at a working distance of 4-5 mm with a scanning electron microscope (Merlin FE-SEM, Zeiss, DE), operated at an accelerating voltage of 1.5 kV.

Transmission electron microscopy (TEM)

Ultrathin cross-sections of ~ 60 nm thickness for TEM were obtained from a wire embedded in methacrylate resin. 3 mm pieces of wire were soaked in LR White Resin (Polysciences, Inc., USA) for 30 minutes under vacuum. Afterwards, embedding in 100% LRwhite was continued for 3 days at 4°C with 2 changes of resin. Polymerization was done at 60 °C for 48 hours in closed Eppendorf tubes. Ultrathin sections (~ 50 nm) were cut on a Leica Ultracut FC6 (Leica Microsystems, Vienna, Austria), transferred onto formvar coated carbon-grids (Quantifoil, D) and poststained with uranyl acetate. Imaging was done in a TEM Morgagni 268 (Thermo Fisher Scientific, USA) operated at 100 kV.

Conductivity measurements

Conductivity measurements were done using a Multimeter (Uni-T true rms ut61e 22000) in standard relative room humidity (40%) with a four-point probe conductivity method using an Agilent B1500 Semiconductor Device Analyzer. To be able to connect the four probes to the conductive core, the wire was cut on both sides and liquid metal - Eutetic Gallium Indium (EgaIn) - was used to build a connection between the core and the probes.^[190,191]

Thermogravimetric analysis (TGA)

Liquid dispersions were prepared for TGA by placing 50 µL of the sample in the pan, drying it at 60°C and subtracting the weight of the dry pan. The TGA machine was operated under O₂ gas flow using a linear temperature increase of 10°C/min up to 800°C.

RESULTS AND DISCUSSION

Concentration dependent interaction strength between BLG and CNFs

The interaction of protein as monomeric building blocks combined with cellulose is well known.^[101,192] However, the mechanism becomes complex when much bigger molecules such as polymers are involved. Electrostatic complexation is a thermodynamic driven interaction and thus has a much faster time scale than their diffusion. Therefore, the formation monolithic gels by electrostatic complexation of polymers is probably not possible. However, there are several options to overcome these problems. Peng and coworkers used a cellulose matrix where they added BLG monomers and heated the mixture at 95°C promoting the formation of amyloid fibrils. This procedure allowed them to obtain a homogeneous bulk material consisting of a double-network of CNF and BLG-fibrils.^[106,107] A second method combining CNF and BLG-fibrils is IPC. This technique enabled us the combination of two well-characterized fibrillar systems, avoiding uncertainties in the fibrillization process of BLG-fibrils. The fibrillization of amyloids is extremely delicate and their properties can be changed by impurities and seeds of the cellulose matrix.^[193] Hence, we chose this second strategy for the formation of our hybrid material.

Figure 1A,B shows AFM height images of BLG fibrils and CNFs, respectively. Mixing the two fibril dispersions in bulk lead to the formation of precipitating gel fragments. However, the AFM image of the mixture confirms the interaction of the two oppositely charged polymers (Figure 1C). IPC fiber spinning from the interface of two droplets of CNF and BLG-fibril dispersions allowed pulling long filaments from the interface (Figure 1D). The SEM image of the wet spun IPC filament shows nicely alignment within the direction of pulling (Figure 1E). Figure 1F is an AFM height image of a representative Au-crystal produced by adding Au⁺ ions in a dispersion of BLG-fibrils and heated at 60°C overnight.

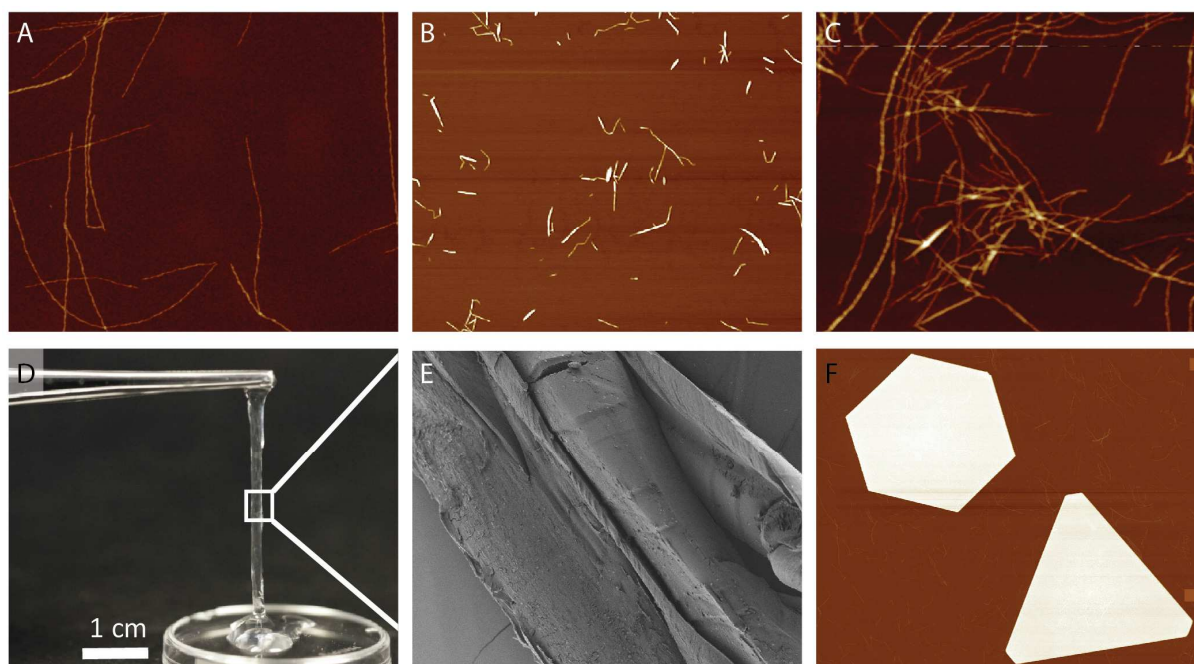


Figure 1: A) AFM image of BLG-fibrils. B) AFM image of CNFs. C) CNFs and BLG mixed in bulk and diluted to allow for single molecule imaging by AFM. D) Wet spun IPC filament from CNF and BLG. E) SEM image of a wet spun CNF-BLG ICP filament. F) AFM height image of gold crystals formed by incubation in nematic BLG fibril dispersion, imaged by AFM.

To find the optimal conditions for the interaction of the two polyelectrolytes, we mixed BLG-fibril dispersions and CNF dispersions at different concentrations and found that a minimum concentration of BLG-fibrils is needed to form self-standing filaments (Figure 2). Moreover, the best results for fiber pulling were achieved when the concentrations of the two polymers were roughly the same. An important remark at this point is the fact that the two dispersions have very different rheological properties. The transition to a gel-like behavior of CNF dispersions is around 0.5 wt%,^[134] whereas the gel transition of BLG-fibril dispersions is at a concentration one order of magnitude higher.^[194] Thus, the upper concentration we were able to use was limited by the viscosity of the dispersions. In our experiments, the longest filaments (> 5 cm) were produced by ratios of BLG to CNF between 3:1 and 1:1 (blue region in Figure 2). The general observed trend was that the higher the fibril concentration the longer were the drawn filaments. We obtained the longest filament at a concentration of 2 wt% BLG-fibrils and 0.7 wt% CNFs.

The control experiment using 0 wt% BLG-fibrils showed that that the decrease in pH alone does not lead to self-standing filaments. Thus, only the interaction of the two polymers allowed the formation of a structure strong enough to be withstand the tensile stress during pulling.

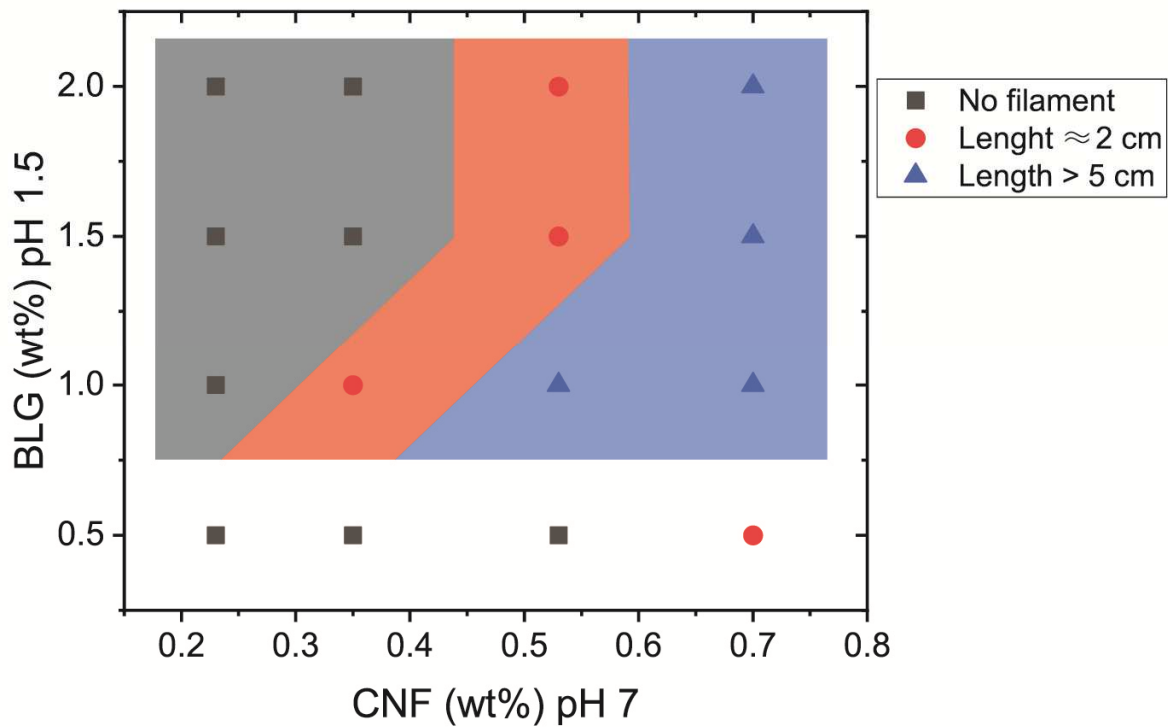


Figure 2: Phase diagram of the interaction between CNF and BLG-fibrils at various polymer concentrations. The described lengths are an average of three pulled fibers. The colored areas describe the following ratios of BLG-fibrils to CNF: grey > 5:1, red > 3:1, blue > 1:1.

Wet spinning of composite filaments

The phase diagram helped us to gain knowledge of the interactions to form mechanical strong filaments. However, as we observed by SEM (Figure 1E), IPC fiber spinning lead to filaments where the interface of the two phases was rough and not well defined. In an effort to improve the structure and interface between the phases, we investigated the possibilities to form core-shell structures by injecting the BLG-fibril dispersion in a coagulation bath containing CNFs. Using this technique, we were able to produce well defined core-shell filaments, that we could remove from the coagulation bath piercing the filament on syringes (Figure 3B). This setup allowed controlled drying in two dimensions whereas the length of the filament could be maintained (Figure 3C).

Since both fibril dispersions are rather transparent, it was not possible to distinguish between the BLG core and the surrounding CNF layer. Therefore, we added Congo-red or Au-crystals to the BLG-fibrils as visualized in Figure 3A. However, we do not know in what way Congo-red interacts with the fibrils and their morphology and functionality is maintained and additionally, the Au-crystals have the advantage of having a different density than BLG-fibrils, granting contrast for the analysis by SEM and TEM. Thus, further we used the Au-ink, where

we know, that the BLG-fibrils are not affected. Figure 3D shows the Au-ink injected in the CNF coagulation bath and Figure 3E the supercritical CO₂-dried filament.

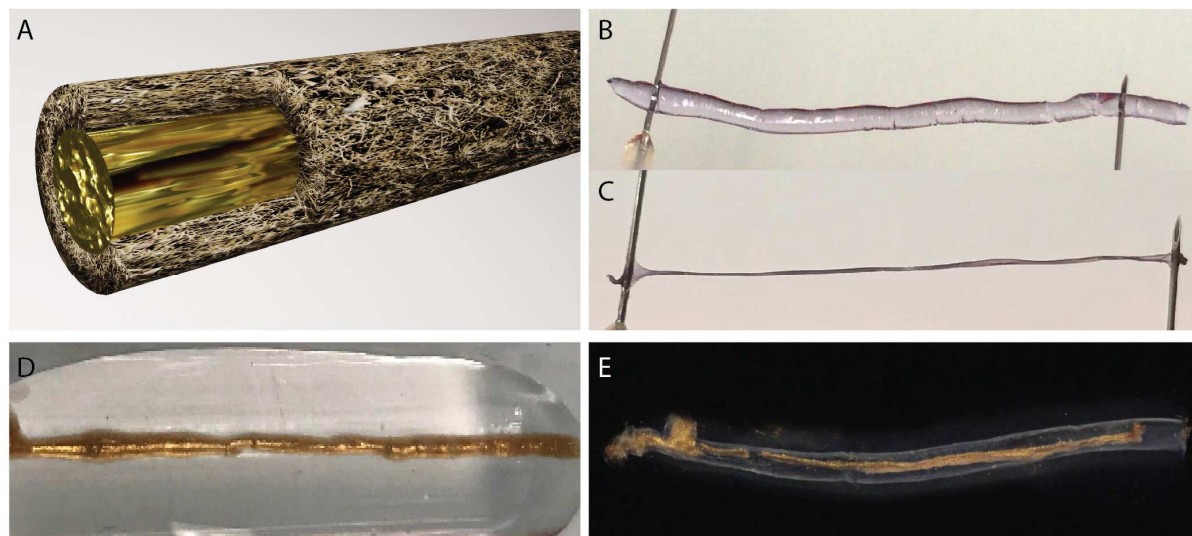


Figure 3: A) Schematic of a filament with a gold core surrounded by an insulating shell out of CNFs. B) Filament produced by the injection of BLG-fibrils into a coagulation bath containing CNFs in the wet state and C) air dried pierced on syringes. D) Filament composed of an Au-ink core in the CNF coagulation bath. E) Supercritical CO₂-dried filament from previous image.

The structural analysis of the dried filaments was extremely challenging due to the collapse of the structure coming from the capillary forces during ambient drying. Supercritical CO₂-drying had the advantage to empower the preservation of the interesting structural features. Closer investigation of the supercritical CO₂-dried samples allowed to gain microscopic insights into the bulk phases as well as at the interface between the BLG and CNF phases (Figure 4A,B).

We were able to cleave the filament at the interface of the BLG-fibrils and CNFs. This revealed that the fibrils of both components close to the interface were aligned, probably resulting from the shear forces during the extrusion process.

The CNF bulk phase did not show alignment at all and looked like a aerogel structure previously reported (Figure 4D).^[134] The Au-crystals in the BLG-fibril matrix appear to have a certain alignment, what can be rationalized due to the injection process and the much higher inertia of the big Au-crystals (Figure 4C). Again, this phenomenon may be explained by the shear flow during the injection and the much higher inertia of the huge Au-crystals compared to the small BLG-fibrils.

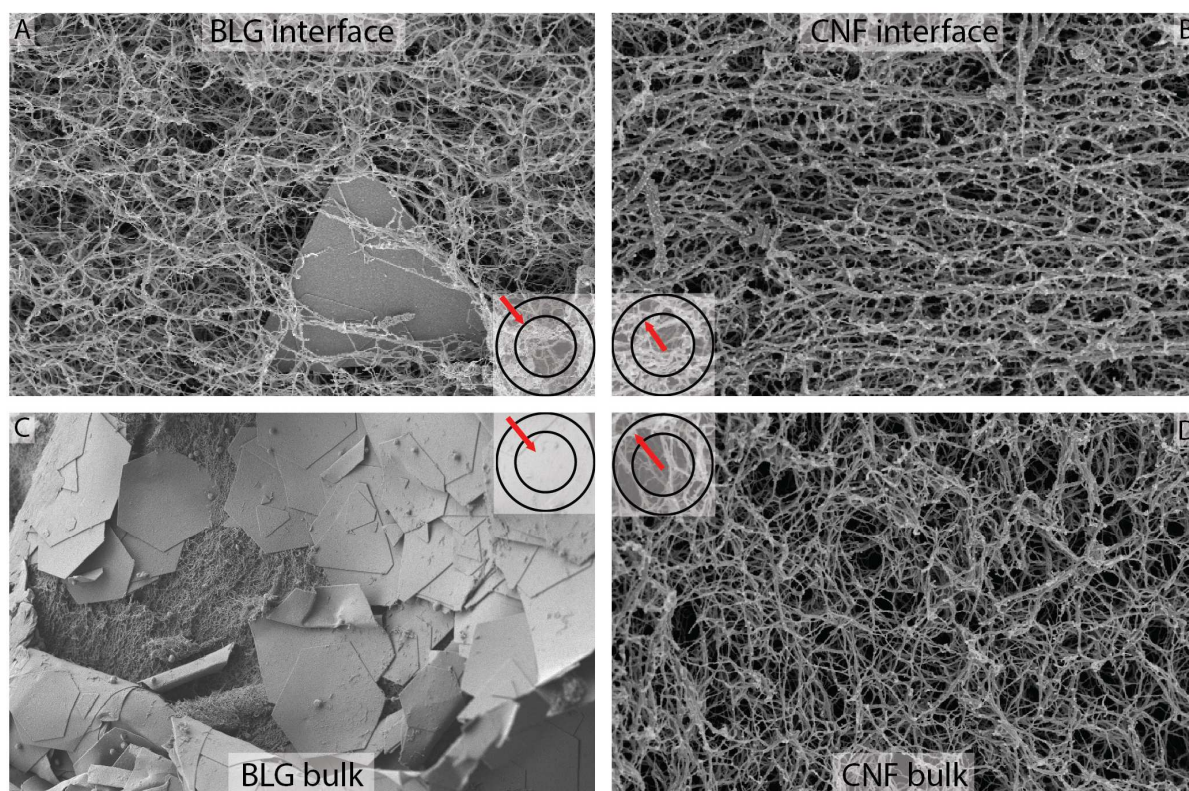


Figure 4: Nanostructure of supercritical CO₂-dried BLG-Au-CNF core-shell filament imaged by SEM filaments. The view on the interface of A) the BLG-Au-core and B) the CNF-shell, as well as the bulk phases of C) BLG-Au and D) CNFs.

Conductivity of core-shell filaments

The last challenge of the production of a conductive and insulating structure was to establish the minimal amount of conductive Au-crystal for the core as well as the right amount of insulating CNF to retain structural stability. The thickness of the CNF shell could be increased by lowering the pH of the Au-crystal ink from 2 to 1.5.

Tuning the composition of the Au-crystal ink was more complex. The concentration of BLG-fibrils needed to be high enough to stabilize the ink, in order to avoid precipitation of the Au-crystals, and nevertheless provide a viscosity suitable for extrusion. To guarantee conductivity, the Au-crystal density needs to be high enough for the crystals to be in contact with each other and form a coherent, connected system. A sample with an Au-crystal concentration too low to form an interconnected system is shown in the TEM image in Figure 5A.

Figure 5C provides an overview of the relation between the composition of the core and the conductivity. We found that the threshold for conductivity was at 11.4 mg/L of Au-crystals in the ink. By increasing the Au-crystal content of the ink to 17.1 mg/L, we could double the conductivity to 2.3×10^4 S/m, which is 3.5 orders of magnitude below the conductivity of pure gold (4.46×10^7 S/m).

The exact composition of the cold concentration was determined by TGA (Figure 5D), which revealed that the 17.1 mg/L Au-crystal ink has a dry content of 70 wt% gold and 30 wt% BLG-fibrils. Compared with previously reported results, we found a threshold of conductivity around 20% lower.^[96]

In the previous work, the authors produced a film by filtration of the BLG-Au-crystal dispersion through a cellulose membrane. Thus, the alignment of the Au-crystals in the films is certainly different than in our filaments. However, this highlights the importance of shear alignment of the Au-crystals for maximal conductivity.

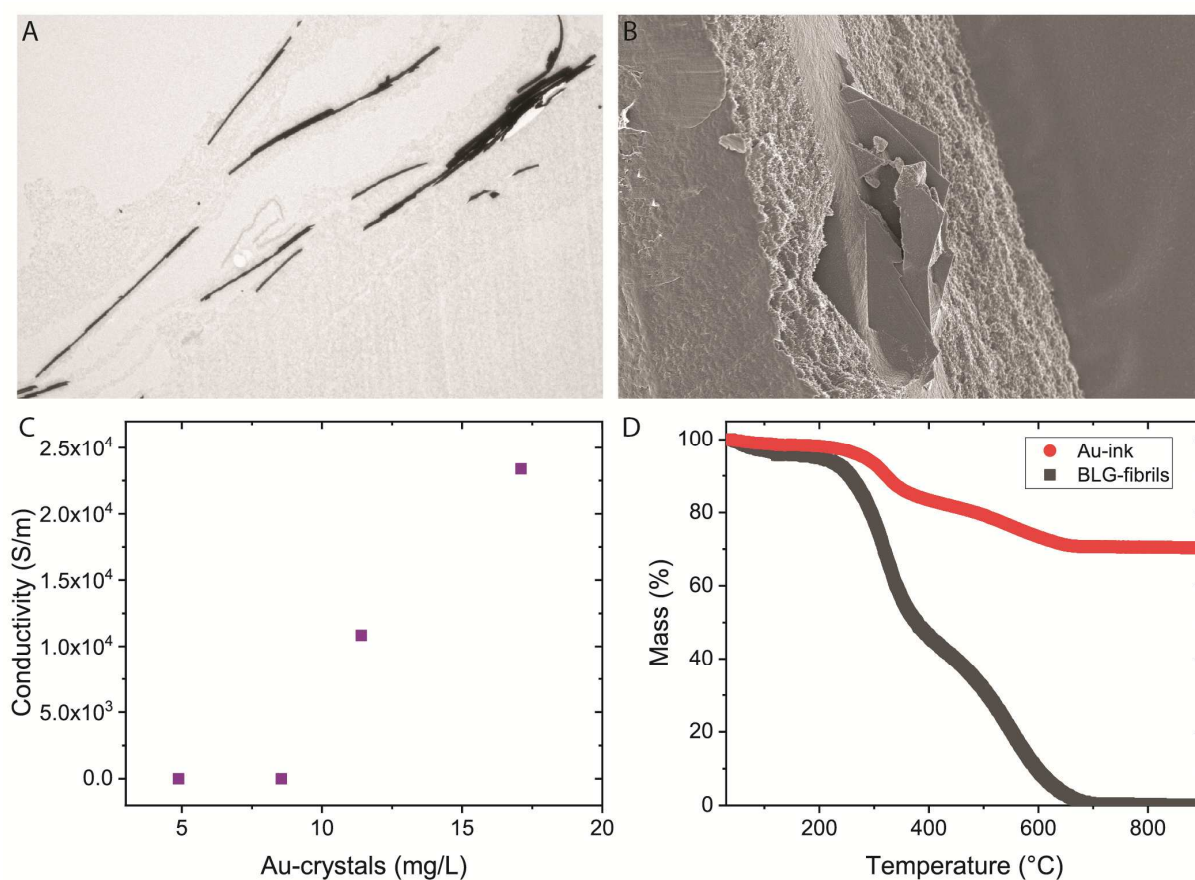


Figure 5: Conductivity of the insulated gold-filament. A) TEM image of the BLG-Au-core with an Au-crystal concentration too low for them to be in contact. B) SEM image of the cross-section of an air-dried filament revealing the gold crystals in the center, surrounded by aligned BLG fibrils. C) Dependence of the conductivity of the filament on the Au-crystal concentration. D) TGA of and Au-crystal ink and the pure BLG dispersion.

CONCLUSIONS

Interfacial complexation of cationic BLG-fibrils and of anionic CNF allowed drawing filaments from the interface forming between the two dispersions. The length and integrity of these filaments were found to depend on the ratios of fibril concentrations. A ratio of below 3:1 and above 1:1 of BLG-fibrils to CNFs allowed to form the longest filaments. AFM, SEM

and TEM imaging enabled a detailed structural analysis of the created hybrid material. Oppositely charged fibrils were found to be colocalized, supporting the hypothesis of the attractive nature of these fibrils and their ability to form high cohesion mixed phases.

Using this knowledge, we created core-shell structured by injection of an Au-crystal ink into a coagulation bath containing CNFs. Optimize the Au-crystal core composition for its conductivity, we were able to significantly reduce the gold content for the conductivity threshold compared to previous reports. However, we think that also the shear-induced alignment due to the extrusion process contributed to the increased performance.

Our results provide insights into the interaction of CNFs and BLG fibrils as oppositely charged polyelectrolytes and we present a proof-of-concept for a conductive and insulating bio-composite as an example for an application might represent a basis for several sustainable, technological innovations in the future.

ACKNOWLEDGEMENTS

This project was funded by the Swiss National Science Foundation, Project No. 200021-175994 and Ambizione Grant No. PZ00P2_168023/1. Additionally, we thank Pascal M. Gschwend from the Particle Technology Laboratory for the help with TGA and Tian Tian from the Lab for Interface and Surface Engineering of Nanomaterials for the support with conductivity tests.

Conclusion of the thesis

As an ubiquitous and sustainable resource with excellent mechanical properties, cellulose has gained great popularity in current research. This thesis describes fundamental aspects of the isolation of cellulose nanoparticles and aims to relate these properties with the materials that they can produce. Nanocellulose has been used in wide-ranging applications such as in smart and responsive nanomaterials or as functional packaging materials and coatings. For an efficient use of the cellulose raw material as well as an optimal material functionality, it is essential to understand the influence of the production parameters of nanocellulose particles on the subsequent material processing.

Within my PhD project, I studied the structure-property relationships of TEMPO-CNFs over different hierarchical levels. Starting with a systematic characterization on the single CNF particle level, chapter 2 helped understanding the impact of production parameters on the morphology of CNFs extracted from two softwood pulps. Having a broad set of CNF samples where the individualization parameters (degree of surface oxidation, concentration and sonication time) were methodically altered, enabled an exact determination of their impact on fibril properties such as contour length and number of kinks per fibril. A highlight of this work was the discovery that the right-handed twist of the fibrils is depending on the charge density as provided by detailed AFM analysis.

In the succeeding project, presented in chapter 3, I used these well-characterized CNFs as building blocks to study the self-assembly and behavior of the particles forming bulk materials such as salt and proton induced hydrogels and thereof produced aerogels. The rheological analysis of protonation induced gels revealed a correlation between the average fibril length and G' at low concentrations. This correlation was used to approximate the mesh size from experimental values, and it was found to be in good agreement with scaling arguments.

With the differently charged CNF model fibrils from the first paper in hand, in chapter 4, we studied the interfacial adsorption of CNFs at the air-water interface and found a decrease in interfacial tension. The adsorption of CNFs and the reduction of surface tension were enhanced by decreasing the surface charge densities of the CNFs. Thus, the surface charges limit

both their adsorption and surface coverage at the air-water interface.

In the final manuscript, presented in chapter 5, I investigated the electrostatic complexation of anionic CNFs with cationic BLG-fibrils to form a bio-composite material by interfacial polyelectrolyte complexation. Altering the concentration and pH of each component resulted in different material characteristics. The addition of Au-nanocrystals in the BLG-fibril dispersion furthermore allowed us to produce conductive filaments that were stabilized and insulated by a surrounding layer of CNFs. The filaments were produced by extrusion of the Au-crystal ink into a coagulation bath containing CNFs or possibly by coaxial extrusion. These conductive filaments are a proof-of-concept representing an application where the properties of the final structure are controlled by the properties of its building blocks by a bottom-up approach.

In summary, I was able to produce a set of CNFs with various properties, allowing me to study the structure-property relationship of dispersions, hydrogels and aerogels, and the CNF adsorption at the air-water interface. Additionally, I investigated the formation of a hybrid material combining the CNFs with oppositely charged amyloid fibrils.

These findings provide a toolbox for designing TEMPO-CNFs with desired self-assembly responses to form specific structures and materials by a bottom-up approach. The ability of precisely controlling the routes of self-organization from nanostructure of the single particle to complex materials is essential for future advanced applications. In an ever-growing field of nanocellulose research, the contribution of the presented work is a combined perspective on the properties of CNFs as building blocks and their thereof formed structures.

Outlook

My work in the field of nanocellulose research could only answer a few of the many open questions and also generated new questions that should be answered to fully capitalize on the potential of cellulose materials. Here, I present some of the most promising ideas and discoveries that I was unfortunately not able to tackle in the extent of my thesis.

Starting with the findings on the morphological level of the single particles, I found the twist of the CNFs to be dependent on the charge density. Producing CNCs from differently twisted CNFs by acid hydrolysis might provide the opportunity to adjust the pitch of cholesteric phases in liquid crystalline systems as desired.^[47] This knowledge would allow the fine-tuning of material properties such as colors of liquid crystalline materials by a bottom-up approach. However, since both the twist as well as the charge density of the fibrils, influence the alignment of CNCs in the cholesteric phase, it is a challenging task to predict the properties of the thereof formed cholesteric phases and only an experimental approach might elude these relationships. It was reported that the diameter of CNFs might be influenced by the charge density as well as the sonication time.^[54] Our data pointed towards this effect, however, was not significant to confirm this claim. Going back to the twist of fibrils, it is not only the charge density, but also the diameter, or the second moment of area, that influence the twisting and thus the properties of the thereof formed cholesteric liquid crystalline phases, making predictions of the phase behavior even more complex.^[130,131]

A further unresolved topic remains the exact location of the charges on the TEMPO-CNFs' surfaces. It is still under debate whether the charges are evenly distributed along the fibril contour or if they are accumulated at specific positions. Resolving the location of the charges along the fibril contour might help to better understand the exact distribution of the crystalline and amorphous regions of CNFs. Using WAXS, we can exactly determine the ratio between the two domains, but not the arrangement. The accumulation of charges at positions of kinks could be correlated with amorphous regions. Finding highly charged regions would either mean that not all kinks are observed by AFM or it would support the theory about altering

amorphous and crystalline domains. Alternatively, finding evenly distributed charges would point towards the theory of a crystalline core and an amorphous shell.

Polymers such as CNFs, BLG-fibrils or polysaccharide form extremely porous networks. Unlike in cryogels, where the pores are defined by the growing ice-crystals, in polymer aerogels, these distinct pores are missing. This inevitably leads to the problem of how to determine and measure the size of a pore. So far, there are no 3D imaging techniques resolving on the length scale of polymers. Thus, an evaluation and confirmation of the concept for the determination of the mesh size presented in chapter 4 by other polymer systems becomes important.

To produce strong and robust aerogels from individualized CNFs, minimizing shrinkage and damage from humidity, functionalization becomes inevitable. Consequentially, to really understand the structure-property relationship of the functionalized CNFs, an analysis of the complete procedure must be repeated in a similar way to the here presented work. This process is extremely time consuming and there may be ways to correlate and adapt my findings to other systems.

In perspective of gaining the knowledge and using it for finalized and customized applications on an industrial level, there are already a few examples such as the Kyoto-Process (CNF composite material e.g. for car industry), 3D printing and civil engineering. However, I believe materials and composites from nanocellulose have the potential to replace a lot of the traditional materials in the field of electronics, optics, construction and engineering, pharmaceuticals, healthcare and food production. In this regard, refined particle synthesis and careful bottom-up material assembly may contribute to a more responsible and sustainable handling of the available resources.

Further related content

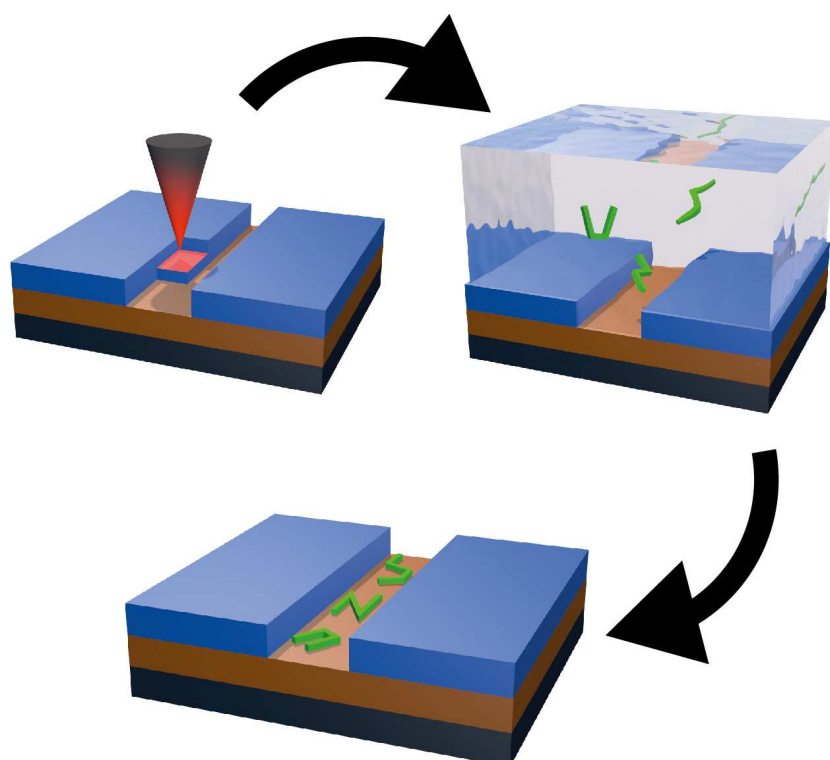
Confinement-induced ordering and self-folding of cellulose nanofibrils

K. B. Smith, J-N Tisserant, S. Assenza, M. Arcari, G. Nyström and R. Mezzenga

Advanced Science 2019, 6, 1801540

<https://doi.org/10.1002/advs.201801540>

Reproduced with permission from Wiley-VCH.



Confinement-induced ordering and self-folding of cellulose nanofibrils

Kathleen Beth Smith, Jean-Nicolas Tisserant, Salvatore Assenza, Mario Arcari, Gustav Nyström, and Raffaele Mezzenga

Department of Health Sciences and Technology, Swiss Federal Institute of Technology in Zurich, 8092 Zurich, Switzerland

Nanotechnology Group, Swiss Federal Institute of Technology in Zurich, 8803 Rueschlikon, Switzerland

Institute for High Frequency Technology, Braunschweig University of Technology, 38106 Braunschweig, Germany

Laboratory for Applied Wood Materials, Empa, 8600 Duebendorf, Switzerland

Department of Materials, Swiss Federal Institute of Technology, Zurich, 8093, Zurich

E-mail: raffaele.mezzenga@hest.ethz.ch

Abstract

Cellulose is a pervasive polymer, displaying hierarchical length scales and exceptional strength and stiffness. Cellulose's complex organization, however, also hinders the detailed understanding of the assembly, mesoscopic properties, and structure of individual cellulose building blocks. This study combines nanolithography with atomic force microscopy to unveil the properties and structure of single cellulose nanofibrils under weak geometrical confinement. By statistical analysis of the fibril morphology, it emerges that confinement induces both orientational ordering and self-folding of the fibrils. Excluded volume simulations reveal that this effect does not arise from a fibril population bias applied by the confining slit, but rather that the fibril conformation itself changes under confinement, with self-folding favoring fibril's free volume entropy. Moreover, a nonstochastic angular bending probability of the fibril kinks is measured, ruling out alternating amorphous–crystalline regions. These findings push forward the understanding of cellulose nanofibrils and may inspire the design of functional materials based on fibrous templates.

Introduction

Over the last few decades, materials science has taken a turn towards smart, green materials.^[195] One source of inspiration for such materials comes from nature itself, where the pre-programmed features of individual building blocks self-assemble and fold into extremely complex and hierarchical structures.^[196–198] Although one most commonly thinks of DNA and proteins when considering such natural systems, another incredible natural material is cellulose,^[13] the most abundant organic polymer on the planet.^[199]

Cellulose shows fascinating order and hierarchy over multiple length-scales.^[200] This, combined with its high stiffness and specific strength, has made it a prime component in the fabrication of self-assembled materials such as hydrogels,^[114] nematic liquid crystals^[35] and even chiral nematic films.^[201] The assembly of the cellulose into these highly-ordered materials has been well studied,^[2,10] as well as the structure of cellulose crystals on the atomic level.^[7] However, little is known about the structure and assembly of cellulose particles between these two length scales.^[2] Thus, the full potential of self-assembled hierarchical cellulose materials is yet to be reached, as studying and understanding single particles at different length scales is paramount for rational material design.^[202] This concept is epitomized by DNA, where the assembly mechanisms of its different building blocks are so well established that one can engineer it to fold and self-assemble into highly complex patterns.^[203–205] This has enabled the recent development of an impressive amount of DNA-based applications and technologies.^[205–208] In spite of its potential, precisely self-assembled cellulose nanostructures and materials are still to be realized, due to the lack of detailed understanding of the mechanisms ruling mesoscopic structures.

One of the smallest building blocks used in cellulose-based self-assembled materials is the cellulose nanofibril (CNF).^[29] It is known that the processing of the cellulose can influence the length, aspect-ratio and degree of polymerization within the fibrils.^[43,44] It has also been discussed that the kinks along the fibrils may be due to mechanical treatment and hence depending directly on the processing conditions.^[45] Further theoretical work has been done by Ciesielski^[126] where the kinks were described by energy minimization along certain crystal-line planes. However, there is still no clear explanation as to their exact nature. In order to better understand the structural properties of the CNFs, how to manipulate the mesoscopic features and gain further insight on the nature of the kinks in view of its relevance for practical applications, the effect that confinement has on the individual fibrils was studied. Confinement was chosen as it has been extensively studied both theoretically^[209–211] and, in recent years, experimentally.^[212–216] It is known to reveal structural information or change in topolo-

gy of the constrained elements.^[212,215,217] A noteworthy example of this was observed by Japaridze et al.^[215] in the case of circular DNA, where they observed hairpins at the nicked regions of the DNA plasmids when under strong confinement. These structural defects could be analogous to the kinks observed in CNFs, bringing a strong motivation to study them under confinement. In addition, confinement is known to create order and alignment, a crucial parameter that bio-inspired materials try to reproduce.^[197,218] Therefore, confinement can provide more than just much-needed structural information, it can also give an overall picture of how the fibrils and other similar biomolecules behave during certain material processing where confinement by geometry and increase in concentration are used to induce macroscopic ordering and self-assembly.^[64,218,219] Most confinement experiments are accomplished using microfluidics combined with optical imaging and staining of the molecules.^[212–214] In this study, our goal was to obtain high-resolution images while avoiding perturbations of the fibril structure due to staining. This was achieved by utilizing a novel thermal scanning probe lithography technique^[220] to create confinement patterns, in which fibrils were deposited by adsorption. The CNFs were then imaged under confinement using atomic force microscopy (AFM) techniques, and subsequently single molecule statistics was performed on the confined fibrils. Our results show the expected alignment and most surprisingly, a net folding of the CNFs. In order to determine whether the slits were acting as topological filters for fibrils with a higher kink count, geometry-based simulations were carried out. Simulations consisted in testing which fibrils, generated from the unconfined statistics, would fit into an implemented confined geometry. The subsequent sub-population showed that the observed net-folding could not be explained by selectivity of the slits for a specific fibril population, but rather by a conformational change of the fibrils themselves. Further a preferential bending direction of the CNFs was observed, which provides additional experimental evidence to the fact that amorphous and crystalline regions cannot alternate along the contour length of CNFs.

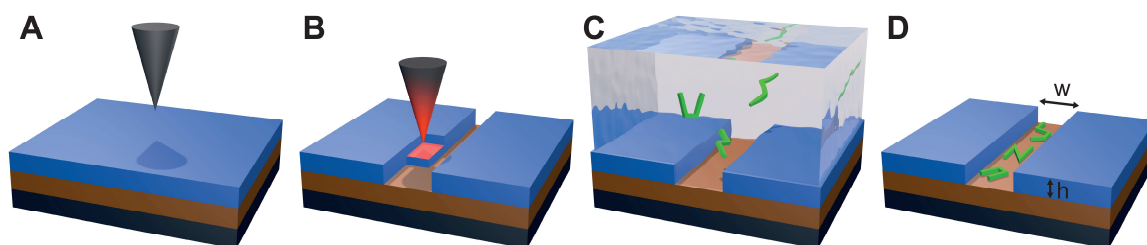


Figure 1: Experiment overview. A) Stack of pre-patterned substrate. Layers from bottom to top: silicon wafer, P4VP, and PPA. B) Patterning of the substrate by thermal probe lithography. C) Deposition of the CNFs by adsorption through specific electrostatic interactions. D) Final sample displaying folded CNFs in a slit of width w and height h .

Results

The confinement of cellulose nanofibrils of average contour length $\langle L \rangle \approx 600$ nm was studied on prepatterned PPA/P4VP substrates (see materials and methods) having rectangular slits of depth $h = 60$ nm and width w varying between 0.75 and 9.50 μm , Figure 1. PPA is a thermally cleavable polymer that can be removed locally by a thermal probe as shown in Figure 1A,B. P4VP is a polycation chosen to attract the fibrils by electrostatic interaction.

The degree of confinement in such patterns can be quantified by $\langle L \rangle/w$. As depicted in panels C and D of Figure 1, CNFs display sharp bends in otherwise stiff segments. These bends are referred to as kinks. The main traits of the CNFs are the number of kinks, the kink angles, and the contour length. All further characterizations of the fibrils are constructs derived from these features. In addition, the area occupied by each fibril can be characterized by the normalized mean square radius of gyration $(R_g/L)^2 = \frac{1}{NL^2} \sum_i^N \langle (\vec{r}_i - \vec{r}_{cm})^2 \rangle$, with \vec{r}_i the segment vector i along the contour length, and \vec{r}_{cm} the center of mass of the chain.

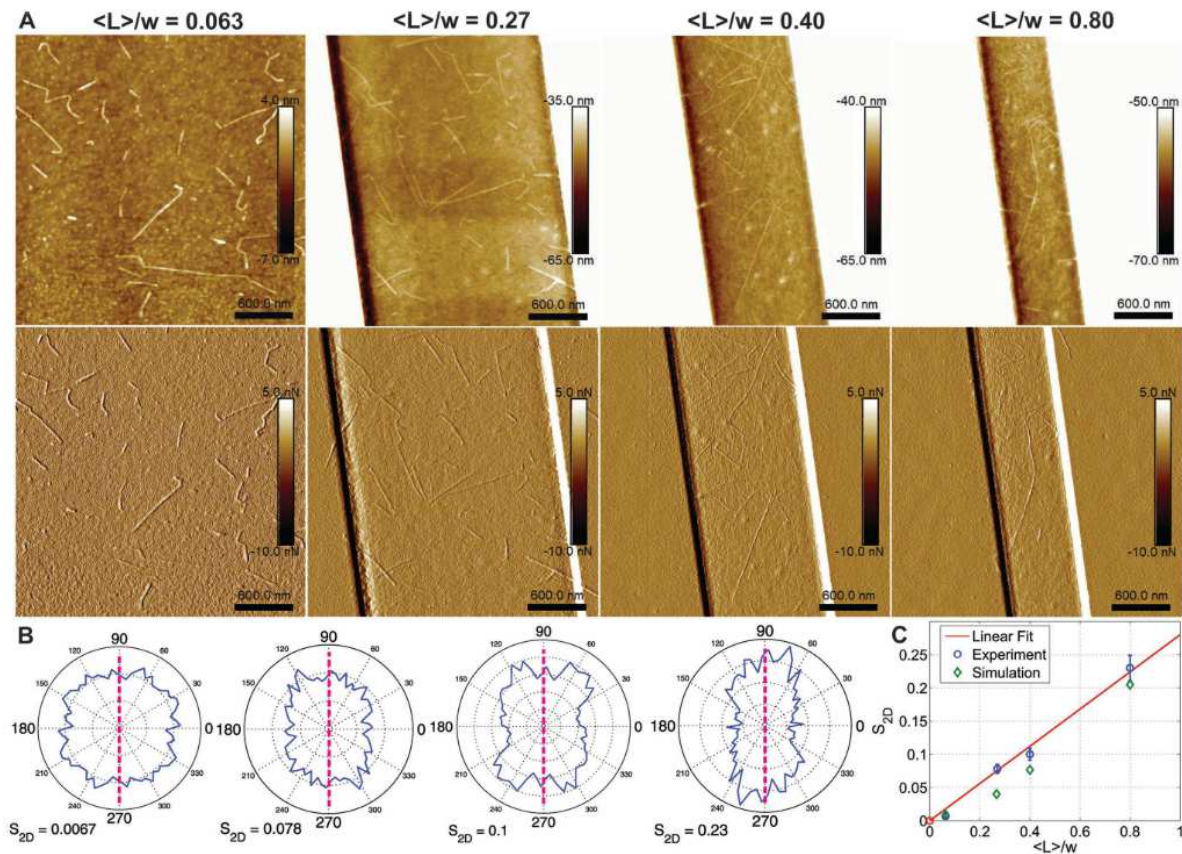


Figure 2: Alignment of cellulose in slits. A) AFM images (top height, bottom peak force error channel) of cellulose in slits of $\langle L \rangle/w$ ratios of 0.063 (unconfined), 0.27, 0.40 and 0.80 (left to right). B) Full statistical orientation distributions of fibrils in slits for $\langle L \rangle/w$ ratios of 0.063, 0.27, 0.40 and 0.80 (left to right), where the dashed pink line represents the slit long-axes. C) Experimental S_{2D} (blue circles) and simulated S_{2D} (green diamonds) as a function of $\langle L \rangle/w$. Linear fit (red line) forced through 0, of R^2 of 0.988 and RMSE of 0.0101.

Alignment

Confinement is well known to induce an orientation of the object along the long axis of the slit. In the case of a rigid rod, the degree of alignment in a slit has an exact analytical solution. For ideal flexible and semiflexible chains, seminal theoretical work has been done by de Gennes^[209] and Odjik,^[210,211] where de Gennes elaborates his "blob" theory under weak confinement, e.g. $R_g \sim w$, with R_g the radius of gyration, and Odjik describes the chain as a series of detecting segments when under strong confinement, e.g. $R_g \gg w$. The kinks in CNF make it an interesting case somewhere between a rigid rod and semi-flexible polymer. This justifies the use of $\langle L \rangle/w$ to quantify the degree of confinement.

In Figure 2A AFM images were chosen to show this effect on the CNFs in slits of $\langle L \rangle/w$ ratios of 0.063, 0.27, 0.40 and 0.80. This alignment was quantified in two ways: by plotting the orientation distribution (OD), as shown in Figure 2B, and by calculating the S_{2D} order parameter given by $S_{2D} = \langle \cos(2\theta) \rangle$,^[128] where θ is the angle between the n th segment and a local director. The OD plots clearly show a trend from isotropic to anisotropic average particle direction. It can be observed that though the component in direction of the confinement gets increasingly narrower, the rectangular shape is well preserved. This is attributed to the distinct morphology of the nanocellulose fibrils.

The S_{2D} order parameter increases linearly as a function of confinement, as seen in the Figure 2C. (This fit has a R^2 of 0.988 and RMSE of 0.0101). It was assumed in the zero intercept of this fit that an infinite slit width would yield a purely isotropic fibril distribution. To better understand this trend, the values were compared to those of simulated CNF in confinement (green diamonds). A full explanation of the simulations can be found in the Materials and Methods. In short, fibrils of fixed contour length $\langle L \rangle$, with corresponding statistics extracted from the distributions of the unconstrained case, were generated and placed in a slit of width w . If the fibril fit into the slit it was taken into the statistics, if not it was discarded. The simulated values of S_{2D} were obtained by simulating fibrils in slits with various L/w ratios and taking the sum of these S_{2D} weighted according to the experimental contour length distributions (see SI) normalized by w . We observe that the simulated values are systematically lower for the confined cases. This can be justified by the fact that we used a fixed kink angle, that the implemented statistics are exact only for $\langle L \rangle$, and that the simulations do not take the fibrils excluded volume into account.^[209,216] The excluded volume was therefore estimated from that of a rigid rod in 2D (for this reason we will refer to an excluded area). For a CNF of same length, this approximation should overestimate the actual excluded area. From Onsager's theory,^[221] we calculated the excluded area for rigid rod in the limit of $L \gg d$, with d the diameter

of the rod, to be $\frac{2L^2}{\pi}$ (see SI). If we compare this to the area available to each fibril (values extracted from AFM images), see Figure S2 in the Supporting Information, the estimated values showed that in certain cases, especially at the ratio $\langle L \rangle/w = 0.27$, we could have an additional alignment from the fibrils interacting with each other.

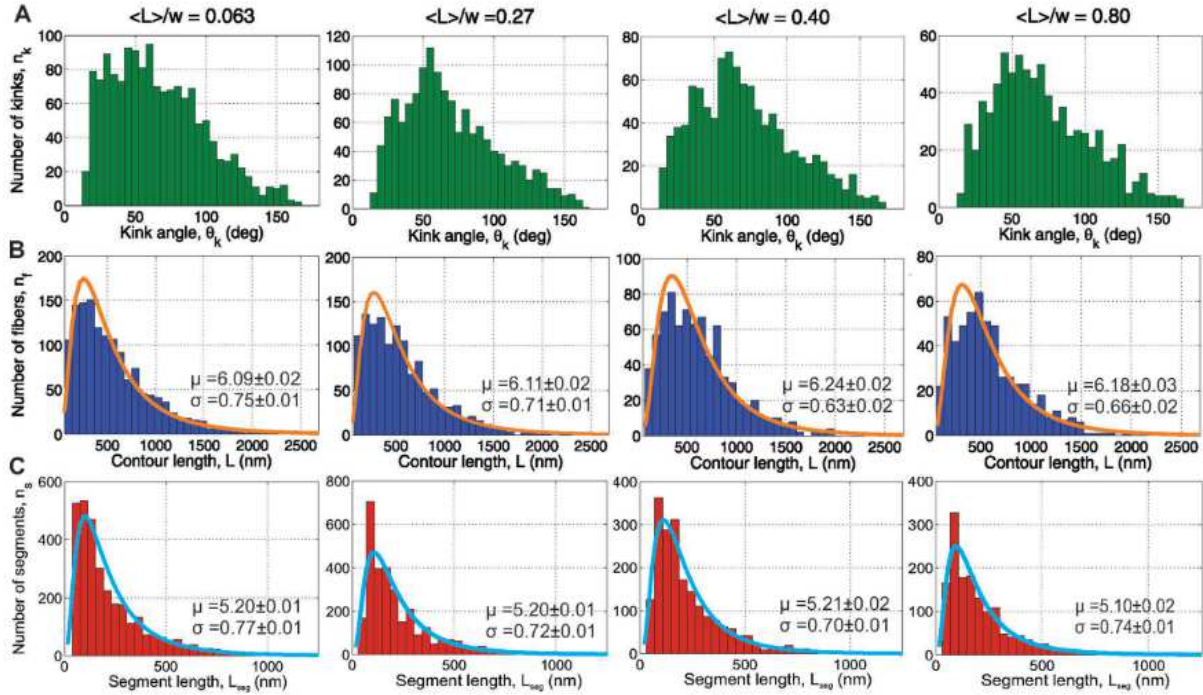


Figure 3: Full Statistics Distributions. In all distributions the number of counted fibrils for the different confinements are: 0.063 - 1420, 0.27 - 1286, 0.40 - 791, 0.80 - 562. A) Kink angle distributions. B) fibril contour length distributions with lognormal fit (μ and σ fit parameters given on the plot). C) Segment length distributions with lognormal fit (μ and σ fit parameters given on the plot).

Fibril conformation

It has been reported that confinement can influence the conformation of the confined elements.^[212,215,217,222] Consequently, different fibril attributes were investigated, the full detailed distributions of which can be seen in **Figure 3**. We observe a shift towards higher values in the kink angle distribution under confinement, as well as a decrease in the tail of the segment length distributions. The contour length, however, is left more or less undisturbed.

To better visualize the effect of the slits on CNFs, mean values of fibril characteristics were extracted from the full statistics and plotted as a function of confinement, **Figure 4**. For each parameter, corresponding schematics depict the fibril conformation in the unconfined and confined states. Figure 4A shows the mean kink angle $\langle \theta_k \rangle$ as a function of confinement, with a subplot of $\langle \theta_k \rangle_{nk}$ for fibril subpopulations, identified by different number of kinks, $n_k = 1, 2, 3$. We observe that the overall $\langle \theta_k \rangle$ increases in confinement. We also note that the $\langle \theta_k \rangle_{nk}$ fol-

lows a similar trend with confinement, but also that $\langle \theta_k \rangle_{nk}$ monotonically decreases with n_k .

Figure 4B shows the mean contour length $\langle L \rangle$, the mean inverse kink density $\langle \rho_k \rangle^{-1} = \langle (n_k/L) \rangle^{-1}$ (where n_k is the kink number), and the mean segment length $\langle L_{seg} \rangle = \langle L/(n_k + 1) \rangle$. Nyström et al.^[46] exploited these parameters to understand if the fibrils break along a segment or at a kink, or if a new kink is observed. Using their classification system, we could determine that we are observing more kinks per fibril in confinement (as our $\langle L \rangle$ is constant in the different slits but the $\langle \rho_k \rangle^{-1}$ and the $\langle L_{seg} \rangle$ decrease).

The combination of these two panels help to understand the results of Figure 4C. An overall decrease in the normalized 2D mean square radius of gyration $\langle (R_g/L)^2 \rangle$ is apparent once the fibril is confined. Taking into account that we observe both fibrils with more kinks and with higher kink angles, this result is expected as on average the fibrils are folding upon themselves under increasing confinement.

These results can be understood from an entropic point of view, as fibrils that are more bent can adopt more states in the slit than stretched out fibrils.^[217] In other words, while the change in configurational entropy of the fibrils is essentially equivalent between stretched and folded states, folding increases free volume entropy of the fibrils in the slit. It should be noted that this observation holds in a regime of weak confinement as $\langle L \rangle \sim w$, and that this effect cannot be extrapolated to strong confinement, which goes beyond the limits of our experimental procedure.

To determine if these results could be justified solely from a slit selectivity for existing fibril populations that would be entropically favorable, geometry-based simulations of the cellulose fibrils under confinement were performed (see the Experimental Section for details). The simulations showed a similar trend for the mean kink number $\langle n_k \rangle$, with an increase from 1.24 to 1.29 (i.e., 4%). However, the shift observed in the experiments was from 1.24 to 1.69 (37%), see Figure S3 in the Supporting Information. It could be argued that the averaged values used in the simulation are the source of this discrepancy. However, this possibility was discarded by performing a second set of simulations with CNFs of constant segment lengths and a maximum kink angle up to 160° . These features are typical of the fibrils occupying the smallest area observed in experiments, thus considering such a subpopulation provides an upper-boundary to the prediction range of a purely selective model. This second set of simulations showed only an increase in $\langle n_k \rangle$ of 10%, i.e., it still did not account for the experimental data. Therefore, it was determined that the geometry of the system is not solely acting as a conformational filter, but that it also has a direct influence on the conformation adopted by the nanofibrils. A model capable of quantitatively recapitulating the data would thus need to ac-

count for more complex features, such as detailed mechanical and structural features of single fibrils, adsorption dynamics, etc., but is well beyond the scope of this paper.

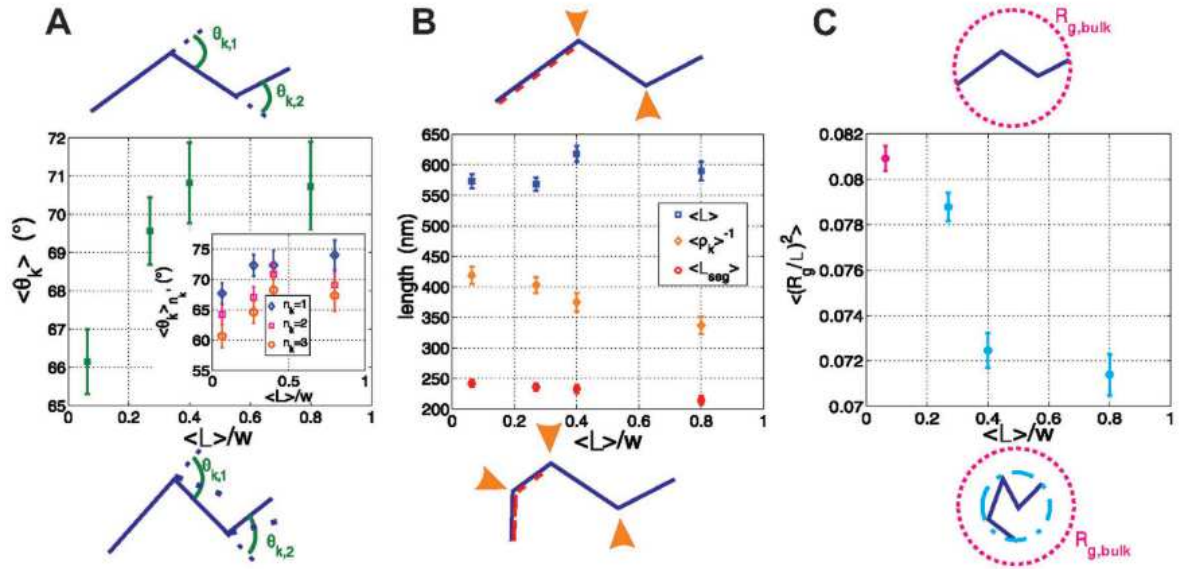


Figure 4. Fibril conformations in slits. Schematics at the top represent fibril parameters for the unconfined case, whereas those at the bottom represent the same parameters in the confined cases. A) Overall mean kink angle, $\langle \theta_k \rangle$, as a function of $\langle L \rangle/w$, with subplot of the mean kink angle per kink population, $\langle \theta_{nk} \rangle$ as a function of $\langle L \rangle/w$. B) Mean contour length $\langle L \rangle$ (blue squares), mean inverse kink density $\langle \rho_k \rangle^{-1}$ (green diamonds), and mean kink segment length $\langle L_{seg} \rangle$ (red circles) as a function of $\langle L \rangle/w$. C) normalized mean square radius of gyration $\langle (R_g/L)^2 \rangle$ as a function of $\langle L \rangle/w$.

Kink Populations

Usov et al.^[45] reported that the kink angle distribution of the nanocellulose does not follow a Gaussian distribution and is non-symmetric. This argument was used to support one of the two models^[223] used to describe the disposition of the ordered and disordered regions in cellulose fibrils and to suggest that the kinks were possibly a result of the preparation of the nanocellulose. Their results are in favor of the model of a crystalline core and amorphous shell. This evidence went also in the direction of the results of other studies.^[59,114,224–226] In this section, a similar argument to that of Usov et al. is proposed to further push the evidence towards the afore-mentioned model.

First, as observed earlier, the mean kink angle $\langle \theta_k \rangle_{nk}$ decreases systematically with n_k (Figure 4A). We propose to interpret these results as follows. Let us suppose kinks are formed from breaking to release an indicted strain. If the rupture happens in only one place, all the energy goes into breaking the fibril in that one spot, resulting in one deep break, see **Figure 5A** (top). Conversely, if two spots are involved the energy is shared between the two areas and therefore the breakage will not go as deep, see **Figure 5A** (bottom).

A further argument in favor of a stress-induced origin of kink formation comes from an analysis of kink bending directions. Let us look at the populations of fibrils with two or more kinks and assign a sign to the direction in which the fibril bent, see Figure 5B. For instance, following the contour of the fibril, if the fibril bent to the right, we determined the sign $s_k = +1$, if it bent to the left $s_k = -1$. Using these s_k values we calculated $\langle s_1 s_2 \rangle$ for the population of fibrils with two kinks. Assuming the probability of bending in either direction was that of a random walk, a mean value of 0 and a variance of 1 would be expected.

However, a mean of 0.30 and variance of 0.91 for unconfined fibrils were calculated. From this, the probability p of bending in the same direction is obtained by $\langle s_1 s_2 \rangle = p - (1 - p)$, giving $p = 0.65 \pm 0.03$. The fibrils are therefore bending in a preferential direction, which is not in agreement with the alternating amorphous-crystalline regions model,^[116] and which indeed leads to a non-symmetric, non-gaussian distribution of the kink angle distribution (see Figure 3A). This finding therefore further supports the hypothesis that kinks are a product of mechanical strain. Indeed, it is much more probable that they break in the same direction if they are created by the same mechanical event. Accordingly, a log-normal segment length distribution is found in between kinks (see Figure 3C).

In addition, we calculated, $\langle |\sum_{i=1}^{n_k} s_i| \rangle$, for $n_k = 2; 3; 4$, both from the data and from the probability p to bend in the same direction as given by Equations 1-3. The arbitrarily in the sign assignment, which is introduced in attributing right or left from a given fibril end taken as origin, is removed by taking absolute values of the averages (see Figure 5B). In general, a good agreement between this simple theory and the experimental values was observed, Figure 5C. The constant values support the hypothesis that the aforementioned increase in kink number under confinement, is due mainly to pre-existing unobservable kinks becoming apparent when the fibrils adopt a higher degree of folding to gain in entropy. Indeed, Usov et al.^[45] reported that it is hard to distinguish kinks below an angle of 20° . In addition, if new kinks were being introduced through confinement we would expect a decrease in the values of the sum as a function of confinement, as the bending of the fibril would be independent of the direction of the pre-existing kinks. Only the case of four kinks shows discrepancies with the supposed model. It is hard to ascertain if this is from poor statistics or maybe an effect of the confinement. Therefore, from this data, we cannot exclude the possibility that extra kinks might be formed due to the confinement itself.

Discussion and conclusions

In this study, the effect of weak confinement on individual CNFs has been explored. Alignment was observed and quantified. In addition, we observed an accentuation of the folding of the individual fibrils under confinement. Simulations showed that this effect could not be solely explained by a specific selectivity of the slits for pre-existing fibril populations, but rather confinement itself induces the conformational change. To our knowledge this is the first time the folding of cellulose upon itself under confinement has been reported. In most cases, the high concentration of CNFs prevents a detailed characterization of the single particles, however, this was overcome in our approach, by creating the confinement solely through geometry. This effect should be considered when developing materials using cellulose nanofibrils, as often confinement, be it by microfluidics, geometry or high-concentration, is used to encourage self-assembly into higher ordered materials.^[218,219,227] As a practical example, our results may have interesting implications for nematic films,^[10] cholesteric droplets,^[64] and tactoids.^[46] As the kinks impede self-assembly, these systems need to be generated by short rod-like particles. If on top of this the fibrils are further folding upon themselves when at a concentration equivalent to weak confinement, this effect could shift up the expected critical concentration or even fully prevent the self-assembly of the fibrils into such phases. The accentuated kink angle under confinement as well as the fairly constant $\langle |\sum_{i=1}^{n_k} s_i| \rangle$, for the different kink populations, lead us to suggest that a weak confinement experiment offers more information on the fibril characteristics, by bringing into observation kinks or weak regions that were not noticeable in the unconfined state, much like in the case of the circular DNA studied by Japaridze et al.^[215] In addition, a monotonic decrease in average kink angle as a function of the number of kinks, $\langle \theta_k \rangle_{nk}$ was observed. This trend and that of the preferential bending direction, lead us to suggest mechanical breaking of the fibrils. This evidence further rules out the alternating amorphous-crystalline model for kink formation.^[116] In conclusion, geometrical confinement of cellulose nanofibrils enhances characterization possibilities, thus bringing us one step closer to understanding these nanomaterials at the length-scale of the single particles. By comparing the statistical analysis of nanofibrils conformation based on experimental AFM images with simulations on entropy driven selectivity of the confining slit, it was possible to conclude that the confining geometry not only leads to orientational ordering of the fibrils, but it also has an influence on the conformation of the nanofibrils themselves. The most remarkable feature of this morphology-controlled confinement is the self-folding on the cellulose nanofibrils in order to increase the overall free volume entropy in the slit. The understanding of the implications of confinement of cellulose nanofibrils in simple

geometries may guide and inspire the design of those functional nanomaterials where CNFs have emerged as main building blocks, with far reaching consequences in soft condensed matter, nanotechnology and materials science.

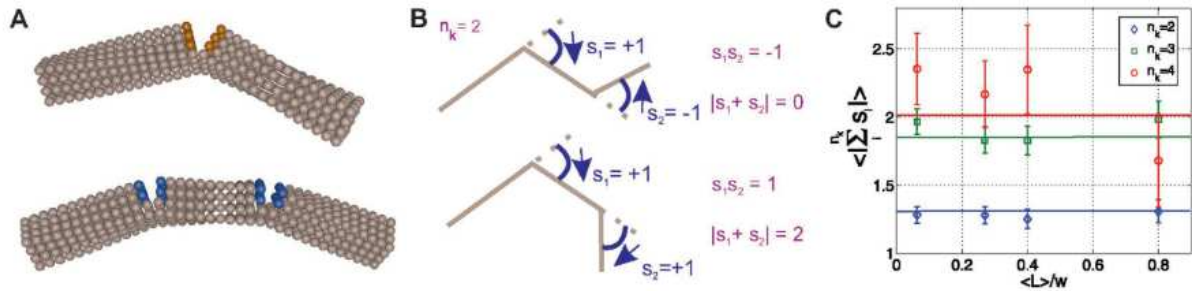


Figure 5: Kink bending. A. Depiction of a fibril with one kink (top) breaking and bending more than a fibril with two kinks (bottom). Colored beads represent the broken bonds. B) Schematic of the kink bending direction s_k , for a kink population $n_k = 2$. Top, fibril with kinks bending in opposite directions, $s_1 = -s_2$. Bottom, a fibril with kinks bending in the same direction $s_1 = s_2$. C. $\langle |\sum_{i=1}^{n_k} s_i| \rangle$, for kink populations $n_k = 2; 3; 4$. Solid horizontal lines represent the theoretical values using a probability $p = 0.65$ of kinks bending in the same direction as the previous kink.

Experimental section

Substrate preparation

1 cm² silicon wafer (P/Bor $\langle 100 \rangle$, thickness 525 μm , 1-30 ohm cm) pieces were cleaned by sonication in toluene, isopropanol and milli-Q water for 20 min each. The wafer surface was activated for 30 s in an O₂ plasma cleaner.

A solution (10 mg mL⁻¹) of poly(4-vinylpyridine) (P4VP) M_w 60000 Da (Sigma Aldrich) in 1-butanol and a solution (5 mg mL⁻¹) of linear poly(phthalaldehyde) (PPA) (Sigma Aldrich lot # is MKCC5806) in anisole were prepared for spin coating. The P4VP was chosen for its polyelectrolyte properties, at the pH of the cellulose sample it is positively charged, therefore the opposite charge of the nanocellulose fibrils. The PPA acts as a resist in the nanolithography technique used.

A 20 nm P4VP layer was spin-coated onto the freshly activated wafer (100 μl at 4000 rpm for 1 min). 60 nm of PPA was spin-coated (100 μl at 4000 rpm for 1 min) on top of the P4VP layer. The substrates were then baked for 3 min at 90 °C, to evaporate any extra solvents. The 20 nm of P4VP and 60 nm PPA were chosen to maximize both the writing of the patterns and the cellulose deposition. The initial layer of the polyelectrolyte is crucial for the adsorption of the cellulose, but also allows for a deeper patterning of the resist (as it acts as an insulating layer to the wafer, that can act as a heat sink). The 60 nm of resist was needed to screen the

full effect of the polyelectrolyte to the cellulose.

Nanolithography

The principle of the nanolithography technique used is fully described elsewhere³⁸ and was carried out on a Nanofrazor apparatus (Swisslitho). In a few words, an AFM tip was heated to a temperature at which the PPA resist starts to evaporate, due to self-amplified depolymerization.

This reaction decomposes the polymer into its volatile monomer. The coupling of this effect with the AFM feedback allows for a high precision nanolithography. In the case of this study, simple geometries were chosen to study the confinement. Rectangles with widths of 9.5 μm , 2.25 μm , 1.5 μm and 0.75 μm and constant lengths of 18.5 μm and constant depth of 60 nm. The rectangle of 9.5 μm was used as a control of the unconfined state. This control was favored over a plain P4VP layer because the lithography treatment could leave residues or change some properties of the layer due to the extreme heating, also it must be noted that the P4VP and the PPA could be mixing at some point of the process. The parameters of the AFM were chosen to obtain the desired depth. The selection of these parameters varied from tip to tip. In general, a high temperature of 900 °C and a blunted tip were needed to reach a depth of 60 nm. At this depth one tip could write up to ten patterns before contamination took over. On average five good patterns were written per wafer.

Carboxylated cellulose nanofibrils

Carboxylated cellulose nanofibrils with a charge density of 0.65 mmol g^{-1} cellulose were prepared from never-dried sulphite softwood-dissolving pulp (Domsjö, Sweden) using a protocol for TEMPO-mediated oxidation with 5 mmol NaClO per gram cellulose.²¹ Using ultrasonication, 100 ml of the cellulose pulp dispersion (0.5 g L^{-1}) was fibrillated with a sonication probe (7 mm, 20% amplitude, 200 W, no interval) for 7 min. To remove non-dissolved aggregates, the dispersion was centrifuged at 4000 rcf for 60 min.

Fibril deposition and AFM

The bulk solution of cellulose fibrils was diluted 1000 times for the AFM sample preparation. A 100 μL drop of this solution was deposited onto the patterned substrates. After 3 min, the drop was gently rinsed off and the sample was gently dried by air stream. This protocol was chosen as it leads to a concentration of adsorbed fibrils lower than the critical concentration at which fibril–fibril interaction would be expected (see the “Excluded area” in the Supporting Information). AFM images of the patterns were taken using a Bruker FastScan in the scan

assist mode or a MultiMode 8 in soft tapping mode. The cantilevers in both cases were RTESPA-150 with a resonance frequency f_0 of 150 kHz and a spring constant k , of 6 N m^{-1} . Scan size was $25 \times 25 \text{ }\mu\text{m}$ and a minimum pixel resolution of 3072 pixels per line. Images were saved in the height channel and the peak force error channel.

Image analysis

Single molecule statistics were carried out using an in-house Matlab-based software, FiberApp,^[128] to trace the individual cellulose fibrils. The features of the software are fully described elsewhere^[128] and additional information on cellulose tracing with this software can be found in Usov et al.^[45] The built-in functions of the software provided the fibril contour lengths, kink angles, and individual orientation distributions. From these and the coordinates of the fibrils and kinks, additional information was extracted in Matlab, such as the fibril segment length, kink density, kink angle orientation, mean radius of gyration, the summed orientation distributions over all the images (with error bars performed by bootstrapping), positions of kinks and fibrils in slits.

From the kink angle orientation, the sum of the kink angle signs could be theoretically calculated by assuming a probability p of bending in the same direction as the previous kink (assuming only nearest-neighbor interactions), $\langle |\sum_{i=1}^{n_k} s_i| \rangle$ for different kink populations as a function of p . Considering all the possible conformations (see SI) we get the following expressions.

$$n_k = 2, \langle |\sum_{i=1}^2 s_i| \rangle = 2p \quad (1)$$

$$n_k = 3, \langle |\sum_{i=1}^3 s_i| \rangle = 2p^2 + 1 \quad (2)$$

$$n_k = 4, \langle |\sum_{i=1}^4 s_i| \rangle = 4p^3 - 4p^2 + 4p \quad (3)$$

In our confinement experiments, only the CNFs fully in the slits were taken into our statistics. To check if a fibril was in the slit, the height image was systematically compared with the equivalent peak force error image, as seen in Figure 2A. The AFM images analyzed in FiberApp were pre-processed with a 3rd order flattening provided in the NanoScope Analysis software.

Table 1: Probabilities of having n_k kinks from the unconfined statistics of fibrils of lengths between 550-650 nm.

n_k	0	1	2	3	4
p_{n_k}	0.21	0.45	0.26	0.05	0.03

Simulations

Geometry-based simulations were carried out by implementing the statistics of the unconfined CNFs in a C++ program and artificially confining them. Specifically, we implemented the cellulose fibrils with a fixed contour length, fixed kink angles and random segment lengths. In this case, fibrils between 550-650 nm were chosen, yielding a population of 104 fibrils with the following kink population probabilities p_{nk} , **Table 1**.

The preferential bending direction of the kink populations was set to the calculated one of $p = 0.65$. A fixed mean kink angle $\langle\theta_k\rangle_{0.063} = 65^\circ$ for the unconfined geometries was utilized, and $\langle\theta_k\rangle_{0.080} = 70^\circ$ for the most confined case.

From these statistics, multiple fibrils were randomly generated, with random overall orientation and random positioning of the center of mass in the slit. If the whole fibril fit into the implemented slit, it was accepted into the statistics, if not discarded. The same statistics as in the image analysis could then be carried out. In the case of fibrils with no kinks, the program was cross-checked with the analytical solutions of rigid-rods.

Acknowledgement

The authors would like to acknowledge SwissLitho AG, in particular Samuel Bisig, for the training services they provided. As well as Dr. Wye Khay Fong for her critical reading of the manuscript.

References

- [1] J. Song, C. Chen, S. Zhu, M. Zhu, J. Dai, U. Ray, Y. Li, Y. Kuang, Y. Li, N. Quispe, Y. Yao, A. Gong, U. H. Leiste, H. A. Bruck, J. Y. Zhu, A. Vellore, H. Li, M. L. Minus, Z. Jia, A. Martini, T. Li, L. Hu, *Nature* **2018**, 554, 224.
- [2] R. J. Moon, A. Martini, J. Nairn, J. Simonsen, J. Youngblood, *Chem. Soc. Rev.* **2011**, 40, 3941.
- [3] M. Frey, G. Biffi, M. Adobes Vidal, M. Zirkelbach, Y. Wang, K. Tu, A. M. Hirt, K. Masania, I. Burgert, T. Keplinger, *Adv. Sci.* **2019**, 6, 1802190.
- [4] A. C. O'Sullivan, *Cellulose* **1997**, 4, 173.
- [5] M. A. S. Azizi Samir, F. Alloin, A. Dufresne, *Biomacromolecules* **2005**, 6, 612.
- [6] Y. Nishiyama, J. Sugiyama, H. Chanzy, P. Langan, *J. Am. Chem. Soc.* **2003**, 125, 14300.
- [7] Y. Nishiyama, P. Langan, H. Chanzy, *J. Am. Chem. Soc.* **2002**, 124, 9074.
- [8] A. Isogai, T. Saito, H. Fukuzumi, *Nanoscale* **2011**, 3, 71.
- [9] A. Brandt, J. Gräsvik, J. P. Hallett, T. Welton, *Green Chem.* **2013**, 15, 550.
- [10] Y. Habibi, L. A. Lucia, O. J. Rojas, *Chem. Rev.* **2010**, 110, 3479.
- [11] E. Kontturi, P. Laaksonen, M. B. Linder, Nonappa, A. H. Gröschel, O. J. Rojas, O. Ikkala, *Adv. Mater.* **2018**, 30, 1703779.
- [12] T. Abitbol, A. Rivkin, Y. Cao, Y. Nevo, E. Abraham, T. Ben-Shalom, S. Lapidot, O. Shoseyov, *Curr. Opin. Biotechnol.* **2016**, 39, 76.
- [13] D. Klemm, F. Kramer, S. Moritz, T. Lindström, M. Ankerfors, D. Gray, A. Dorris, *Angew. Chemie Int. Ed.* **2011**, 50, 5438.
- [14] M. Schlesinger, W. Y. Hamad, M. J. MacLachlan, *Soft Matter* **2015**, 11, 4686.
- [15] T. H. Zhao, R. M. Parker, C. A. Williams, K. T. P. Lim, B. Frka-Petecic, S. Vignolini, *Adv. Funct. Mater.* **2019**, 29, 1804531.
- [16] B. Natarajan, A. Krishnamurthy, X. Qin, C. D. Emiroglu, A. Forster, E. J. Foster, C. Weder, D. M. Fox, S. Keten, J. Obrzut, J. W. Gilman, *Adv. Funct. Mater.* **2018**, 28, 1800032.
- [17] M. Shimizu, T. Saito, A. Isogai, *J. Memb. Sci.* **2016**, 500, 1.
- [18] M. Ghanadpour, B. Wicklein, F. Carosio, L. Wågberg, M. E. Kabir, S. Jeelani, D. Yang, A. Velamakanni, S. J. An, M. Stoller, J. An, D. Chen, R. S. Ruoff, *Nanoscale* **2018**, 406, 328.
- [19] R. E. Abouzeid, R. Khiari, N. El-Wakil, A. Dufresne, *Biomacromolecules* **2019**, 20, 573.
- [20] Z. Zhang, G. Sèbe, D. Rentsch, T. Zimmermann, P. Tingaut, *Chem. Mater.* **2014**, 26, 2659.
- [21] M. A. Lucchini, E. Lizundia, S. Moser, M. Niederberger, G. Nyström, *ACS Appl. Mater. Interfaces* **2018**, 10, 29599.
- [22] T. Li, J. Song, X. Zhao, Z. Yang, G. Pastel, S. Xu, C. Jia, J. Dai, C. Chen, A. Gong, F. Jiang, Y. Yao, T.

- Fan, B. Yang, L. Wågberg, R. Yang, L. Hu, *Sci. Adv.* **2018**, *4*, eaar3724.
- [23] S. Sultan, A. P. Mathew, *Nanoscale* **2018**, *10*, 4421.
- [24] G. Siqueira, D. Kokkinis, R. Libanori, M. K. Hausmann, A. S. Gladman, A. Neels, P. Tingaut, T. Zimmermann, J. A. Lewis, A. R. Studart, *Adv. Funct. Mater.* **2017**, *27*, 1604619.
- [25] M. K. Hausmann, P. A. Rühs, G. Siqueira, J. Läger, R. Libanori, T. Zimmermann, A. R. Studart, *ACS Nano* **2018**, *12*, 6926.
- [26] M. Bhattacharya, M. M. Malinen, P. Lauren, Y. R. Lou, S. W. Kuisma, L. Kanninen, M. Lille, A. Corlu, C. Guguen-Guillouzo, O. Ikkala, A. Laukkanen, A. Urtti, M. Yliperttula, *J. Control. Release* **2012**, *164*, 291.
- [27] K. Syverud, **2017**, pp. 171–189.
- [28] X. M. Dong, J.-F. Revol, D. G. Gray, *Cellulose* **1998**, *5*, 19.
- [29] T. Saito, S. Kimura, Y. Nishiyama, A. Isogai, *Biomacromolecules* **2007**, *8*, 2485.
- [30] K. Heise, G. Delepierre, A. King, M. Kostianen, J. Zoppe, C. Weder, E. Kontturi, *Angew. Chemie Int. Ed.* **2020**, anie. 202002433.
- [31] I. A. Sacui, R. C. Nieuwendaal, D. J. Burnett, S. J. Stranick, M. Jor, C. Weder, E. J. Foster, R. T. Olsson, J. W. Gilman, *Appl. Mater. Interfaces* **2014**, *6*, 6127–6138.
- [32] J.-F. Revol, H. Bradford, J. Giasson, R. H. Marchessault, D. G. Gray, *Int. J. Biol. Macromol.* **1992**, *14*, 170.
- [33] W. J. Orts, L. Godbout, R. H. Marchessault, J. F. Revol, *Macromolecules* **1998**, *31*, 5717.
- [34] E. D. Cranston, D. G. Gray, *Biomacromolecules* **2006**, *7*, 2522.
- [35] J. P. F. Lagerwall, C. Schütz, M. Salajkova, J. Noh, J. Hyun Park, G. Scalia, L. Bergström, *NPG Asia Mater.* **2014**, *6*, e80.
- [36] A. Sato, T. Yoshimura, D. Kabusaki, H. Okumura, Y. Homma, F. Nakatsubo, H. Yano, *Cellulose* **2019**, *26*, 6641.
- [37] A. Dufresne, in *Nanocellulose*, De Gruyter, Berlin, Boston, **2017**.
- [38] A. Hosseinmardi, P. K. Annamalai, B. Martine, J. Pennells, D. J. Martin, N. Amiralian, *ACS Omega* **2018**, *3*, 15933.
- [39] I. Capron, O. J. Rojas, R. Bordes, *Curr. Opin. Colloid Interface Sci.* **2017**, *29*, 83.
- [40] P. Bertsch, M. Diener, J. Adamcik, N. Scheuble, T. Geue, R. Mezzenga, P. Fischer, *Langmuir* **2018**, *34*, 15195.
- [41] A. E. J. de Nooy, A. C. Besemer, H. van Bekkum, *Recl. des Trav. Chim. des Pays-Bas* **1994**, *113*, 165.
- [42] Y. Okita, T. Saito, A. Isogai, *Biomacromolecules* **2010**, *11*, 1696.
- [43] R. Shinoda, T. Saito, Y. Okita, A. Isogai, *Biomacromolecules* **2012**, *13*, 842.
- [44] R. Hiraoki, Y. Ono, T. Saito, A. Isogai, *Biomacromolecules* **2015**, *16*, 675.
- [45] I. Usov, G. Nyström, J. Adamcik, S. Handschin, C. Schütz, A. Fall, L. Bergström, R. Mezzenga, *Nat. Commun.* **2015**, *6*, 7564.
- [46] G. Nyström, M. Arcari, J. Adamcik, I. Usov, R. Mezzenga, *ACS Nano* **2018**, *12*, 5141.
- [47] T. Saito, R. Kuramae, J. Wohlert, L. A. Berglund, A. Isogai, *Biomacromolecules* **2013**, *14*, 248.
- [48] Y. Okita, T. Saito, A. Isogai, *Holzforschung* **2009**, *63*, 529.
- [49] Y. Qing, R. Sabo, J. Y. Zhu, U. Agarwal, Z. Cai, Y. Wu, *Carbohydr. Polym.* **2013**, *97*, 226.
- [50] F. Jiang, S. Han, Y. Lo Hsieh, *RSC Adv.* **2013**, *3*, 12366.

- [51] W. Stelte, A. R. Sanadi, *Ind. Eng. Chem. Res.* **2009**, *48*, 11211.
- [52] S. Fujisawa, T. Saito, S. Kimura, T. Iwata, A. Isogai, *Biomacromolecules* **2013**, *14*, 1541.
- [53] Q. Li, S. Renneckar, *Biomacromolecules* **2011**, *12*, 650.
- [54] N. Lavoine, J. Bras, T. Saito, A. Isogai, *J. Polym. Sci. Part A Polym. Chem.* **2017**, *55*, 1750.
- [55] A. Isogai, L. Bergström, *Curr. Opin. Green Sustain. Chem.* **2018**, DOI 10.1016/j.cogsc.2018.04.008.
- [56] F. Rol, B. Karakashov, O. Nechyporchuk, M. Terrien, V. Meyer, A. Dufresne, M. N. Belgacem, J. Bras, *ACS Sustain. Chem. Eng.* **2017**, *5*, 6524.
- [57] R. S. Reiner, A. W. Rudie, in *Nanocelluloses Their Prep. Prop. Appl.*, American Chemical Society, **2017**, pp. 227–245.
- [58] C. Schütz, J. Van Rie, S. Eyley, A. Gençer, H. van Gorp, S. Rosenfeldt, K. Kang, W. Thielemans, *ACS Sustain. Chem. Eng.* **2018**, *6*, 8317.
- [59] A. N. Fernandes, L. H. Thomas, C. M. Altaner, P. Callow, V. T. Forsyth, D. C. Apperley, C. J. Kennedy, M. C. Jarvis, *Proc. Natl. Acad. Sci.* **2011**, *108*, E1195.
- [60] A. Hirai, O. Inui, F. Horii, M. Tsuji, *Langmuir* **2009**, *25*, 497.
- [61] A. Stroobants, H. N. W. Lekkerkerker, T. Odijk, *Macromolecules* **1986**, *19*, 2232.
- [62] J. Araki, S. Kuga, *Langmuir* **2001**, *17*, 4493.
- [63] X. M. Dong, T. Kimura, D. G. Gray, *Langmuir* **1996**, *12*, 2076.
- [64] Y. Li, J. J. Suen, E. Prince, E. M. Larin, A. Klinkova, H. Thérien-Aubin, S. Zhu, B. Yang, O. D. Lavrentovich, E. Kumacheva, *Nat. Commun.* **2016**, *7*, 12520.
- [65] S. Vignolini, P. J. Rudall, A. V. Rowland, A. Reed, E. Moyroud, R. B. Faden, J. J. Baumberg, B. J. Glover, U. Steiner, *Proc. Natl. Acad. Sci.* **2012**, *109*, 15712.
- [66] B. D. Wilts, H. M. Whitney, B. J. Glover, U. Steiner, S. Vignolini, *Mater. Today Proc.* **2014**, *1*, 177.
- [67] J. A. Kelly, A. M. Shukaliak, C. C. Y. Cheung, K. E. Shopsowitz, W. Y. Hamad, M. J. MacLachlan, *Angew. Chemie Int. Ed.* **2013**, *52*, 8912.
- [68] B. L. Tardy, B. D. Mattos, L. G. Greca, T. Kämäräinen, K. W. Klockars, O. J. Rojas, *Adv. Funct. Mater.* **2019**, *29*, 1808518.
- [69] A. B. Fall, S. B. Lindström, O. Sundman, L. Ödberg, L. Wågberg, *Langmuir* **2011**, *27*, 11332.
- [70] Y. Kobayashi, T. Saito, A. Isogai, *Angew. Chemie Int. Ed.* **2014**, *53*, 10394.
- [71] M. Pääkkö, J. Vapaavuori, R. Silvennoinen, H. Kosonen, M. Ankerfors, T. Lindström, L. a. Berglund, O. Ikkala, *Soft Matter* **2008**, *4*, 2492.
- [72] H. Dong, J. F. Snyder, D. T. Tran, J. L. Leadore, *Carbohydr. Polym.* **2013**, *95*, 760.
- [73] C. Aulin, J. Netrval, L. Wågberg, T. Lindström, *Soft Matter* **2010**, *6*, 3298.
- [74] M. Hamedí, E. Karabulut, A. Marais, A. Herland, G. Nyström, L. Wågberg, *Angew. Chemie Int. Ed.* **2013**, *52*, 12038.
- [75] S. Xiao, R. Gao, Y. Lu, J. Li, Q. Sun, *Carbohydr. Polym.* **2015**, *119*, 202.
- [76] D. Ciolacu, C. Rudaz, M. Vasilescu, T. Budtova, *Carbohydr. Polym.* **2016**, *151*, 392.
- [77] F. Jiang, Y.-L. Hsieh, *J. Mater. Chem. A* **2014**, *2*, 6337.
- [78] N. Lavoine, L. Bergström, *J. Mater. Chem. A* **2017**, *5*, 16105.
- [79] K. J. De France, T. Hoare, E. D. Cranston, *Chem. Mater.* **2017**, *29*, 4609.
- [80] A. Rege, M. Schestakow, I. Karadagli, L. Ratke, M. Itskov, *Soft Matter* **2016**, *12*, 7079.
- [81] I. Kalashnikova, H. Bizot, B. Cathala, I. Capron, *Langmuir* **2011**, *27*, 7471.

- [82] L. Bai, L. G. Greca, W. Xiang, J. Lehtonen, S. Huan, R. W. N. Nugroho, B. L. Tardy, O. J. Rojas, *Langmuir* **2019**, *35*, 571.
- [83] I. Capron, B. Cathala, *Biomacromolecules* **2013**, *14*, 291.
- [84] B. L. Tardy, S. Yokota, M. Ago, W. Xiang, T. Kondo, R. Bordes, O. J. Rojas, *Curr. Opin. Colloid Interface Sci.* **2017**, *29*, 57.
- [85] N. T. Cervin, L. Andersson, J. B. S. Ng, P. Olin, L. Bergström, L. Wågberg, *Biomacromolecules* **2013**, *14*, 503.
- [86] J. Bergfreund, Q. Sun, P. Fischer, P. Bertsch, *Nanoscale Adv.* **2019**, *1*, 4308.
- [87] C. G. Otoni, M. V. A. Queirós, J. B. Sabadini, O. J. Rojas, W. Loh, *ACS Omega* **2020**, *5*, 1296.
- [88] B. D. Almquist, S. A. Castleberry, J. B. Sun, A. Y. Lu, P. T. Hammond, *Adv. Healthc. Mater.* **2015**, *4*, 2090.
- [89] F. Quero, C. Padilla, V. Campos, J. Luengo, L. Caballero, F. Melo, Q. Li, S. J. Eichhorn, J. Enrione, *Carbohydr. Polym.* **2018**, *195*, 89.
- [90] A. C. A. Wan, M. F. A. Cutiongco, B. C. U. Tai, M. F. Leong, H. F. Lu, E. K. F. Yim, *Mater. Today* **2016**, *19*, 437.
- [91] M. Amaike, Y. Senoo, H. Yamamoto, *Macromol. Rapid Commun.* **1998**, *19*, 287.
- [92] A. C. A. Wan, I.-C. Liao, E. K. F. Yim, K. W. Leong, *Macromolecules* **2004**, *37*, 7019.
- [93] S. Bolisetty, R. Mezzenga, *Nat. Nanotechnol.* **2016**, *11*, 365.
- [94] S. Bolisetty, M. Arcari, J. Adamcik, R. Mezzenga, *Langmuir* **2015**, *31*, 13867.
- [95] S. Bolisetty, J. J. Vallooran, J. Adamcik, S. Handschin, F. Gramm, R. Mezzenga, *J. Colloid Interface Sci.* **2011**, *361*, 90.
- [96] C. Li, S. Bolisetty, R. Mezzenga, *Adv. Mater.* **2013**, *25*, 3694.
- [97] G. Nyström, M. P. Fernández-Ronco, S. Bolisetty, M. Mazzotti, R. Mezzenga, *Adv. Mater.* **2016**, *28*, 472.
- [98] L. van 't Hag, S. Handschin, P. M. Gschwend, R. Mezzenga, *Adv. Funct. Mater.* **2020**, *1908458*, 1.
- [99] G. Nyström, M. Arcari, R. Mezzenga, *Nat. Nanotechnol.* **2018**, *13*, 330.
- [100] M. Bagnani, G. Nyström, C. De Michele, R. Mezzenga, *ACS Nano* **2019**, *13*, 591.
- [101] S. Lombardo, S. Eyley, C. Schütz, H. van Gorp, S. Rosenfeldt, G. Van den Mooter, W. Thielemans, *Langmuir* **2017**, *33*, 5473.
- [102] K. Zhu, T. Ye, J. Liu, Z. Peng, S. Xu, J. Lei, H. Deng, B. Li, *Int. J. Pharm.* **2013**, *441*, 721.
- [103] J. H. Johnston, F. M. Kelly, J. Moraes, T. Borrmann, D. Flynn, *Curr. Appl. Phys.* **2006**, *6*, 587.
- [104] A. Sarkar, S. Zhang, B. Murray, J. A. Russell, S. Boxal, *Colloids Surfaces B Biointerfaces* **2017**, *158*, 137.
- [105] A. Sarkar, H. Li, D. Cray, S. Boxall, *Food Hydrocoll.* **2018**, *77*, 436.
- [106] J. Peng, V. Calabrese, J. Geurtz, K. P. Velikov, P. Venema, E. van der Linden, *J. Food Sci.* **2019**, *00*, 1.
- [107] J. Peng, V. Calabrese, S. J. Veen, P. Versluis, K. P. Velikov, P. Venema, E. van der Linden, *Food Hydrocoll.* **2018**, *82*, 196.
- [108] T. Wu, N. Kummer, K. J. De France, S. Campioni, Z. Zeng, G. Siqueira, J. Dong, G. Nyström, *Carbohydr. Polym.* **2020**, 117021.
- [109] M. Arcari, E. Zuccarella, R. Axelrod, J. Adamcik, A. Sánchez-Ferrer, R. Mezzenga, G. Nyström, *Biomacromolecules* **2019**, *20*, 1288.

- [110] A. C. Engström, M. Ek, G. Henriksson, *Biomacromolecules* **2006**, *7*, 2027.
- [111] M. Henriksson, G. Henriksson, L. A. Berglund, T. Lindström, *Eur. Polym. J.* **2007**, *43*, 3434.
- [112] M. Pääkkö, M. Ankerfors, H. Kosonen, A. Nykänen, S. Ahola, M. Österberg, J. Ruokolainen, J. Laine, P. T. Larsson, O. Ikkala, T. Lindström, *Biomacromolecules* **2007**, *8*, 1934.
- [113] S. Fujisawa, Y. Okita, H. Fukuzumi, T. Saito, A. Isogai, *Carbohydr. Polym.* **2011**, *84*, 579.
- [114] T. Saito, T. Uematsu, S. Kimura, T. Enomae, A. Isogai, *Soft Matter* **2011**, *7*, 8804.
- [115] G. Nyström, A. Marais, E. Karabulut, L. Wågberg, Y. Cui, M. M. Hamed, *Nat. Commun.* **2015**, *6*, 7259.
- [116] O. A. Battista, *Ind. Eng. Chem.* **1950**, *42*, 502.
- [117] S. Hanley, J.-F. Revol, L. Godbout, D. Gray, *Cellulose* **1997**, *4*, 209.
- [118] M. Khandelwal, A. Windle, *Carbohydr. Polym.* **2014**, *106*, 128.
- [119] S. Elazzouzi-Hafraoui, Y. Nishiyama, J.-L. Putaux, L. Heux, F. Dubreuil, C. Rochas, *Biomacromolecules* **2008**, *9*, 57.
- [120] J. F. Matthews, C. E. Skopec, P. E. Mason, P. Zuccato, R. W. Torget, J. Sugiyama, M. E. Himmel, J. W. Brady, *Carbohydr. Res.* **2006**, *341*, 138.
- [121] S. Paavilainen, T. Róg, I. Vattulainen, *J. Phys. Chem. B* **2011**, *115*, 3747.
- [122] Z. Zhao, O. E. Shklyaev, A. Nili, M. N. A. Mohamed, J. D. Kubicki, V. H. Crespi, L. Zhong, *J. Phys. Chem. A* **2013**, *117*, 2580.
- [123] L. Bu, M. E. Himmel, M. F. Crowley, *Carbohydr. Polym.* **2015**, *125*, 146.
- [124] J. A. Hadden, A. D. French, R. J. Woods, *Biopolymers* **2013**, *99*, 746.
- [125] S. K. Kannam, D. P. Oehme, M. S. Doblin, M. J. Gidley, A. Bacic, M. T. Downton, *Carbohydr. Polym.* **2017**, *175*, 433.
- [126] P. N. Ciesielski, J. F. Matthews, M. P. Tucker, G. T. Beckham, M. F. Crowley, M. E. Himmel, B. S. Donohoe, *ACS Nano* **2013**, *7*, 8011.
- [127] M. A. Hubbe, O. J. Rojas, L. A. Lucia, *BioResources* **2015**, *10*, 6095.
- [128] I. Usov, R. Mezzenga, *Macromolecules* **2015**, *48*, 1269.
- [129] R. H. Atalla, R. S. Atalla, U. P. Agarwal, in *Nanocelluloses Their Prep. Prop. Appl.*, **2017**, pp. 1–18.
- [130] S. Assenza, J. Adamcik, R. Mezzenga, P. De Los Rios, *Phys. Rev. Lett.* **2014**, *113*, 268103.
- [131] J. Adamcik, R. Mezzenga, *Soft Matter* **2011**, *7*, 5437.
- [132] J. G. de la Torre, V. A. Bloomfield, *Q. Rev. Biophys.* **1981**, *14*, 81.
- [133] M. Nordenström, A. Fall, G. Nyström, L. Wågberg, *Langmuir* **2017**, *33*, 9772.
- [134] M. Arcari, R. Axelrod, J. Adamcik, S. Handschin, A. Sánchez-Ferrer, R. Mezzenga, G. Nyström, *Nanoscale* **2020**, *12*, 11638.
- [135] S. Zhao, W. J. Malfait, N. Guerrero-Alburquerque, M. M. Koebel, G. Nyström, *Angew. Chemie Int. Ed.* **2018**, *57*, 7580.
- [136] H. Jin, Y. Nishiyama, M. Wada, S. Kuga, *Colloids Surfaces A Physicochem. Eng. Asp.* **2004**, *240*, 63.
- [137] A. B. Fall, S. B. Lindström, J. Sprakel, L. Wågberg, *Soft Matter* **2013**, *9*, 1852.
- [138] M. Chau, S. E. Srisandha, D. Pichugin, H. Thérien-Aubin, D. Nykypanchuk, G. Chauve, M. Méthot, J. Bouchard, O. Gang, E. Kumacheva, *Biomacromolecules* **2015**, *16*, 2455.
- [139] A. Gençer, J. Van Rie, S. Lombardo, K. Kang, W. Thielemans, *Biomacromolecules* **2018**, *acs.biomac.8b00493*.
- [140] P. Bertsch, A. Sánchez-Ferrer, M. Bagnani, S. Isabetini, J. Kohlbrecher, R. Mezzenga, P. Fischer,

- Langmuir* **2019**, *35*, 4117.
- [141] O. Nechyporchuk, M. N. Belgacem, F. Pignon, *Biomacromolecules* **2016**, *17*, 2311.
- [142] L. Geng, N. Mittal, C. Zhan, F. Ansari, P. R. Sharma, X. Peng, B. S. Hsiao, L. D. Söderberg, *Macromolecules* **2018**, *51*, 1498.
- [143] M. Shimizu, T. Saito, Y. Nishiyama, S. Iwamoto, H. Yano, A. Isogai, T. Endo, *Macromol. Rapid Commun.* **2016**, *37*, 1581.
- [144] M. Doi, S. F. Edwards, *The Theory of Polymer Dynamics*, Oxford University Press, **1988**.
- [145] C. J. S. Petrie, *J. Nonnewton. Fluid Mech.* **1999**, *87*, 369.
- [146] P. Bertsch, S. Isabettini, P. Fischer, *Biomacromolecules* **2017**, *18*, 4060.
- [147] P. G. de Gennes, *Scaling Concepts in Polymer Physics*, Cornell University Press, **1979**.
- [148] K. Kroy, E. Frey, *Phys. Rev. E* **1997**, *55*, 3092.
- [149] Y. Cao, S. Bolisetty, J. Adamcik, R. Mezzenga, *Phys. Rev. Lett.* **2018**, *120*, 158103.
- [150] P. N. Ciesielski, R. Wagner, V. S. Bharadwaj, J. Killgore, A. Mittal, G. T. Beckham, S. R. Decker, M. E. Himmel, M. F. Crowley, *Proc. Natl. Acad. Sci.* **2019**, 201900161.
- [151] K. B. Smith, J.-N. Tisserant, S. Assenza, M. Arcari, G. Nyström, R. Mezzenga, *Adv. Sci.* **2019**, *6*, 1801540.
- [152] R. Tanaka, T. Saito, T. Hänninen, Y. Ono, M. Hakalahti, T. Tammelin, A. Isogai, *Biomacromolecules* **2016**, *17*, 2104.
- [153] P. Bertsch, M. Arcari, T. Geue, R. Mezzenga, G. Nyström, P. Fischer, *Biomacromolecules* **2019**, *20*, 4574.
- [154] I. Kalashnikova, H. Bizot, P. Bertoncini, B. Cathala, I. Capron, *Soft Matter* **2013**, *9*, 952.
- [155] H. Jin, W. Zhou, J. Cao, S. D. Stoyanov, T. B. J. Blijdenstein, P. W. N. De Groot, L. N. Arnaudov, E. G. Pelan, *Soft Matter* **2012**, *8*, 2194.
- [156] N. T. Cervin, E. Johansson, J.-W. Benjamins, L. Wågberg, *Biomacromolecules* **2015**, *16*, 822.
- [157] S. Lam, K. P. Velikov, O. D. Velev, *Curr. Opin. Colloid Interface Sci.* **2014**, *19*, 490.
- [158] S. Kutuzov, J. He, R. Tangirala, T. Emrick, T. P. Russell, A. Böker, *Phys. Chem. Chem. Phys.* **2007**, *9*, 6351.
- [159] V. R. Dugyala, J. S. Muthukuru, E. Mani, M. G. Basavaraj, *Phys. Chem. Chem. Phys.* **2016**, *18*, 5499.
- [160] H. Wang, V. Singh, S. H. Behrens, *J. Phys. Chem. Lett.* **2012**, *3*, 2986.
- [161] L. Foret, A. Würger, *Phys. Rev. Lett.* **2004**, *92*, 058302.
- [162] I. Kalashnikova, H. Bizot, B. Cathala, I. Capron, *Biomacromolecules* **2012**, *13*, 267.
- [163] R. Aaen, F. Brodin, S. Simon, E. Heggset, K. Syverud, *Nanomaterials* **2019**, *9*, 259.
- [164] P. Bertsch, P. Fischer, *Langmuir* **2019**, *35*, 7937.
- [165] D. Clemens, P. Gross, P. Keller, N. Schlumpf, M. Könnecke, *Phys. B Condens. Matter* **2000**, 276–278, 140.
- [166] L. G. Parratt, *Phys. Rev.* **1954**, *95*, 359.
- [167] L. Botto, E. P. Lewandowski, M. Cavallaro, K. J. Stebe, *Soft Matter* **2012**, *8*, 9957.
- [168] F. Jiang, Y.-L. Hsieh, *Biomacromolecules* **2015**, *16*, 1433.
- [169] L. M. C. Sagis, P. Fischer, *Curr. Opin. Colloid Interface Sci.* **2014**, *19*, 520.
- [170] M. E. H. van den Berg, S. Kuster, E. J. Windhab, L. M. C. Sagis, P. Fischer, *Phys. Fluids* **2018**, *30*, 072103.

- [171] N. Scheuble, T. Geue, S. Kuster, J. Adamcik, R. Mezzenga, E. J. Windhab, P. Fischer, *Langmuir* **2016**, *32*, 1396.
- [172] E. Dickinson, B. S. Murray, G. Stainsby, *J. Chem. Soc. Faraday Trans. 1 Phys. Chem. Condens. Phases* **1988**, *84*, 871.
- [173] S. Mun, D. J. McClements, *Langmuir* **2006**, *22*, 1551.
- [174] C. Jiménez Saelices, I. Capron, *Biomacromolecules* **2018**, acs. biomac.7b01564.
- [175] F. Cherhal, F. Cousin, I. Capron, *Biomacromolecules* **2016**, *17*, 496.
- [176] Y. Habibi, L. Foulon, V. Aguié-Béghin, M. Molinari, R. Douillard, *J. Colloid Interface Sci.* **2007**, *316*, 388.
- [177] A. Braslau, P. S. Pershan, G. Swislow, B. M. Ocko, J. Als-Nielsen, *Phys. Rev. A* **1988**, *38*, 2457.
- [178] M. E. H. van den Berg, S. Kuster, E. J. Windhab, J. Adamcik, R. Mezzenga, T. Geue, L. M. C. Sagis, P. Fischer, *Langmuir* **2018**, *34*, 10932.
- [179] F. Bresme, J. Faraudo, *J. Phys. Condens. Matter* **2007**, *19*, 375110.
- [180] E. P. Lewandowski, J. A. Bernate, P. C. Searson, K. J. Stebe, *Langmuir* **2008**, *24*, 9302.
- [181] K. Du, E. Glogowski, T. Emrick, T. P. Russell, A. D. Dinsmore, *Langmuir* **2010**, *26*, 12518.
- [182] S. Coertjens, P. Moldenaers, J. Vermant, L. Isa, *Langmuir* **2014**, *30*, 4289.
- [183] G. E. Rogers, *Exp. Dermatol.* **2006**, *15*, 931.
- [184] F. Vollrath, D. P. Knight, *Nature* **2001**, *410*, 541.
- [185] C. Meier, M. E. Welland, *Biomacromolecules* **2011**, *12*, 3453.
- [186] R. Grande, E. Trovatti, A. J. F. Carvalho, A. Gandini, *J. Mater. Chem. A* **2017**, *5*, 13098.
- [187] M. S. Toivonen, S. Kurki-Suonio, W. Wagermaier, V. Hynninen, S. Hietala, O. Ikkala, *Biomacromolecules* **2017**, *18*, 1293.
- [188] M. J. Lundahl, V. Klar, L. Wang, M. Ago, O. J. Rojas, *Ind. Eng. Chem. Res.* **2017**, *56*, 8.
- [189] D. Vigolo, J. Zhao, S. Handschin, X. Cao, A. J. deMello, R. Mezzenga, *Sci. Rep.* **2017**, *7*, 1211.
- [190] M. D. Dickey, R. C. Chiechi, R. J. Larsen, E. A. Weiss, D. A. Weitz, G. M. Whitesides, *Adv. Funct. Mater.* **2008**, *18*, 1097.
- [191] T. Tian, C. S. Sharma, N. Ahuja, M. Varga, R. Selvakumar, Y. T. Lee, Y. C. Chiu, C. J. Shih, *Small* **2018**, *14*, 1.
- [192] S. Arola, T. Tammelin, H. Setälä, A. Tullila, M. B. Linder, *Biomacromolecules* **2012**, *13*, 594.
- [193] S. Campioni, M. Bagnani, D. Pinotsi, S. Lecinski, S. Rodighiero, J. Adamcik, R. Mezzenga, *Adv. Mater. Interfaces* **2020**, *7*, 2000446.
- [194] J. M. Jung, R. Mezzenga, *Langmuir* **2010**, *26*, 504.
- [195] H. B. Gray, *Nat. Chem.* **2009**, *1*, 7.
- [196] J. W. C. Dunlop, P. Fratzl, *Annu. Rev. Mater. Res.* **2010**, *40*, 1.
- [197] A. R. Studart, R. M. Erb, *Soft Matter* **2014**, *10*, 1284.
- [198] C. Zhang, D. A. Mcadams, J. C. Grunlan, *Adv. Mater.* **2016**, *28*, 6292.
- [199] J. F. Beecher, *Nat. Nanotechnol.* **2007**, *2*, 466.
- [200] G. Zheng, Y. Cui, E. Karabulut, L. Wågberg, H. Zhu, L. Hu, *MRS Bull.* **2013**, *38*, 320.
- [201] K. E. Shopsowitz, H. Qi, W. Y. Hamad, M. J. MacLachlan, *Nature* **2010**, *468*, 422.
- [202] S. Ling, D. L. Kaplan, M. J. Buehler, *Nat. Rev. Mater.* **2018**, *3*, 1.
- [203] D. Han, S. Pal, J. Nangreave, Z. Deng, Y. Liu, H. Yan, *Science (80-.)* **2011**, *332*, 342.

- [204] C. E. Castro, F. Kilchherr, D.-N. Kim, E. L. Shiao, T. Wauer, P. Wortmann, M. Bathe, H. Dietz, *Nat. Methods* **2011**, *8*, 221.
- [205] T. Tørring, N. V. Voigt, J. Nangreave, H. Yan, K. V. Gothelf, *Chem. Soc. Rev.* **2011**, *40*, 5636.
- [206] E. Kopperger, J. List, S. Madhira, F. Rothfischer, D. C. Lamb, F. C. Simmel, *Science (80-.)*. **2018**, *359*, 296.
- [207] H. T. Maune, S. Han, R. D. Barish, M. Bockrath, W. A. G. III, P. W. K. Rothmund, E. Winfree, *Nat. Nanotechnol.* **2010**, *5*, 61.
- [208] Q. Jiang, C. Song, J. Nangreave, X. Liu, L. Lin, D. Qiu, Z.-G. Wang, G. Zou, X. Liang, H. Yan, B. Ding, *J. Am. Chem. Soc.* **2012**, *134*, 13396.
- [209] P. G. de Gennes, *Scaling Concepts in Polymer Physics*, **1979**.
- [210] T. Odijk, *Macromolecules* **1983**, *16*, 1340.
- [211] T. Odijk, *Phys. Rev. E* **2008**, *77*, 060901.
- [212] D. J. Bonthuis, C. Meyer, D. Stein, C. Dekker, *Phys. Rev. Lett.* **2008**, *101*, 108303.
- [213] M. Krishnan, I. Mönch, P. Schwille, *Nano Lett.* **2007**, *7*, 1270.
- [214] P. Fanzio, C. Manneschi, E. Angeli, V. Mussi, G. Firpo, L. Ceseracciu, L. Repetto, U. Valbusa, *Sci. Rep.* **2012**, *2*, 791.
- [215] A. Japaridze, E. Orlandini, K. B. Smith, L. Gmür, F. Valle, C. Micheletti, G. Dietler, *Nucleic Acids Res.* **2017**, *45*, 4905.
- [216] G. Witz, K. Rechendorff, J. Adamcik, G. Dietler, *Phys. Rev. Lett.* **2011**, *106*, 248301.
- [217] M. R. Smyda, S. C. Harvey, *J. Phys. Chem. B* **2012**, *116*, 10928.
- [218] P. Tseng, B. Napier, S. Zhao, A. N. Mitropoulos, M. B. Applegate, B. Marelli, D. L. Kaplan, F. G. Omenetto, *Nat. Nanotechnol.* **2017**, *12*, 474.
- [219] K. M. O. Håkansson, A. B. Fall, F. Lundell, S. Yu, C. Krywka, S. V. Roth, G. Santoro, M. Kwick, L. Prael Wittberg, L. Wågberg, L. D. Söderberg, *Nat. Commun.* **2014**, *5*, 4018.
- [220] D. Pires, J. L. Hedrick, A. De Silva, J. Frommer, B. Gotsmann, H. Wolf, M. Despont, U. Duerig, A. W. Knoll, *Science (80-.)*. **2010**, *328*, 732.
- [221] L. Onsager, *Ann. N. Y. Acad. Sci.* **1949**, *51*, 627.
- [222] K. Ostermeir, K. Alim, E. Frey, *Phys. Rev. E* **2010**, *81*, 061802.
- [223] Y. Nishiyama, *J. Wood Sci.* **2009**, *55*, 241.
- [224] A. Šturcová, I. His, D. C. Apperley, J. Sugiyama, M. C. Jarvis, *Biomacromolecules* **2004**, *5*, 1333.
- [225] R. H. Newman, *Solid State Nucl. Magn. Reson.* **1999**, *15*, 21.
- [226] K. Wickholm, P. T. Larsson, T. Iversen, *Carbohydr. Res.* **1998**, *312*, 123.
- [227] G. Nyström, A. B. Fall, L. Carlsson, L. Wågberg, *Cellulose* **2014**, *21*, 1591.

CIRRICULUM VITAE

Name: Mario Arcari
E-Mail: m.arcari@gmx.ch
Date of birth: 5th May 1990

Education

Doctoral thesis

ETH Zurich (Swiss Federal Institute of Technology), Switzerland, 2017-2020

“Structure-property relationship of nanocellulose fibrils and their self-assembled materials”
in the group of Prof. Raffaele Mezzenga, Food and Soft Materials

Master of science in Food Science

ETH Zurich (Swiss Federal Institute of Technology), Switzerland, 2015-2016

MSc thesis title: “Liquid Crystal Phase Transitions in Amyloid Fiber Nematic and Cholesteric
Tactoids”, Supervisor: Prof. Dr. Raffaele Mezzenga, Dr. Gustav Nyström

BOKU, Vienna, Exchange Semester, spring 2015

Internship, Emmi AG

Emmi Frischprodukte AG, Emmen and Ostermundigen, autumn 2014

Production: Process optimization

Research and Application: Update of product specifications and process flowsheets

Bachelor of science in Food Science

ETH Zurich (Swiss Federal Institute of Technology), Switzerland, 2011-2014

BSc thesis title: “Hybrid Amyloid Membranes for Continuous Flow Catalysis”, Supervisor:
Prof. Dr. Raffaele Mezzenga, Dr. Sreenath Bolisetty

Manuscripts

- 1) M. Arcari, R. Axelrod, J. Adamcik, S. Handschin, A. Sánchez-Ferrer, R. Mezzenga, and G. Nyström, Structure property relationships of cellulose nanofibril hydro- and aerogels and their building blocks *Nanoscale* **2020**, 14-19.
- 2) P. Bertsch, M. Arcari, T. Geue, R. Mezzenga, G. Nyström, P. Fischer, Designing Cellulose Nanofibrils for Stabilization of Fluid Interfaces *Biomacromolecules* **2019**, 20, 4574.
- 3) M. Arcari, E. Zuccarella, R. Axelrod, J. Adamcik, A. Sánchez-Ferrer, R. Mezzenga, G. Nyström, Nanostructural Properties and Twist Periodicity of Cellulose Nanofibrils with Variable Charge Density *Biomacromolecules* **2019**, 20, 1288.
- 4) K. B. Smith, J.-N. Tisserant, S. Assenza, M. Arcari, G. Nyström, R. Mezzenga, Confinement-Induced Ordering and Self-Folding of Cellulose Nanofibrils *Adv. Sci.* **2019**, 6, 1801540.
- 5) G. Nyström, M. Arcari, J. Adamcik, I. Usov, R. Mezzenga, Nanocellulose Fragmentation Mechanisms and Inversion of Chirality from the Single Particle to the Cholesteric Phase *ACS Nano* **2018**, 12, 5141.
- 6) G. Nyström, M. Arcari, R. Mezzenga, Confinement-induced liquid crystalline transitions in amyloid fibril cholesteric tactoids *Nat. Nanotechnol.* **2018**, 13, 330.
- 7) S. Bolisetty, M. Arcari, J. Adamcik, R. Mezzenga, Hybrid Amyloid Membranes for Continuous Flow Catalysis *Langmuir* **2015**, 31, 13867.

Software skills

Ms Office, Latex, Blender, Photoshop, Illustrator, Programming: PHP, HTML, CSS, Matlab

Language skills

German (mother tongue), English (fluent), French (intermediate), Italian A2

References

Prof. Dr. Raffaele Mezzenga

Head of Food and Soft Materials Group, ETH Zurich

raffaele.mezzenga@hest.ethz.ch

Dr. Gustav Nyström

Head Cellulose & Wood Materials, EMPA Dübendorf

gustav.nystroem@empa.ch